MONASH University

Particle and Cell Manipulation in Microfluidics: Patterning and Trapping using Ultrasound

by

Ruhollah Habibi

Bachelor of Science in Mech. Eng. (Hons.)

Thesis submitted in fulfilment
of the requirements for the degree of

Doctor of Philosophy

Department of Mechanical and Aerospace Engineering
Faculty of Engineering
Monash University

June 2020

Particle and Cell Manipulation in Microfluidics: Patterning and Trapping using Ultrasound

Copyright Notices

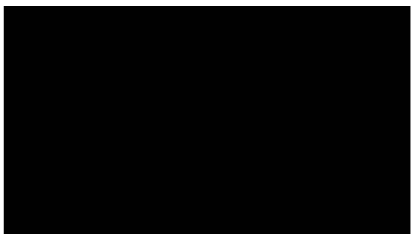

Ruhollah Habibi
27th June 2020

In the loving memory of my father,

Dedicated to my mother, beloved wife and adorable son

Abstract

With the advances of micro and nano-fabrication technologies, the new platform for miniaturised laboratory system emerged, commonly referred to as Lab on a Chip (LOC). In this new platform that is built on the foundation of microfluidics most of the chemical, medical and biological analysis processes can be conducted in significantly more accurate and controlled level, that opens a new window for understanding how diseases spread or drugs interact with cells. Manipulating of cells in this scale is essential to carry out all such activities. Among different activation methods that are used in microfluidics, acoustic excitation has the advantage of being non-contact, label-free and generally biocompatible. Handling the particles and cells in microscale by acoustic forces has shown to be promising in several applications such as sorting, separation, mixing and so, however, in such micron-size scale some physical phenomena appears to be more dominant and sometimes challenging. Although various applications of using ultrasound waves in LOC systems have been developed, the underlying physics behind these phenomena and interaction of the acoustic waves, fluid and suspended particles are to be fully understood and unravelled. One of the applications that microfluidic-based LOC systems to show a prevalence over conventional laboratory methods is the single cell analysis. Single cell analysis provides ample information on the cell structure, cell to cell communications and interaction with drugs when, for instance, introduced to different dosages of newly tested drug. In this dissertation, I presented a new understanding of the behaviour of particles with acoustic waves when the particle size increases with respect to the wavelength. Investigated the interparticle forces, it shows how the natural frequencies of the solid elastic particles play an important role in defining optimum frequency ranges for trapping and pattering of particles or cells in a one-dimensional ultrasound field. That explains why there is only a narrow frequency range that single cell patterning is achievable in a previously presented experimental method. Another finding of this study paved the way to harness the amplified attraction interparticle force under the direct influence of particle resonance frequencies. With this new finding, this work demonstrates a novel method to activate a packed bed of 10 μm particles acoustically and trap nanoparticles as small as 100 nm with capturing efficiencies as high as 97%. Capturing and retaining nanoparticles in a continuous flow is a critical precursor for several medical studies or applications, namely isolation and purification of bacteria, viruses and exosomes; the latter one is known as biomarkers for diagnoses purposes or for making newly emerged regenerative medicine. However, exosomes are scarcely diluted in the bodily fluids, hence, currently harvested from large sample volumes. The sound wave activated nano-sieve (SWANS) has the advantage of being upscalabe as it

only depends to the natural properties of the microbeads in the packed bed, so further investigation is presented that shows the effect of size and material of these funding blocks of the new system followed by a successful example of exosome capturing and enrichment in the microfluidic scale. This research establishes a new method and facilitates further steps for a fully upscaled purification and filtration system that can be used in various applications.

Publications and Outcomes

Articles in peer-reviewed journals

1. Habibi, Ruhollah, Citsabehsan Devendran, and Adrian Neild. Trapping and patterning of large particles and cells in a 1D ultrasonic standing wave. *Lab on a Chip* 17.19 (2017): 3279-3290. [1]

2. Habibi, Ruhollah, and Adrian Neild. Sound wave activated nano-sieve (SWANS) for enrichment of nanoparticles. *Lab on a Chip* 19.18 (2019): 3032-3044. , 224:529-538. [2]

3. Habibi, Ruhollah, Vincent He, Sara Ghavamian, Alex de Marco, Tzong-Hsien Lee, Marie Isabel Aguilar, Dandan Zhu, Rebecca Lim, and Adrian Neild. Exosome trapping and enrichment using a Sound Wave Activated Nano-Sieve (SWANS). *Lab on a Chip* (2020) DOI: 10.1039/d0lc00623h. [3]

Conference proceedings

1. Ruhollah Habibi and Adrian Neild. Ultrasonically Activated Packed Bed: A Platform for Separation and Enrichment of Nanoparticles in Large Scale. Abstract presented in *2019 International Congress on Ultrasonics*, Bruges, Belgium, 3-6 Sept 2019,

2. Habibi, Ruhollah, and Adrian Neild. Nanoparticle Capture Using Ultrasonic Actuation. 2019 *20th International Conference on Solid-State Sensors, Actuators and Microsystems & Eurosensors XXXIII (TRANSDUCERS & EUROSENSORS XXXIII)*. IEEE, 2019, DOI: 10.1109/TRANSDUCERS.2019.8808385. [4]

Thesis including published works declaration

I hereby declare that this thesis contains no material which has been accepted for the award of any other degree or diploma at any university or equivalent institution and that, to the best of my knowledge and belief, this thesis contains no material previously published or written by another person, except where due reference is made in the text of the thesis.

This thesis includes 2 original papers published in peer reviewed journals, and they were reproduced as chapters 3 and 4. The core theme of the thesis is patterning and trapping of micro and nanoparticles using ultrasound waves demonstrated in microfluidic systems using surface acoustic wave. The ideas, development and writing up of all the papers in the thesis were the principal responsibility of myself, the student, working within the Laboratory for MicroSystems (LMS), Department of Mechanical and Aerospace Engineering, Faculty of Engineering, under the supervision of Professor Adrian Neild and Prof. Mainak Majumdar.

Chapter 5 is based on a paper that has been accepted for publication prior to thesis final submission. My contribution nature and extent is about 85% of the submitted work that includes designs, fabrications, experimentations, numerical simulation, data analysis, interpretation and writing. The inclusion of co-authors reflects the fact that the work came from active collaboration between researchers and acknowledges input into team-based research.

In the case of Chapters 3-4 my contribution to the work involved the following:

Thesis chapter	**Publication title**	**Publication status**
3	Trapping and patterning of large particles and cells in a 1D ultrasonic standing wave	Published
4	Sound wave activated nano-sieve (SWANS) for enrichment of nanoparticles	Published

Nature and % of student contribution	**Co-author name(s) Nature and % of Co-author's contribution**	**Co-author(s), Monash student Y/N**
85% Establishment of theoretical model and method, numerical finite element method (FEM) model, development, results analysis, interpretation and writing.	1)Citsabehsan Devendran (Theory, numerical model and review of drafts 7% 2)Adrian Neild (Contribution to theory, overall supervision and review of drafts, 8%)	N, N
95% Design and fabrication of devices, experimentation, numerical modelling, development, results analysis, interpretation and writing.	2)Adrian Neild (Contribution to overall supervision and review of drafts, 5%)	N

I have not renumbered sections of submitted or published papers in order to generate a consistent presentation within the thesis.

Candidate signature: 

Candidate Name: Ruhollah Habibi

Date: 26th June 2020

The undersigned hereby certify that the above declaration correctly reflects the nature and extent of the student's and co-authors' contributions to this work. In instances where I am not the responsible author I have consulted with the responsible author to agree on the respective contributions of the authors.

Main Supervisor signature: 

Main Supervisor Name: Prof. Adrian Neild

Date: 26th June 2020

Acknowledgements

First and foremost, I would like to express my sincere gratitude to my main supervisor Professor Adrian Neild. I felt your support from the first piece of communication we had. It has been a great privilege for me to have such a constant source of support. Your mentorship, vision and positive thinking helped me to overcome challenges at any time of despair or disappointment. Furthermore, I am incredibly appreciative of the incredible patience and freedom given to pursue answers on my pace and try different ideas. Also I would like to thank Prof. Mainak Majumdar for taking the role of my co-supervisor.

Reaching this point could not be more enjoyable without the support and contributions of my fellow friends and colleagues at our Lab for MicroSystems. Saab Devendran, I couldn't find any better group mate than you as a great source of knowledge in the field, support and fun. A big thank you to Amy Fakhfouri for sharing resources and your experiences that saved me a lot of time. Jason Brenker, you are truly an engineer, thanks for your help, technical advices and also gadgets that made the life much easier in the lab. The list goes on, and I cannot be more thankful to all you guys in LMS. A huge thanks to my friend Abozar for being always there for me and creating good memories through this long journey. Thanks to my colleagues Jason Brenker and Cynthia Richards for proofreading chapters 1, 2 and 6.

To the Department of Mechanical and Aerospace Engineering, the Faculty of Engineering and the Monash Institute of Graduate Research, thank you for the technical and administrative support given throughout my candidature. Further, a big thank you to staff and experts in Melbourne Centre of Nanofabrication (MCN) for sharing their knowledge and training. This project would not have been possible without the financial support received from Discovery Project grants of Australian Research Council (ARC).

Last but not least, to my wife Sarah, thank you for your undying support, love and patience. My dream would not have been possible without your encouragement and immense sacrifices. I cannot find words to be equivalent to your never-ending backing and comfort. To my son Sean, your curiosity to explore your little world was an inspiration for me to never stop learning. Your joy and happiness has been my source of hope during all sleepless lab nights. I wish when you grow up you never stop asking questions.

Ruhollah 'Rui' Habibi
Laboratory for Micro Systems
Monash University - June 2020

Contents

List of Figures

List of Tables

Chapter 1

Introduction

Microfluidics is the scientific field of the study and application of the physics of fluids at micro-scale, thus offers advantages of visual accessibility, low sample volume, high resolution control of the fluid and suspended matter and integrability into automated lab processes on a chip. With these exceptional advantages, it has and continues to provide, opportunities to interrogate Physics at a new level and turn previously unexplored physical effects into new applications in research and industry.

1.1 Microfluidics

Microfluidics deals with small fluid volumes (usually in the range of femtolitre (fL) to microlitre (μL)) geometrically contained in channels with cross-sections between 0.5 to 500 μm. Working with such small sample volumes is desirable when samples are very expensive or laborious to produce. Moreover, reducing system size affects the governing forces that apply to the fluid. At the micro-scale fluid behaviour is governed by low Reynolds number laminar flows; viscous and surface tension forces dominate. The predictability of flow provides the opportunity of precise spatial and temporal control over the fluid. Due to the sub-millimetre scale of the fluid channels, and the dominance of viscosity and capillary effects, high-resolution control over fluids and suspensions (particles, droplet, cells, etc) are achievable. However, the dominance of laminar effects poses its own challenges. For example, the absence of turbulence makes some processes such as forced mixing harder. The need of on-demand manipulation of fluid and suspended particle, such as trapping and patterning of particles, requires the introduction of external forces to interact with the confined fluid. When combined with external forces, these microfluidic devices become useful tools for analytical chemistry and bioanalysis. [34,35]

The demand for technological advancements in the fields of molecular analysis, biodefence, molecular biology and microelectronics [36] in the twentieth century, aided the development of the field of microfluidics. The field gradually emerged in the late 1980s and the early 1990s with the invention of the inkjet printer and research on gas chromatography. [37] It then rapidly grew and demonstrated its potential for applications in various fields and technologies: organ printing, tissue engineering, display technology, immunology, chemical detection and

screening. [38]

As a multidisciplinary field, various fields namely engineering, (bio-)chemistry, physics and nanotechnology have contributed to microfluidics and in turn it led to many advances in these fields and became a key component in microsystems technology. A subset of microfluidic systems is Lab-on-a-chip (LOC), the aim of which is to replicate all conventional laboratory processes into a miniaturised platform that can be integrated with micro-electromechanical systems (MEMS); microfluidics can provide that platform. Thanks to the small size of microfluidic components, they can be easily integrated with other MEMS devices and electronic integrated circuits. Lab-on-a-chip systems are portable and have the tremendous potential for being mass-produced in an affordable manner that can revolutionise the health care industry. In addition to opening new frontiers in research and technology development in conventional high-tech laboratories, LOC devices can reduce the need for highly trained experts for the operation of specialized devices and would thus be ideal for fast track diagnosis and disease monitoring in remote areas or in less developed countries.

Many applications of microfluidics utilise the intrinsic behaviour of fluids such as capillary effects, diffusion and inertial forces for driving the system for transport, mixing and separating. The methods that use these kind of intrinsic effects are customirally termed as 'passive' methods in microfluidics. In such applications, the dominance of viscous forces means that for further manipulation, or on demand actuation at a specific point (space and time) external forces are needed. This is very critical when the manipulation of suspended particles, cells, bacteria or other biological species is required. In contrast to passive methods (i.e. inertial or capillary forces), the use of external forces or actuation are labelled as 'active' methods and include various approaches that have already been applied in microfluidics thus far, such as: optical, [39,40] magnetic, [41,42] electrical, [43,44] and acoustic. [45,46] The use of acoustics, by applying ultrasonic waves, has the advantage of providing a label-free and non-contact manipulation method while magnetic, or similar electrochemical methods require preparation of cells or particles by labelling them with magnetic or chemical receptors prior to exposing them to the respective fields. Another advantage of acoustics is its biocompatibility thus make it suitable for biological assays.

Acoustic excitation methods in microfluidics, termed acoustofluidics, are generally categorised into two forms of wave generation: bulk acoustic wave (BAW) and surface acoustic wave (SAW). Bulk acoustic waves are limited to creating an acoustic field that resonates the fluid volume and is thus restricted to certain channel dimensions or to chambers designed for only one frequency. Whilst, surface acoustic waves are generated by exciting a piezoelectric substrate on its surface and provide freedom on the direction, frequency and position of wave excitation. Furthermore, SAW provides access to higher frequencies which brings the wavelength down to the size order of typical particles such as cells that is desirable for their trapping or patterning. In addition, access to high frequencies opens to the opportunity

of exciting particles at their resonant modes which in turn can provide higher magnitudes of force or displacement as will be discussed further throughout this thesis. One particular advantage of SAW devices is that they are easily integrated onto microfluidic chips that have been used for sorting, mixing, droplet splitting, patterning and trapping.

1.2 Thesis Overview

In this thesis, new strategies for the implementation of ultrasound for the purpose of trapping and patterning of particles and cells are explored. A very useful tool that acoustics provides in this regard is acoustic force, that can be harnessed for the manipulation of particles. The focus of this work is on the modelling and characterisation of a system which harnesses particle to particle interactions and the effect that resonance frequencies have on interparticle forces. This dissertation has six chapters, including this introduction (chapter 1) and the literature review in chapter 2. The research components of the thesis span from chapter 3 to 5 and include:(i) the modelling patterning and trapping of large particles and cells in a 1D ultrasonic standing wave, (ii) the invention of sound wave activated nano-sieve (SWANS) for enrichment of nanoparticles, and (iii) the study of submicron biological particles (e.g. exosomes) trapping and enrichment using SWANS by investigating the effect of size and material of microbeads on the performance of SWANS. They are presented in the form of two publications and a submitted in-review article. The thesis ends with a conclusionary chapter that summarises the findings of this work and discusses potential future works.

1.2.1 Chapter 2: Background, Theory and Fabrication

In this chapter, a thorough review of patterning and trapping of particles in microfluidic systems and their applications, is given. Different excitation methods are discussed with emphasis on acoustics and forces that arise from ultrasonic fields, for example, drag force induced by acoustic streaming and acoustic radiation forces (primary and secondary). The relevant background theory is reviewed and a brief overview of the design and fabrication processes are provided.

1.2.2 Chapter 3: Trapping and Pattering Large Particles and Cells in 1D Ultrasound Wave

In this chapter, the mechanism behind the interaction of single solid particles and the incident ultrasound standing wave is investigated. Previously, an experimental single particle/cell patterning approach using standing surface acoustic waves (SSAWs) [12] showed that a critical range of particle diameter to wavelength (d/λ) ratio exists that facilitates single cell patterning. However, as there was no prior theoretical proof of these experimental results, in this chapter it is demonstrated, through FEM simulations, how a solid elastic sphere with a size in

the order of an acoustic wavelength ($d \rightsquigarrow \lambda$) behaves when a standing 1D field is excited at different frequencies, and especially with respect to the role that resonance of the particle might have on the nature of the forces generated. The outcome reveals distinct regions along the frequency range where the particles tend to reach the minimum or maximum pressure nodes (nodes or antinodes). This was shown for particles of three different materials. These regions, as well as the natural resonant frequencies of the elastic spheres, are dependant on the mechanical properties of the solid particle. When the interaction of two particles are investigated, those regions and natural frequencies play a significant role in the direction and magnitude of the secondary inter-particle force. For example, when poly(methylmethacrylate)(PMMA) spheres with diameters of $0 < d/\lambda < 0.5$ are evaluated, it is shown that there is a narrow band of $0.42 < d/\lambda < 0.50$ where single particle patterning is achievable (similar to the trend that was observed in the experimental work). Another valuable finding of this work is that there is also a size range (equivalently a frequency range for each size) where secondary forces are highly attractive causing the single particles to accumulate and make clusters (for the case of PMMA, this occurs between $0.33 < d/\lambda < 0.42$).

1.2.3 Chapter 4: Sound Wave Activated Nano-sieve (SWANS) For Enrichment of Nanoparticles

Building on the findings of the previous chapter, this chapter focuses on using the frequency range that generates an all-attractive force for collecting suspensions that are generally difficult to capture. The motivation behind this work comes from the demand of capturing and separating submicron-sized extra- cellular vesicles to obtain highly concentrated solutions. A brief numerical simulation demonstrates the significant role that resonance frequencies play in increasing the attractive force between neighbouring particles. A microfluidic system was developed in which the channel was filled with 10 μm polystyrene (PS) particles to form a closely packed bed. On either side of the channel, there is a pair of interdigital transducers (IDTs) that can be excited in a wide range of frequencies. When a sample of suspended fluorescent 500 nm PS particles are passed through this packed bed, and standing SAWs are generated, the packed bed attracts and collects the nanoparticles which can then be observed and measured by the change in the fluorescent light intensity. The frequency response of the nanoparticles closely resembles the results obtained from the simulations. The optimum frequencies appear to be around 69±2 MHz and 78±2 MHz. This sound wave activated nano-sieve (SWANS) system demonstrates efficient trapping and capturing of nanoparticles with a rate as high as 97%. The system can also be used for smaller nanoparticles, as demonstrated with 190 and 100 nm particles. Due to the fact that this system is only dependent on the characteristic properties of the packed bed microbeads and not on the geometry of the channel, it has the potential to be upscaled for various applications such as filtration or purification.

1.2.4 Chapter 5: Submicron biological particle trapping using a Sound Wave Activated Nano-sieve (SWANS)

With the aim of better understanding how SWANS functions, and how best it can be scaled-up, Chapter 5 focuses on characterising the system for different sizes of microbeads which can be used to fill the channel to create the packed bed. Since increasing or decreasing the size of the beads changes the size of the gap between the packed beads, and as such the underlying physics of the system, the numerical model needs to be modified accordingly. The model was expanded to include different sized beads but also to include different materials in order to investigate the effects that bead mechanical properties have on the system. The numerical model of microparticle-nanoparticle interaction was extended to consider travelling waves because in an actual SSAW excited channel both standing and travelling wanes are formed and exist inside the channel. Experiments were conducted for PS particles with sizes of 7, 10 and 15 μm along with PMMA and silica glass particles with diameters of 10 μm to cover both size and material variety. The frequency response of all sizes and materials show satisfactory agreement with the extended numerical simulations as the number of optimum peak frequencies and their trends could be predicted from the simulation. By comparing the capturing efficiencies of different bead sizes and materials, it can be concluded that increasing the size of the microbeads may have the advantage of increasing the attraction force (even though the gap between particles also increases). The comparison between materials also demonstrated that polymeric materials perform better in terms of nanoparticle collection compared to stiffer materials such as silica glass. This finding was supported by trapping and enrichment of 167 nm exosomes using a packed bed of 15 μm PS particles excited at 70 MHz. Moreover, the system biocompatibility is demonstrated by characterisation of 75 nm liposomes' membranes that have been trapped and then released in SWANS.

1.2.5 Conclusion and future work

The final chapter summarises the contributions of this thesis to the field of patterning and trapping of particles and cells using acoustofluidics principles and methods. Suggestions for the works that can be extended, areas that can be studied more in-depth and ideas for possible applications are provided at the end.

Chapter 2

Background, Theory and Fabrication

2.1 Background

2.1.1 Trapping and Patterning of Particles and Cells

Trapping and pattering of cells has been a fundamental step in tissue engineering and bioprinting, [8, 47] and also found applications in cell based biosensors, [48] drug screening, and cell biological studies [49] to study cell migration, polarisation, diffrentiation, proliferation and cell signaling (Fig. 2.1a-c). [50, 51]

A subset of cell trapping is single-cell trapping that enables alternative applications such as single-cell analysis [52–54] that provides very useful information about cell-cell interaction, drug screening and a platform for tunable engineered tissues or stem cell research. It has the advantage of preserving the information that is lost in averaging over the whole population while the size, chemistry and behaviour of cells are different and their reaction to drug or virus agents would be different as the average data mostly represents stronger behaviours. [55, 56]

Microfluidics, for its highly confined nature, high resolution control and integrability into other lab processes on a chip, has provided exceptional opportunities to develop single-cell analysis platforms. A range of techniques have been developed to establish patterning of particles and cells (Fig. 2.1c-d), particularly single-cell arrays. Some of these methods use passive hydrodynamic effects to direct individual cells to micro-patterned structure. A passive strategy is to create previously patterned microwells in a microfluidic system that traps the cells in a fine resolution array, [57–59] however, it had weak capability for further manipulation of cells after entrapment (Fig. 2.1e).Adherence of cells to the microstructures after sufficient time is one of the challenges that make these devices single-use. Although attempts have been made to address this, [60, 61] pre-designed microwell arrangement still limits the flexibility of manipulation of the cells after entrapment.

In addition to passive methods, [52, 53] a number of active methods such as optical, [62] magnetic, [63] dielectrophoretic, [64] and acoustic [12, 65–67] has been developed as well.

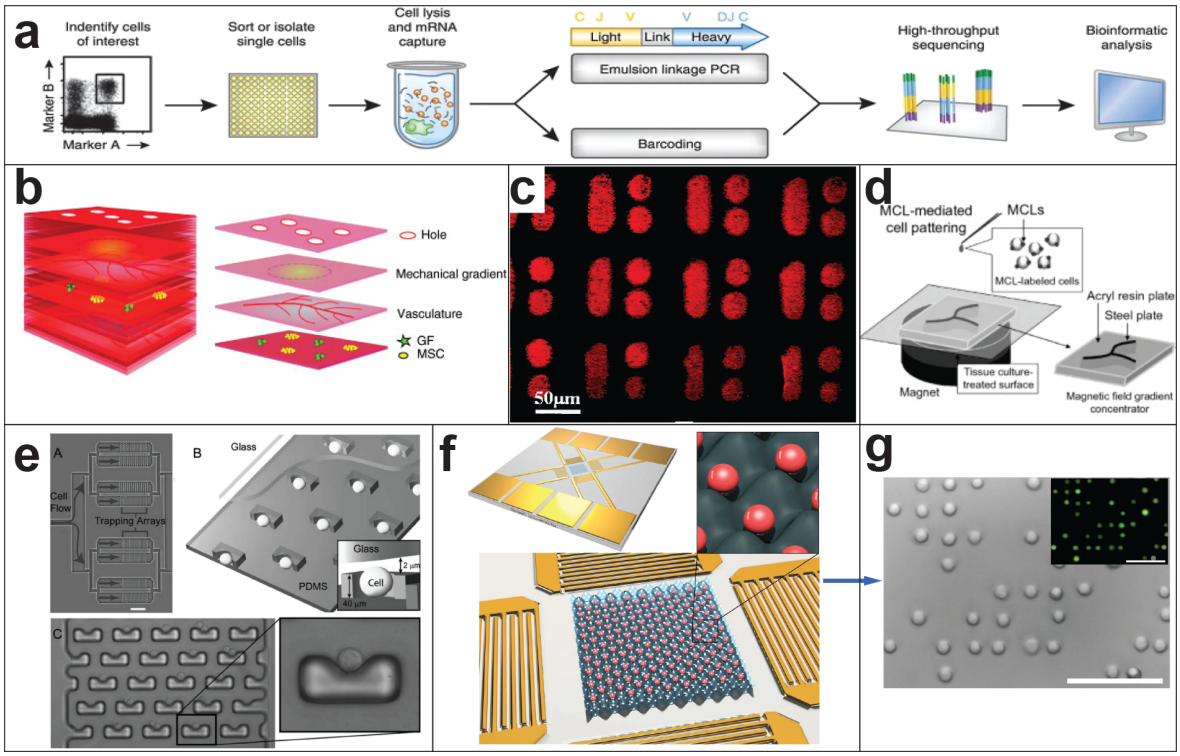

Figure 2.1: (a) An example of single-cell analysis, by cell lysis and sequencing valuable biological information can be obtained.Reprinted by permission from Springer Nature. Nature Biotechnology [7] copyright 2014. (b) Schematic principle of layer-by-layer assembly of complex tissue constructs. Tissue engineering greatly benefits from cell trapping and patterning. Reprinted from [8] with permission from Elsevier. (c) An example of protein patterning using passive microarrays in microfluidic channel. Reprinted with permission from [9]. Copyright 2012 American Chemical Society. (d) Magnetic cell patterning using magnetic cell labelling (MCL). Reprinted from [10] with permission from Elsevier. (e) Single cell trapping using microwells. Reproduced from [11] with permission from The Royal Society of Chemistry. (f-g) Single cell trapping and patterning using two-dimensional surface acoustic waves exhibited for red blood cells (g). Scale bar, 50 μm. Reprinted from [12].

Some examples are presented in Fig. 2.1d-g. While certainly each method offers a range of advantages, acoustic cell manipulation has the advantage of minimal harm to the living cells in contrast to optical tweezers or electric techniques, being free of bonding (such as seen in magnetic methods) and independence from presence or modification of electrical charge or polarity in the fluid or suspended matter.

Nonetheless, the key feature that the using of ultrasound enables single particle or cell patterning is the interplay between primary and secondary acoustic radiation force. Although single cell patterning was achieved experimentally in SAW based microfluidic techniques (Fig. 2.1f-g), there are gaps in the understanding of the mechanism behind that, especially in the role that particle resonance plays. This will be discussed briefly in this chapter in section 2.4.1 and further expanded in the Chapter 3.

2.1.2 Trapping and Separation of Nanoparticles

The trapping and separation of nanoparticles are an essential step in nanoparticle synthesis methods, [68, 69] and to a great degree for filtration of hazardous indtustrial waste. [70, 71] Another crucial application of isolating and separating of nanoparticles is in medical diagnosis and virology, as most of the viruses and desease biomarkers fall in the category of nanoparticles. [72, 73] Another group of submicron size biopaticles that attracted enormous attention in recent years are the extracellular vesicles, such as exosomes (Fig. 2.2a) for their potential as biomarkers in disease detection, and as a base for regenerative medicines in therapeutics. [74] However, they need to be trapped, separated and enriched from the suspensions prior to being used in such applications. [75]

Conventional methods for separation and purification of nanoparticles are ultracentrifugation, ultrafiltration as well as chromatography, immunoaffinity capture and precipitation, [69, 76] where these techniques have shown to be effective in terms of isolation accuracy and capturing yield. However, there are several drawbacks with them as some such as ultracentrifugation or ultrafiltration need minimum sample volume and laborious/time-consuming preparation. Although they are suitable for larger scale processing for their highthroughputs, they can potentially damage biological nanoparticles due to their high centrifugation speeds or high filtration-induced shear stresses. [77] Other methods such as immunoaffinity capture, precipitation and chromatography have been applied to lesser extent in industry. Their separation principles are based on several parameters which varies significantly between different extracellular vesicles and require precise optimisation of those parameters (such as density, conductivity, purity, surface charge and solubility). Additionally, they have relatively high costs for devices or antibodies and can be contaminant due to permanent chemical bonding or damaging to the native exosome structure. [78] These limitations hampers their application to be extended into a more universal separation and enrichment technology on larger industrial scales. Thus, development of a more robust and versatile system to capture, separate, and enrich nanoparticles is needed to fill the gap and address these challenges.

While microfluidic-based techniques for the separation, sorting, trapping and patterning microparticles and micron-range sized cells have been widely implemented, [79] the progress of similar systems for the manipulation of nanoparticles advanced less due to challenges it posed. A set of challenges arises from the characteristics of the nanoparticles themselves, such as difficulty to manipulate such smaller size of objects due to scaling of external forces with size and emerging of previously negligible effects in micro or nano-scale such as intermolecular forces, surface charge and Brownian motion. Additionally, fabrication of devices in this scale is more complicated, expensive and sometimes restricted due to technological limitations. [80] Nevertheless, methods of nanoparticle capturing and handling have been developed and incorporated into microfluidic systems inspired by microparticle manipulation techniques or conventional methods such as centrifugation, filtration or immunoaffinity capture.

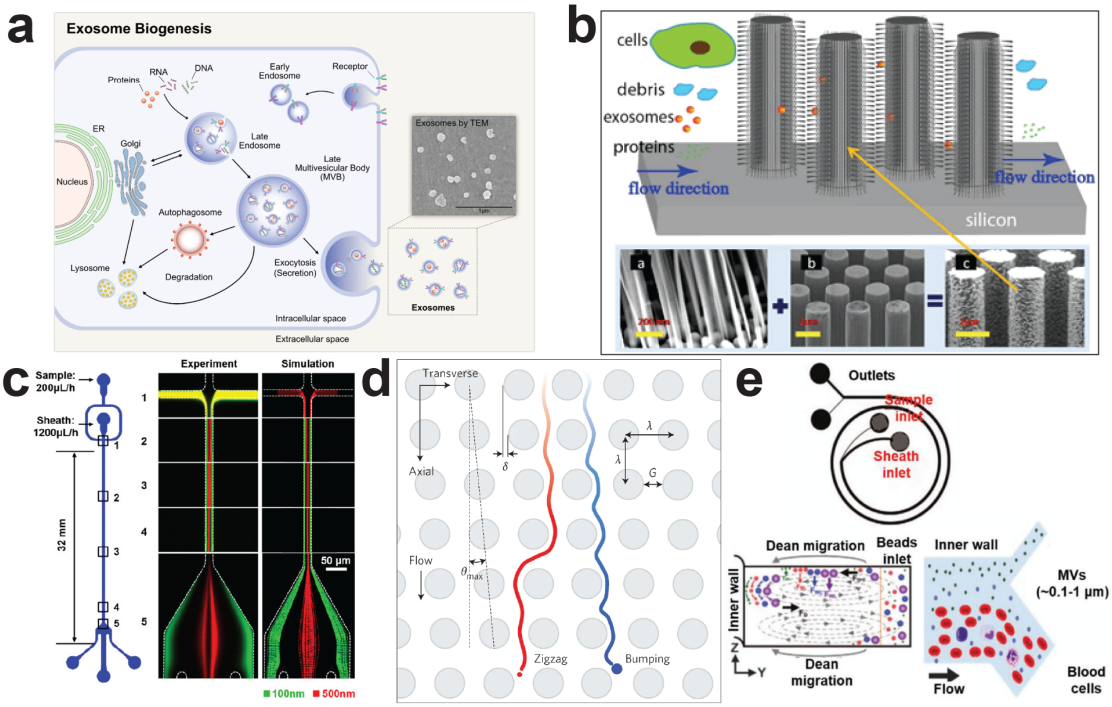

Figure 2.2: (a) Exosomes are among extracellur vesicles(EVs) within the range of 30-200 nm, carrying valuable information from parent cells draw huge interest to be used as biomarkers or for regenerative medicine. Reprinted under a Creative Commons (CC BY 4.0) licence from [13] as published by MDPI. (b) A passive method of separating exosomes using ciliated micropillars as filters. Reproduced from [14] with permission from The Royal Society of Chemistry. (c) Laminar viscous flow allows for visoelastic forces to separate larger nanoparticles from smaller ones such as exosomes. Reprinted with permission from [15]. Copyright 2017 American Chemical Society. (d) Nanoscale Deterministic lateral displacement (DLD) another passive method of nanoparticle separation. Reprinted by permission from Springer Nature. Nature Biotechnology [16] copyright 2016. (e) Inertial flow forces used for separating microvesicles (including exosomes) from larger blood cells in spiral channel. Reproduced under a Creative Commons (CC BY) license from [17] Copyright 2017, Springer Nature.

Similar to microparticle and cell manipulation, active methods provide higher accuracy, control and differentiation over passive methods as they work on the basis of a varied range of intrinsic properties of the particle. Some of the active methods that have been developed for nanoparticle separation include field flow fractionation, [81] affinity capture, [82] optical techniques, [83] magnetophoresis, [84, 85] acoustophoresis, [22] electro- and dielectrophoresis. [86, 87]. Furthermore, there are passive methods as well which may not have superiority over active techniques in term of control or accuracy, however, they are label-free and leave minimum footprint on the nanoparticles especially the biological samples. These methods use hydrodynamic forces as seen in inertial flow based systems, [88] physical displacement or sieving as developed in deterministic lateral displacement (DLD), [16] or filtration techniques (Fig. 2.2b-d). [89]

Although these methods may offer better efficiency or accuracy compared to conventional nanoparticle separation methods, they are normally limited to micro scales throughputs, which limits their usefulness in industrial applications. Chapters 4 and 5 propose a method that is

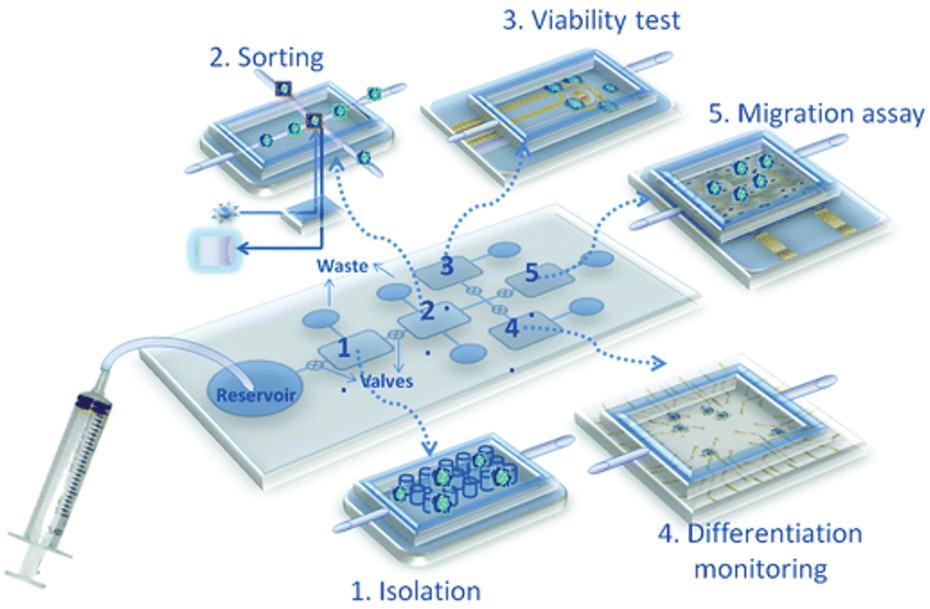

Figure 2.3: Illustrative example of a modular Lab on a Chip (LOC) that integrates multiple microfluidic modules for cell isolation, sorting, viability or migration assays and differentiation studies. Reproduced from [18] with permission from The Royal Society of Chemistry.

not limited to the geometry of microchannels but is founded based the intrinsic properties of microbeads that are activated by ultrasound so they have great potential for being upscaled to an industrial level.

2.2 Lab on a Chip

In the second half of the twentieth century with the advent of integrated circuits (IC) industry and then further development in micro and nano-fabrication technologies researchers in other field started to exploit these tools in other areas such as analysis of chemical reactions or biological assays. [36] Researchers attempted to miniaturise every process and conventional test to the micro-scale and discovered many benefits. Microfluidics is one of the major branches that has emerged as a platform of this miniaturisation and and is commonly defined as the study and application of handling fluids in micro-scale channels and chambers. [90] Many macro-scale processes were replicated and developed into such scale, namely micro-pumps, [91] -valves, [92] -sprayers, [93] -mixers [94,95] and so on. [96] Hence, this development gave birth to the idea of downsizing all conventional lab processes into a single small chip, commonly termed as Lab on a Chip (LOC) (See an illustrative example in Fig. 2.3). [97]

LOC, and broadly microfluidic systems, have the advantage of being more predictable than macro-scale methods and systems due to the absence of turbulent flows in such scale, consumption of small sample volumes and integrability with multiple different functions in one or a few chips. LOC technology also reduces the time of each process while accuracy and sensitivity of analytical processes increase as a result of the minuscule level of control over the

fluid and suspension. It has tremendous potential to invent cheap, portable and easy-to-use devices to carry out biological detection and diagnosis applications at the point of care or remote areas. [98]

With these benefits, it has drawn a huge amount of interest among researchers in different fields such as chemistry, physics, biology and engineering. Some applications to name include analytical chemistry, [99] cell culture, [100] genomic research, [101, 102] pharmaceutical drug development [103] and environmental monitoring. [104, 105]

2.2.1 Scaling Effects

In many LOC and other microfluidic applications, a fundamental task is to manipulate fluid and suspended matter to carry out processes such as sorting, mixing, separation and chemical reactions. However, as intrinsically all these processes occur in micro-scale environments where many fundamental physical phenomena appear different compared to the macro-scale a discussion will follow on the effects of scaling. It is worthy to note that although all physics laws are still valid, however, new features appear to be more pronounced while others disappear for example turbulence.

In microfluidic systems, surface to area volume ratios are dramatically higher and boundary effects are more significant, in comparison to the macro-scale. [33] Also, owing to the size order of the suspended objects and fluid paths, external fields such as electrical, magnetic, optical and acoustics can operate more effectively, this makes the fluid and particle manipulation easier. [106, 107] Some physical parameters which become so significant and prominent that they cannot be neglected are viscosity, surface tension as well as intermolecular forces that give rise to phenomena such as capillary, adhesion and wetting. [33] On the other hand some physical phenomena lose their impact and importance, for instance gravitational effects become minimal and thus, in many cases, negligible.

Similar to conventional approaches to studying fluid mechanics, non-dimensionalisation is a powerful tool to understand the impact of different parameters such as body forces, viscosity, inertia, surface tension and so on. So to realise the variation in the physics, physical parameters can be defined in terms of a characteristic length (L). As each variable changes with length scale differently, as discussed before, some of them disappear and lose their importance while others which were previously insignificant play a more important role. Applying dimensional analysis is also beneficial in designing and analysing microfluidic systems. For particle manipulation their size and distance from the source of a field or local maximum energy point are important and can play an important role so can be considered as characteristic lengths (L). Chapter 3 discusses the impact of those parameters in manipulating of particles when using acoustics. Here, some well-known dimensionless numbers that are widely used in microfluidics are discussed briefly:

Physcical Quantity	**Scaling Law**
Intermolecular Van der Waals Force	L^{-7}
Density of Van der Waals Forces between interfaces	L^{-3}
Time	L^{0}
Capillary Forces	L^{1}
Distance	L^{1}
Flow Velocity	L^{1}
Thermal power transferred by conduction	L^{1}
Electrostatic Force	L^{2}
Diffusion time	L^{2}
Volume	L^{3}
Mass	L^{3}
Gravitational Force	L^{3}
Electrical Motive Power	L^{3}
Magnetic force with an exterior field	L^{3}
Magnetic force without an exterior field	L^{4}
Centrifugal Force	L^{4}

Table 2.1: In micro/nanofluidics various physical parameters scale down or up when the characteristic length is reduced. [33]

Reynolds number

The Reynolds number, Re, is one of the important dimensionless numbers in fluid mechanics that predicts the flow regime and is given by,

$$Re = \frac{\rho U L}{\mu} \tag{2.1}$$

where, ρ, U, and μ are the density, velocity and the viscosity of the fluid, respectively. In other words, it is the ratio of inertial forces to viscous forces. Lower Reynolds numbers represent the flow regime with dominant viscous terms, called laminar flow.

In the case of microfluidics, as L and also U are very small, and Re is often limited to very low value of L. [34] As the flow is fully laminar, fluid behaviour is predictable, providing a great degree of controllability that can be used for many applications such sorting or separating of assorted particles or cells (Fig. 2.2c). However, as the flow never enters the turbulent regime, passive mixing of different phases does not occur immediately but normally needs external disturbance or force field.

Weber number

The Weber number, We, is the dimensionless number that represents the ratio of inertial to surface forces and it is normally used to describe and analyse the interfacial effects between

two or more phases. It is given by,

$$We = \frac{\rho U^2 L}{\gamma} \tag{2.2}$$

where here also ρ, U, and μ are the density, velocity and the viscosity of the fluid, respectively and γ is the surface tension of the interface considered.

Based on Equation 2.2, similar to Reynolds number when L decreases the denominator term becomes more significant, in this case the interfacial surface forces. Realising and quantifying of these effects by Weber number helps when analysing the formation of droplets and bubbles and the reaction within multiple emulsions. [108, 109]

Péclet number

The Péclet number, Pe, is given as

$$Pe = \frac{UL}{D} \tag{2.3}$$

where, D is the diffusion constant. This dimensionless number measures the ratio of convection to diffusion forces.

In microfluidics, L is very small, flow is laminar and bulk convective transfer is limited and insignificant compared to the the diffusive rate.

Capillary Number

The capillary number, Ca, reflects the interplay between viscous forces and surface tension forces acting across an interface of two different phases, given by,

$$Ca = \frac{\mu U}{\gamma} \tag{2.4}$$

where, μ, U and γ are, respectively, the viscosity of the liquid, the characteristic velocity and the surface tension or interfacial tension between the two fluid phases.

Although, the capillary number is not directly a function of the characteristic length (L), however, the characteristic velocity, U is very low in microfluidic systems inherently due to small L. This number can be used for analysis and control of droplets generation, break-up and coalescence. [110]

To exploit physical effects in the microfluidic system, dimensionless numbers and their representation of each effect, as explained in section 2.2.1 and also the scaling laws of other physical parameters with L (Table 2.1) should be taken into consideration. For example, the small size of channels, i.e L, means very low Re and Pe that shows the fluid is completely laminar. Laminar flow facilitate many processes such as separating or sorting of particles or

cells due to the predictable velocity profile, reduction in samples cross contamination or isolation of sample and reagents. However, consideration of the Pe number emphasises that the mixing regime is dominated by diffusion, which is a relatively slow process while in some cases a very rapid mixing is required. Having said that, increasing the surface area, as employed in some designs by introducing curved channels can enhance the mixing. An instant and quick way to mix is by applying an external force such as an acoustic force which has proven to be very effective. Although high ratio of surface area to volume may prevent some phenomena to occur effectively, it allows massive energy coupling when locally external force field is applied. Understanding these advantages of micro-scale, incredibly high resolution and accuracy can be accomplished which that are not practical in conventional macro-scale systems.

2.3 Actuation and Manipulation methods

One of the fundamental features of LOC systems and their advantage over the macro-scale method is their exceptional degree of control over fluid and suspended objects. This ability of regulated manipulation of particles and cells is one of the desirable characteristics of microfluidic LOC platforms, and it is achievable by utilising the distinct physical aspects of micro-scales systems. Section 2.2.1 briefly discussed these physical aspects, and here their manifestation in applied methods will be explained. The manipulation methods are customarily categorised into passive and active. Each category has a wide range of techniques that bear their own advantages and limitations. The selection of each technique depends on their performance and capacity in terms of system throughput, force magnitude and localisation ability, compatibility with biological samples, integrability and level it complexity for implementation or operation.

2.3.1 Passive Systems

Techniques that are developed based on geometrical features of the channel to modify hydrodynamic forces without applying any external impingement fall under the category of passive methods. Moreover, these techniques rely on the physical properties of the particles such as size, density, shape and deformability to manipulate them. Another approach to modifying internal forces acting on the suspended matter to control their position and motion path is introducing physical obstacles. A wide range of applications have been developed based on passive methods to carry out particle sorting (by pinched flow fractionation (PFF), [111–113] field flow fractionation (FFF), [81, 114] and hydrodynamic filtration (HDF) [115]) concentration, [116,117] and mixing. [118–120] Also physical-obstacle based sorting and separation have been achieved by introducing pillars as shown in Fig. 2.2b, [121] weris, [122] microwells, [64] and microarrays (as in Fig. 2.1d). [53, 60] One good example of the utilisation of the passive method to achieve single-cell trapping is using cup-shaped micro-arrays. Di Carlo et al. demonstrated this approach (see Fig. 2.1e). [58] Another method that has been very effective

in particle, cell and even submicron-sized exosomes sorting and separation is deterministic lateral displacement (DLD) as demonstrated in Fig. 2.2d and also mentioned earlier in section 2.1.2. [16, 123, 124]

As discussed in Section 2.2.1, at the micro-scale the Reynolds number is on the order of 1 and so the flow is fully laminar in microfluidic system. In this regime viscous effects are prevalent, so the Navier-Stokes equation can be expressed as

$$\rho\left(\frac{\partial v}{\partial t} + v \cdot \nabla v\right) = -\nabla p + \eta \nabla^2 v \tag{2.5}$$

where, ρ, v, p and η refer to the fluid density, velocity, pressure and viscosity respectively. In the limit of very low Re number, the non-linear Navier-Stokes is reduced to Stokes equation by neglecting the $(v.\nabla v)$ non-linear term: [34]

$$\rho\frac{\partial v}{\partial t} = -\nabla p + \eta \nabla^2 v \tag{2.6}$$

In a passive microfluidic system, fundamental parameters in design are the Re number, Pe number, hydrodynamic resistance, R_{hyd}, and the flow rate, Q where for any certain flow rate the pressure drop,Δp, is dictated by the hydrodynamic resistance:

$$Q = \frac{\Delta p}{R_{hyd}} \tag{2.7}$$

For any microchannel the hydrodynamic resistance is dictated by the geometrical shape and size of the channel and physical obstructions.

Most of these methods have the advantage it being cheap and straightforward to construct and operate. However, some of them are susceptible to blockage due to their reliance on physical obstacles or very small channel features to create force gradients (e.g. microwell or DLD). They may depend on channel and particles size and geometry, that limits the system flexibility and robustness. For passive trapping systems, usually, there is no control over the particles after their separation. This is another drawback in terms of tunability.

2.3.2 Active Systems

Optical

In optical manipulation methods, the external force is generated by an intense light beam (Laser). [125] This method can trap and handle individual particles in the size range of few nanometers to tens of micrometres and is customarily called optical tweezers first developed by Ashkinin in the 1970s. [126, 127] Optical tweezers work on this principle that dielectric particles are attracted and trapped in the strong electric field gradient created by a focused laser beam. [128] It has been used to manipulate individual bacteria, viruses, molecules and even atoms, [125] and its application is demonstrated in the sorting of biologicals, [129] and

mechanical characterisation of blood cells. [130] Although it provides exceptionally high resolution and accuracy in trapping and patterning of cells and submicron particles, optofluidic (optical microfluidic) systems lack high throughput and are costly to build and operate. Another major drawback of optical tweezers is that due to the use of high power laser, they damage soft tissues and are not very compatible with live cells. While optical tweezers are capable of trapping single particles or cells with exceptional resolution, with their low throughput, they cannot be used for separating and trapping of large volume of particles, especially nanoparticles and no upscaled trapping system can be developed based on optical methods.

Magnetic

Another external near-field that is commonly used in LOC and other microfluidic systems is the magnetic field. Moreover, the manipulation of particles in this field is called magnetophoresis. [131, 132] Here also the mechanism of exerting the force on particles lies on the gradient of the magnetic field. [133] As particles and cells should have magnetic properties or they need to be labelled using tiny magnetic particles. [134] Magnetophoresis has the advantage of being biocompatible and several applications have been developed for cell sorting and immunoassays. [135–137] Another desirable feature of the magnetic technique is its simple design, low cost and smooth operation. Also, it does not generate a high amount of energy and heat to be harmful to live or susceptible biological samples in contrast to optical or electrical methods. However, magnetophoretic force is relatively weak and trades off throughput, so handling large volume samples would be challenging. Furthermore, another major drawback of magnetophoresis is the need for tagging of naturally non-magnetic species or fluids, which limits its broader application.

Electrical

One of the widely used active methods uses electric fields to manipulate the fluid and the suspended matter. Applying an electric field can generate three types of forces on suspended particles: electrophoresis, electro-osmosis and dielectrophoresis. [138, 139] Electrophoresis is the manipulation of charged particles when they pass through the field. In electro-osmosis, the electrical field induces a flowing stream within the conductive fluid that can cause hydrodynamic forces. The last and most applied type of electrically-induced forces on particles, dielectrophoresis, [140] appears when a non-charged particle goes into a non-uniform field; this phenomenon depends on the field gradient and particle's polarity. [141] DEP has been widely applied for trapping, [142,143] concentration, [144,145] and separation [146] of particles and cells. While electrophoresis and in particular DEP has a high degree of sensitivity and integrability, one major drawback is high voltage requirement that causes heating making it unsuitable for many cell types and biologicals. Moreover, there are other drawbacks with electrical actuation such as relatively small forces and local heating.

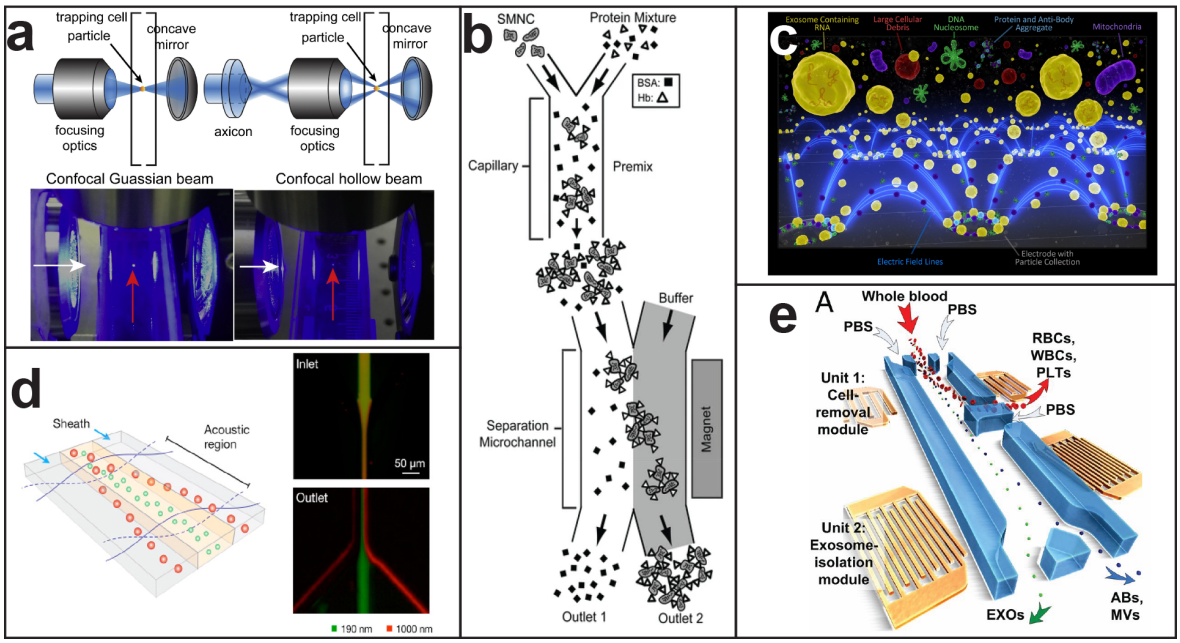

Figure 2.4: Examples of active methods for particle manipulation: (a) Optic tweezers can trap single particles and manipulate them. Reprinted from [19], with the permission of AIP Publishing. (b) Magnetic nanobeads are also used to trap and separate nanoparticles such as haemoglobin particles demonstrated here. Reprinted by permission from Springer Nature, Microfluids and Nanofluids [20] copyright 2011. (c) Dielectrophoresis (DEP) force drives EVs to the peripheral region of individual circular electrodes under AC field. Reprinted with permission from [21]. Copyright 2017 American Chemical Society. (d) Acoustic manipulation separates exosomes here from microvesicles (MVs). Reprinted with permission from [22]. Copyright 2017 American Chemical Society. (d) Titled surface acoustic waves in an acoustofluidic device separates exosomes from blood cells and MVs. Reproduced with permission. [23] Copyright 2017, National Academy of Sciences.)

Acoustic

Acoustic methods apply ultrasound waves onto the microfluidic channel to manipulate the fluid and other objects in the channel or chamber to exert forces on fluid on particles. The term acoustofluidics refers to the application of acoustics into the microfluidic systems. The acoustic technique has the advantage of being label-free (as opposed to magnetic or electrical techniques), only relying on the physical properties of the particle and cell such as size, density and compressibility (so is independent from electrical or magnetic properties of the suspended object) and also unlike optical or electrical methods is biocompatible. As acoustic is the main method selected and used in this work, a more thorough review of its principles and literature will follow in the subsequent sections. It will be shown that acoustic manipulation of particle will be more challenging when their size become smaller (i.e. nanoparticles), where drag forces (induced by acoustic streaming) will be more dominant. Moreover, creating sufficiently large acoustic radiation force will be more challenging. To tackle this, resonant modes can be excited. This thesis shows the potential of resonant modes in generating large magnitudes of inter-particle force (chapter 3) and presents a nanoparticle capturing method using this previously unexploited resonance (chapters 4 and 5).

2.4 Acoustofluidics

Sound waves are mechanical waves that propagate through a medium, fluids or solids with a specific amplitude and frequency. While in solids both longitudinal and transverse modes can be excited, in fluids sound waves only propagate in the longitudinal mode. [147] Acoustics is the study of sound waves, their generation and propagation in different mediums. Although a classical branch of Physics dating back to the nineteenth century by works of Rayleigh [148] and Faraday, [149, 150] the extensive application of sound waves developed later in the 20th century in particular ultrasonics. [151] Sound waves with frequencies higher than the audible range (>20 kHz), their study and applications are called ultrasound or ultrasonics. They have opened their way into various engineering and technologies such as non-destructive testing/examination (NDT/NDE), [152] ultrasound scanning or sonography, [153] sound navigating ranging (SONAR), [154] medical ultrasound [155] and so on. In microfluidic systems also, ultrasound has been used along with other actuation techniques that can be traced back with the development of sensor technologies. [32, 156]

"Acoustofluidics" is the overlapping field between microfluidics and acoustics, where the application of ultrasound waves into microfluidic devices and systems is studied, characterised, and new technologies are developed. Understanding the physics behind the acoustic forces that arise from the interaction of ultrasound wave, the fluid and suspended objects is essential for developing an effective microfluidic system to reach the favourable result. In the microfluidic systems, objects such as particles (solid or biological), droplets, bubbles and channel components such as pillars and posts may undergo any or all of three forces generated by ultrasound. These are acoustic streaming induced drag force, [157, 158] primary acoustic radiation force [159, 160] and secondary Bjerknes force. [161] Hereafter all three will be discussed and explained.

2.4.1 Acoustic Radiation Forces

In all ultrasound particle manipulation approaches, the main stimulation mechanism relies in the mechanical force generated by the acoustic field on the object due to the object's scattering effect on the incoming wave, generally called as Acoustic Radiation Force (ARF) and also the field's acoustic streaming phenomenon, usually called acoustic streaming induced force. ARF itself can have two contributing components, first is caused by the incoming or incident wave and referred by some as 'Primary Force' and secondly caused by the surrounding objects, especially other particles, so named as secondary or interparticle force as well as secondary Bjerknes force.

Primary force

The first attempt to analytically model acoustic radiation force was conducted by King [160] for an arbitrary size rigid sphere. Later, Yosioka and Kawasima [162] developed it to calculate force on small compressible particles in both standing and travelling plane waves. Gor'kov [159] introduced a convenient formula applicable for small spheres in any standing waves. The relative size is commonly defined compared to the wavelength of the acoustic wave, and radius of the object. An object is considered small if it is in the order of 0.01 relative to the wavelength. Hasegawa [163] presented an analytical approach that using Bessel and Hankel equations is able to predict the acoustic radiation force on elastic solid sphere in both standing and travelling waves valid for any size range. Nevertheless, to achieve a reasonable accuracy higher orders of these functions should be caclulated which makes the computation costly for large particles. Others [164–166] also presented studies of force on elastic spheres with more specific conditions such as considering viscosity or force on shells. Also, it has been shown that the viscosity only matters for small size particles, [165] where particle size is much smaller than the wavelength ($d \ll \lambda$) so the acoustic streaming induced force, also dependant on the geometry and boundary conditions, will not be dominant for particles with larger diameters. [167]

In any acoustic wave field, when an incident sound wave comes into contact with a particle, it interacts directly with the particle, gets scattered by it and also transmits into the body of the particle. In general the particle could be solid, liquid or gas so depending on the particles physical and mechanical properties (i.e. size, density and compressibility or stiffness) those interactions, scattering and transmission may vary, however, they yield a net force due to pressure and velocity gradients around the particle (Fig. 2.5a).

Perturbation theory is applied to obtain the second order non-zero forcing terms, the resultant acoustic radiation forces. [34, 168] In this approach the pressure field is assumed to consist of stationary part P_0, first order P_1, and second order P_2 expansions, in which P_1 and P_2 are assumed to be time dependent and harmonic. So we assume,

$$P_1 = P_1(x)e^{i\omega t} \tag{2.8a}$$

$$\rho_1 = \rho_1(x)e^{i\omega t} \tag{2.8b}$$

$$\mathbf{v}_1 = \mathbf{v}_1(x)e^{i\omega t} \tag{2.8c}$$

Also, $P_1 = \rho_1 c_0^2$ which is derived from isentropic derivative $c_0^2 = (\partial P/\partial \rho)_s$.

The expansion to the second order is sufficient when the perturbation, ϵ is small. Considering the stationary state density ρ_0, and velocity v_0 (which is equal to zero), pressure, density and velocity fields can be expanded as:

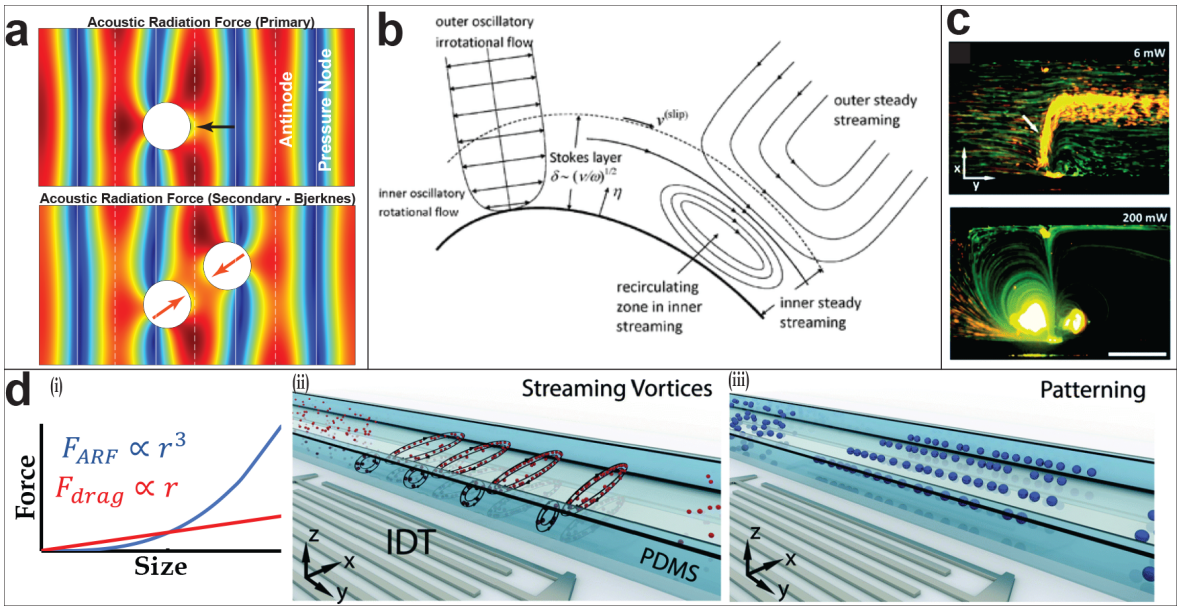

Figure 2.5: Acoustic manipulation uses three effects, primary acoustic radiation force, secondary radiation force also known as secondary Bjerknes force and drag froce induced by acoustic streaming. (a) The incident wave is scattered by the particle and net time-averaged of pressure field produces the primary force, here shown in a standing wave (top) and secondary scattering by neighbouring particle contributes to inter-particle force, i.e. secondary Bjerknes force (bottom) (b) Schematic illustrating the streaming arisen due to viscous effects at the limits of the fluid volume. Reproduced from [24] with permission from The Royal Society of Chemistry. (c) Acoustic streaming used to manipulate and separate particles. Scale bar is 200 µm. Reproduced from [25] with permission from The Royal Society of Chemistry. (d) Different scaling laws for streaming drag force and radiation forces (i) explains the dominance of streaming forces (ii) for very small particles while for larger particles radiation force is dominant (iii) and patterning due to pressure gradient is achievable. The insets (ii) and (iii) adapted from [26] with permission from The Royal Society of Chemistry.

$$\rho = \rho_0 + \epsilon\rho_1 + \epsilon^2\rho_2 + ..., \tag{2.9a}$$

$$P = P_0 + \epsilon(c_0^2\rho_1) + \epsilon^2 P_2 + ..., \tag{2.9b}$$

$$\boldsymbol{v} = \boldsymbol{v_0} + \epsilon\boldsymbol{v_1} + \epsilon^2\boldsymbol{v_2} + ... \tag{2.9c}$$

As the oscillation occurs at very high frequencies, the net footprint of the wave is its time average. The time-average operator is defined as,

$$\langle X \rangle = \frac{1}{T_{osc}} \int_0^{T_{osc}} X(t) dT_{osc} \tag{2.10}$$

where, T_{osc} is the period of oscillation, t the time variable and ω the frequency. It should be noted that for a harmonic function of $X(t) = sin(\omega t)$, its time-average, $\langle X \rangle$, is zero but $\langle sin^2(\omega t) \rangle \neq 0$.

Also, it is noted that, when we have two harmonically varying fields f and g that have complex components, the physical real-valued time-average $\langle f \ g \rangle$ is given by the real-part rule as,

$$\langle f \ g \rangle = \frac{1}{2}\mathrm{Re}\left[f(x) \ g^*(x)\right] \tag{2.11}$$

where, the asterisk denotes the complex conjugate.

Implementing Equation 2.9 alongside the continuity and Navier-Stokes equations, and taking the time average of the terms over a harmonic cycle, yields:

$$\rho_0 \boldsymbol{\nabla} \cdot \langle \boldsymbol{v_2} \rangle = -\boldsymbol{\nabla} \cdot \langle \rho_1 \boldsymbol{v_1} \rangle \tag{2.12a}$$

$$\langle \rho_1 \frac{\partial \boldsymbol{v_1}}{\partial t} \rangle + \rho_0 \langle (\boldsymbol{v_1} \cdot \boldsymbol{\nabla}) \, \boldsymbol{v_1} \rangle = \eta \boldsymbol{\nabla}^2 \langle \boldsymbol{v_2} \rangle + \beta\eta \boldsymbol{\nabla} \left(\boldsymbol{\nabla} \cdot \langle \boldsymbol{v_2} \rangle \right) - \boldsymbol{\nabla} \langle P_2 \rangle. \tag{2.12b}$$

While the time average of static and first order components of the fields equate to zero, the time average of the first order products are non-zero as explained earlier above and thus, $\langle v_2 \rangle$ and $\langle P_2 \rangle$ will in general be non-zero. The non-zero $\langle P_2 \rangle$ contributes to the acoustic radiation force. [34] This force is derived from the integration of the second-order pressure field over the surface of the particle (in an ideal inviscid fluid). For this reason it is also a time averaged phenomena and as such acts over numerous harmonic cycles, allowing a steady migration of particles in a rapidly oscillating sound field. The resulting force is:

$$\boldsymbol{F}_{rad} = \int_{S(t)} \langle P_2 \rangle (-\boldsymbol{n}) dS. \tag{2.13}$$

Here, $\boldsymbol{n}$ indicates the normal vector facing outward to the surface of the particle, S. However, as the surface of the particle, $S(t)$ deforms and moves under effect of the incident field, an integration over this surface is problematic. Instead, by applying Reynolds' transport theorem and expanding the second-order pressure field, [168] the acoustic radiation force on the particle is found, by integration over the unperturbed surface, in this form, S_0:

$$\boldsymbol{F}_{rad} = \int_{S_0} \Big(\frac{\rho_0}{2} \langle v_1^2 \rangle \boldsymbol{n} - \frac{1}{2\rho_0 c_a^2} \langle P_1^2 \rangle \boldsymbol{n} - \rho_0 \langle (\boldsymbol{n} \cdot \boldsymbol{v_1}) \boldsymbol{v_1} \rangle \Big) dS, \tag{2.14}$$

here c_a is the wave speed in the fluid. This formula uses only the first-order velocity and pressure fields applied over the stationary surface of the particle. The integrand has three distinct parts. The first two make up the momentum flux in/out of particle volume surface while the first is kinetic and the latter is hydrostatic energy, contributing to the force. The third term is the convective momentum flux so the particle's motion and surface fluctuation are taken into consideration.

Having Equation 2.14, the acoustic radiation force acting on a particle can be calculated regardless of the size of the particle and the form and type of the wave as long as first-order acoustic pressure and velocity fields are known. In this thesis, this expression was used to

numerically compute the force magnitude and direction as further explained in Chapter 3.

To be able to estimate the first-order pressure and velocity fields, we assume that they have two contributing parts corresponding to incident and scattered effects, as expressed here for the velocity term: [169]

$$\boldsymbol{v_1} = \boldsymbol{v_i} + \boldsymbol{v_s}, \tag{2.15}$$

Accordingly, the squared velocity term can be written as:

$$v_1^2 = v_i^2 + 2v_i v_s + v_s^2 \tag{2.16}$$

The scattered wave v_s is also a first-order approximation in this case. This approach was used by Yosioka and Kawasima [162] and later by Gor'kov [159] to derive the formula of the force on a compressible spherical particle in a standing acoustic wave, as given by,

$$\mathbf{F_{rad}} = -\nabla U_{Gor'kov} \tag{2.17}$$

where,

$$\begin{aligned} U_{Gor'kov} &= 2\pi r^3 \rho_f \left(\frac{1}{3} \frac{\langle P_1^2 \rangle}{\rho_f^2 c_f^2} f_1 - \frac{1}{2} \langle v_1^2 \rangle f_2 \right) \\ f_1 = 1 - \frac{\kappa_p}{\kappa_f} \quad &, \quad f_2 = \frac{2\left(\rho_p - \rho_f\right)}{2\rho_p + \rho_f} \end{aligned} \tag{2.18}$$

where $\kappa_0 = 1/(\rho_0 c_0^2)$ and κ_p denote the compressibility of the liquid and particle respectively and subscripts f and p denote the fluid and particle respectively.

However, they assumed that the particle is much smaller than the wavelength, ($d \ll \lambda$), [169] and as such the scattered-scattered term is very small compared to incident and scattered-incident fields, $v_s^2 \ll v_i v_s$ (Equation 2.16). Hasegawa and Yosioka [170] also broke the potential field into incident and scattering components and then expanded them analytically using spherical Bessel and Hankel functions. Their approach provided an analytical solution for the force on elastic particles with an arbitrary size compared to the wavelength. Similarly Doinikov [165] derived force relations within a viscous fluid. However, for large spheres, the scattered field cannot be neglected, so a higher order of approximation is required for an analytical solution.

In summary, for very small spherical particles, Gor'kov [159] solution provides sufficient accuracy and his expression of force is convenient and widely used, however for larger particles it cannot provide accurate results as it ignores scattered-scattered field effects. Using perturbation theory, we are able to express the force with first-order terms. As our subject particles are in the order of the wavelength, we must consider the scattering effects as well. In this thesis we chose to adopt a finite element method (FEM) to solve the problem directly and

utilised the general form of acoustic radiation force (Equation 2.14).

Secondary (Bjerknes) force

Secondary forces were studied by Bjerknes who formulated forces between two oscillating bubbles. [171] To acknowledge his contribution, the interparticle force that arises from the wave scattering of another particle to the first one is called secondary Bjerknes force. [161] Later, others also studied interparticle forces between bubbles, small bubble-particle and particle-particle interaction as well with mathematical approach. [172–175]

The secondary Bjerknes force is a result of the scattering of scattered wave of neighbour particle (or object) which is non-linear in nature, so developing an analytical expression needs assumptions and simplification to a great extent (Fig. 2.5a). Assuming two identical spherical particles with very small radius ($r \ll \lambda$) and at very close distance from each other ($G \ll \lambda$, where G stands for gap between two spheres) in a one-dimensional field ($v(x)$ and $P(x)$) there is an expression for inter-particle Bjerkness force, [176–178] given as,

$$\boldsymbol{F}_{Bj}(x) = 4\pi r^6 \left[\frac{(\rho_p - \rho_f)^2 \left(3\cos^2\theta - 1\right)}{6\rho_f G^4} v^2(x) - \frac{\omega^2 \rho_f \left(\kappa_p - \kappa_f\right)^2}{9G^2} P^2(x) \right] \tag{2.19}$$

where θ is the angle between the wave propagation axis and the centre-connecting line of the particles. Although for larger particles and larger gaps between them, this equation is not valid, but it does show how the force scales with the distance between them and angle with the wave axis. More recently Sepehrirahnama [175] studied the interaction between two small rigid particles around the node, although this approach is applicable to larger sizes but it cannot be used for compressible or elastic particles. All studies show that one of the key features of the secondary Bjerknes force is its high sensitivity to the gap or distance between two particles; it can be stated that $F_{Bj} \propto \frac{1}{d^n}$ and it drops quickly at further distances between neighbouring particles. [179]

As Equation 2.14 provides the acoustic radiation force acting on a particle regardless of the their size, position and surrounding particles, using FEM numerical computation, total radiation force can be calculated. When the surrounding object (in this case, another particle) is removed from the simulation, the same equation returns the primary acoustic radiation force, by subtracting that from the total radiation force, secondary Bjerknes force can be obtained:

$$\boldsymbol{F}_{total} = \boldsymbol{F}_{prim} + \boldsymbol{F}_{Bj} \quad \Rightarrow \quad \boldsymbol{F}_{Bj} = \boldsymbol{F}_{total} - \boldsymbol{F}_{prim} \tag{2.20}$$

In the following chapters (3-5) as we are dealing with large elastic solid particles, the same approach is applied to compute the secondary force between two particles where the

numerical simulation is done by COMSOL Multiphysics. Then Equation 2.14 is used to calculate the acoustic radiation force acting on particles, either single particles or in presence of other particles. Then Equation 2.20 will return the secondary Bjerknes force acting on both particles instead of Equation 2.19 which is only valid in special cases.

2.4.2 Acoustic Streaming induced Drag Forces

Acoustic streaming is a term applied to the net flow that is generated due to the existence of a non-linear second-order body force induced by the acoustic wave progression in the viscous fluid domain. Acoustic streaming is commonly categorised in two forms. One as a result of the spatial attenuation of the progressive wave which consequently produces a pressure and velocity gradient along the wave progression direction. [30] This gradient gives rise to a net force and accordingly a net flow arising from time-average non-linear effects. Secondly, when sound wave interacts with the fluid, a streaming vortex is formed within the viscous boundary layer. In that layer the fluid vibrates rotationally to conform to the no-slip boundary condition. Owing to continuity, the small vortices in the boundary layer trigger a rotation in the fluid bulk, [180] similar to a gear and pinion mechanism (Fig. 2.5b). As discussed earlier, mixing is a challenge in microfluidic systems however acoustic streaming is very functional for this application; and has been applied for the rapid fluid mixing, [181, 182] as well as pumping, [183, 184] and particle concentration (Fig. 2.5b). [185–187] However, it can also be undesirable for particle patterning, then it should be suppressed. [188, 189]

Accordingly to describe how the non-linear terms initiate streaming induced force, the derivation is based on the continuity and Navier-Stokes for compressible viscous fluid,

$$\frac{\partial \rho}{\partial t} + \nabla \cdot (\rho \mathbf{v}) = 0 \tag{2.21a}$$

$$\rho \left(\frac{\partial \mathbf{v}}{\partial t} + \mathbf{v} \cdot \nabla \mathbf{v} \right) = -\nabla p + \eta \nabla^2 \mathbf{v} + \beta \eta \nabla (\nabla . \mathbf{v}) \tag{2.21b}$$

we combine both Equations 2.21a and 2.21b, then we replace the left hand side of the combined equation with F as a body force (F), it returns,

$$\mathbf{F} = \frac{\partial (\rho \mathbf{v})}{\partial t} + \rho (\mathbf{v} . \nabla) \mathbf{v} + \mathbf{v} \nabla . \rho \mathbf{v} \tag{2.22}$$

After applying the perturbation method here, then we take the time-average, steady state terms yield zero, [34]

$$\langle \mathbf{F} \rangle = \rho_0 \langle (\mathbf{v}_1 \cdot \nabla) \mathbf{v}_1 + \mathbf{v}_1 \nabla \cdot \mathbf{v}_1 \rangle \tag{2.23a}$$

$$\langle \mathbf{F} \rangle = -\nabla \langle P_2 \rangle + \beta \eta \nabla (\nabla \cdot \langle \mathbf{v}_2 \rangle) + \eta \nabla^2 \langle \mathbf{v}_2 \rangle \tag{2.23b}$$

After time-averaging, only products of first order terms or second order terms are non-zero. The first equation (Equation 2.23a) is the Reynolds stress and thus the driving body force. On the other hand, from the second equation (Equation 2.23b) and replacing $\langle \mathbf{F} \rangle$ as Equation 2.23a) we can express the second-order velocity field $\mathbf{v}_2$ (i.e. acoustic streaming velocity) in terms of first-order velocity and pressure fields, respectively $\mathbf{v}_1$ and P_1.

The acoustic streaming drag force on a suspended particle with the initial velocity of $\mathbf{v_p}$ can be computed from the steady-state time-averaged second order velocity field ($\langle \mathbf{v_2} \rangle$), by the Stokes drag equation,

$$\mathbf{F}^{ac}_{\text{drag}} = 6\pi\eta a(\langle \mathbf{v}_2 \rangle - \mathbf{v}_p) \tag{2.24}$$

so, by knowing the acoustic streaming drag force the motion and path of the particles can be predicted. As it can be seen here in Equation2.24, it scales with particle size as the characteristic length L while the acoustic radiation force (ARF) for small particles scales with L^3 (standing wave) (or L^6 for travelling wave), [190] so when the particle size is very small, this force is significant but when the particle size is larger with respect to the acoustic wavelength then, this force loses its significance and becomes negligible. [26] Therefore in chapter 3 as large particles in the acoustic field are investigated, acoustic streaming effects are not considered (see Fig. 2.5d). In chapters 4 and 5, the investigated channel is filled with microparticles, so large vortices of acoustic streaming cannot form, however, microstreaming may exist in the pores between microparticles but due to the small size of the pores , the assumption is made that the effect of streaming is small.

2.5 Excitation Methods in Acoustofluidics

There are different ways to categorise ultrasonic systems based on the sound wave type and direction (such as longitudinal, transverse, planar, travelling or standing, and so), frequency range, source and application. In acoustofluidics, in terms of excitation mode, they fall into two main groups: bulk acoustic waves (BAW) and surface acoustic waves (SAW). In principle, the main difference between these two types is how they interact with the fluid in the channel and the mode they excite in the channel of the chamber. Bulk acoustic wave excitation mode creates resonance across the 'bulk' of the fluid volume by vibrating the channel or chamber in specific resonance modes that is dictated by the geometry of the channel. However, surface acoustic waves appear and propagate along the surface of the piezoelectric substrate upon its excitation. These waves couple locally into the liquid in a certain angle and transfer its energy to the liquid domain. Each of these methods has their inherent advantages and disadvantages; hence selecting them will depend on the type of application and desired output. This section discusses these different methods in more details.

2.5.1 Bulk Acoustic Waves

The bulk acoustic wave actuation method in microfluidic systems indicates a channel or chamber that the whole liquid volume undergoes resonance, so the term bulk is used. To achieve bulk resonance in the fluid, usually, a piezoelectric transducer generates planar waves from one side that couples at the solid-fluid boundary and travels into the fluid domain. The critical factor is the size of the channel (along the wave axis) and the amount of reflection. For example, for a 1D standing wave, the width of the channel (along the wave axis) should be a multiplication of $\lambda/2$ (half wavelength) [27, 191] as illustrated in Fig. 2.6a and similarly both width and height of the channel in 2D standing wave system. [192, 193] Channels are made of very reflective material (such as glass or silicon), or a reflector is used. Geometry limits the frequency and resonance made here. Also, transducers are typically in kHz to a few MHz range that makes the size range of the system in order of millimetres. Reducing the size allows for higher frequencies which are beneficial for particle manipulation by providing more significant force. In a 1D standing field, primary force along with the wave axis on a particle with the radius r is given by [162]:

$$F_{rad} = 4\pi r^3 E_{ac} k_{wave} sin(2k_{wave}x)\Phi \tag{2.25}$$

where x is the particle position along the wave axis, k_{wave} is the wave number given by,

$$k_{wave} = \frac{\omega}{c_f} = \frac{2\pi f}{c_f}, \tag{2.26}$$

f is the frequency and c_f is the fluid's speed of sound.

Also, E_{ac} is the acoustic energy density given by,

$$E_{ac} = \frac{P_0^2}{4\rho_f c_f^2} = \frac{1}{4}\rho_f v_0^2 \tag{2.27}$$

where, P_0 and v_0 are the amplitude of the pressure and velocity fields and Φ is the contrast factor that is given by:

$$\begin{aligned} \Phi &= \frac{1}{3}f_1 + \frac{1}{2}f_2 \\ &= \frac{1}{3}\left[\frac{5\rho_p - 2\rho_f}{2\rho_p + \rho_f} - \frac{\kappa_p}{\kappa_f}\right] \end{aligned} \tag{2.28}$$

For particles and cells much smaller than the wavelength, when $\Phi > 0$ means they will be collected at minimum pressure nodes and $\Phi < 0$ means primary force pushes the particle toward antinodes (Fig. 2.6b). This equation is only valid for very small particles; however, generally in most BAW systems, the channel size and the wavelength are extensively greater than target particles and other suspended matter.

BAW systems are less complicated to build, especially if standard transducers and channels are selected then no micro/nanofabrication presses are needed. However, pressure fields

in the BAW system are only limited to few resonant modes that can be excited, which means for a channel with a specific size only specific frequencies can be excited. Due to geometrical and technological limitations, only low frequencies in the range of few MHz are practical. BAW systems inherently lack high spatial resolution required for individual particle/cell manipulation (see Fig. 2.6c). [194] In BAW systems, the channel geometry is linked to operation frequency that places limit on the maximum sizes which can be be used especially for nanoparticle collection.

In microfluidics, BAW systems have been used extensively for sorting and separating, [27, 195–197] particle concentration, [198] and clustering. [191, 192, 199] While operating at very low frequencies, some approaches have been developed for trapping and handling of nanoparticles. [200] For smaller nanoparticles, due to scaling law, acoustic streaming induced drag froce is more dominant. Acoustic streaming drag force can be used for capturing of nanoparticles within the vortices, [189], however, it is limited to low capacity and flow rate. In an elegant method, using BAW, a cluster of microparticles were formed in the centre of the channel and then acoustic streaming assisted to lead the nanoparticles into the cluster to be further trapped by secondary Bjerknes force induced by 'seed' microparticles. [201] As this system uses resonant mode of fluid bulk in the channel, while it works well for small samples, its dependence to the channel geometry makes it unsuitable for large-scale nanoparticle trapping and separation.

2.5.2 Surface Acoustic Waves

Surface acoustic waves were first theoriesed by Lord Rayleigh in 1885 as a form of wave in elastic solids. [157] Since then, they have been used to describe siesmic waves. Later on, in the mid 20TH by the invention of interdigital transducers (IDTs) printed on the surface of piezoelectric substrates, surface acoustic waves found a new application in radio-frequency (RF) relays and filters; [32,202] and continues to do so today. New piezoelectric crystals such as lithium tantalate (LT) and lithium niobate (LN) with their improved electro-mechanical coupling paved the way for wider application of SAW in different industries, started with telecommunication [203,204] and then expanded to other application such as bio-sensor technologies, [205] optical modulators, [206] touch sensitive screens, [207] and automotive windscreen raindrop sensors [208] as well as microfluidics.

As SAW mainly develop and progress on the surface, they propagate on the surface of the solid in two dimensions only (Fig. 2.6d), so they decay slower than bulk acoustic waves, so energy dissipation is considerably lower. Moreover, SAW systems can generate much higher frequencies in the order of MHz (Very High Frequencies, VHF) and GHz (Ultra High Frequencies, UHF) that is a major advantage over BAW systems in microfluidics as it can provide many more effects to exploit in handling the fluid and manipulation of particles.

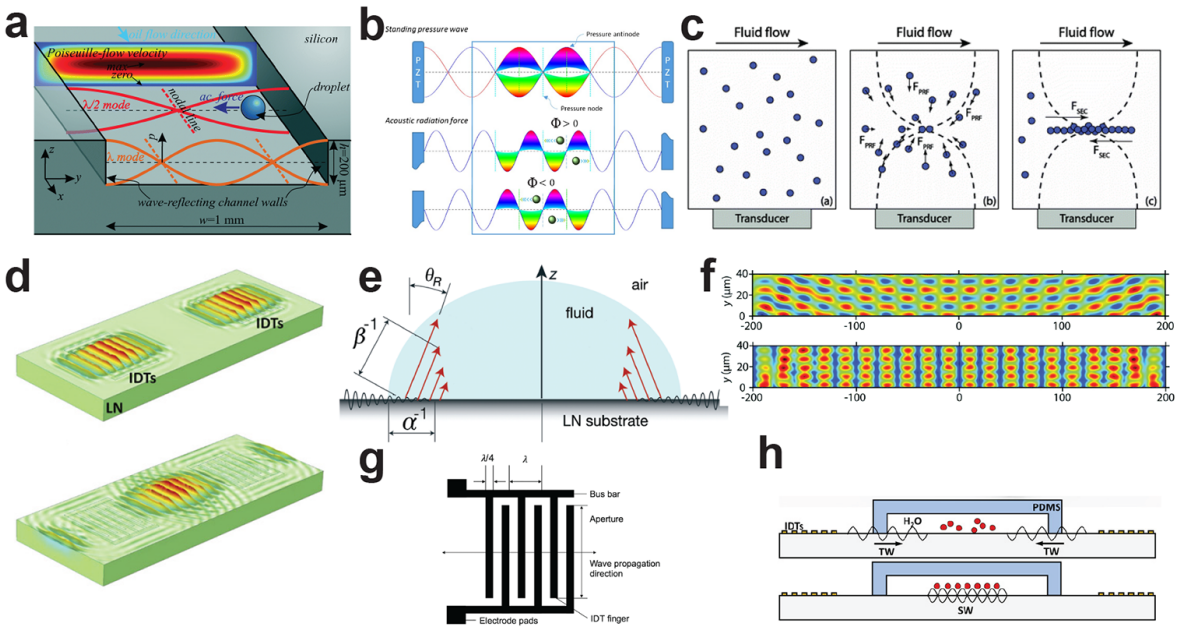

Figure 2.6: (a) Schematic of Bulk Acoustic Wave (BAW) manipulation of particles in microfluidic systems. [27] - Published by The Royal Society of Chemistry. (b) In a standing wave, acoustic radiation force (ARF) pushed the particles with positive contrast factor ($\Phi > 0$) to pressure nodes and with $\Phi < 0$ to antinodes. Reproduced from [28] under Creative Commons attribution (CC BY 4.0). (c) Generally for small particles, primary forces pushes the particles toward the pressure node (or antinode) and the secondary force helps their aggregation. Reproduced from [29] with permission from The Royal Society of Chemistry. (d) Illustration of how SAW is generated on piezoelectric substrate surface and creating standing wave in the middle using two IDTs. (e) At substrate-fluid interface, SAW transmits its energy to the fluid domain at Rayleigh angle (θ_R), attenuates the surface with a rate of α and the transmitted wave attenuates in the fluid with a different attenuation coefficient, β. (f) Surface plots of first-order pressure fields, P_1, at top and time-averaged modulus of the first-order pressure fields, $\langle P_1 \rangle$ show a standing wave forms in the channel in horizontal direction by two-opposing SAW. Reproduced from [30] with permission from The Royal Society of Chemistry. (g) Basic design of a single frequency straight IDT based on its wavelength, λ. (h) One application of standing SAW (SSAW) for patterning of particles. (d)&(h) are reproduced from [31] under Creative Commons attribution-NonCommercial license. (e)&(g) are reproduced from [32] with permission from The Royal Society of Chemistry.

Here, wavelengths can be as short as the size of the particles, cells, or submicron biomolecules thus enabling higher spatial resolution contrary to bulk acoustic wave systems. Further examples of these applications are discussed below.

The surface acoustic wave coupling to the fluid domain occurs locally and then the acoustic wave propagates into the fluid rather than resonating the whole fluid volume. Standing surface acoustic waves (SSAW) can be generated by exciting two opposing IDTs independent of the channel geometry (Fig. 2.6d and f), that is another key advantage that permits flexibility for selecting channel size or frequency to be applied. In addition to these benefits, SAW chips offer great integrability into lab on chip devices and have found application in droplet generation, [209] merging, [210] and steering, [211,212] atomisation, [213,214] size-based sorting, [215](Fig. 2.4d and e) particle patterning, [12](Fig. 2.1f and 2.6h) and trapping of cells

and nanoparticles. [2,216]

Theory

One of the common groups of materials in the micro-electromechanical systems (MEMS) is piezoelectric materials which is also used in a wide range of other applications from sensors, sound production to amplifiers and quartz watches. Piezoelectricy means the conversion of mechanical stress into electric charges and vice versa; this bidirectional phenomenon is called converse piezoelectric effect. [217] Surface acoustic waves can be generated when an oscillating electrical charge is applied across the comb-shaped periodic circuits that are patterned on the surface of the piezoelectric material (Fig. 2.6d). These patterned comb-shaped electrodes are customarily called interdigital or interdigitated transducers (for short IDT) as they resemble inter-locking fingers. The width and spacing of these finger-like periodic patterns of electrodes dictates the wavelength (λ_{saw}) and thus the frequency (f_{saw}) of the sound wave (Fig. 2.6g), for any piezoelectrical material with certain speed of sound, c_{saw}, as follows: [218]

$$f_{saw} = \frac{c_{saw}}{\lambda_{saw}} \tag{2.29}$$

where the width and spacing between each finger pair is equal to quarter of wavelength ($\lambda_{saw}/4$) in the most basic design (Fig. 2.6g). For most of piezoelectric materials, the speed of sound depends to the crystal cut and wave propagation direction. Lithium niobate ($LiNbO_3$), usually abbreviated as LN, is the most common piezoelectric material in SAW systems for its desirable properties, such as low acoustic attenuation, [204] high electromechanical coupling coefficient and high spontaneous polarization. [219,220] The electromechanical coupling coefficient, regarded the most important coefficient of piezoelectric materials, expresses how effectively electro-mechanical energies convert to each other. [221]

At the interface of solid-fluid, a sound wave transfers and transmits its energy into the fluid domain at a certain angle, θ_R, known as Rayleigh angle and the transmitted waves are called Rayleigh leaky waves (Fig. 2.6e). The sound wave then propagates into tThe fluid at θ_R (with respect to the surface normal) given by the Snell's law, [180]

$$\theta_R = sin^{-1}\left(\frac{c_f}{c_{saw}}\right) \tag{2.30}$$

Due to conservation law of energy, SAW decays across the surface as it progresses because it continuously leaks its energy into the fluid at a rate, known as the attenuation coefficient, α, and given by: [222,223]

$$\alpha = \frac{\rho_f c_f}{\rho_{sub} c_{saw} \lambda_{saw}} \qquad (m^{-1}) \tag{2.31}$$

where, ρ_{sub} is the density of the piezoelectric substrate.

Although leaky waves and attenuation occurs at the interface of solid-gas too, it is considerably lower and thus is normally neglected as most of the acoustofluidic applications deal with liquids. To minimise, energy loss, IDTs are placed either directly underneath the liquid channel or more commonly out of the channel under an empty chamber with the micro channel chips (usually made of PDMS) or completely exposed to air. That is to minimise the loss of energy because of SAW leaking to solid is not negligible. In the liquid chamber, leaky waves also attenuate though in considerably lower rates. Similarly, the attenuation coefficient in liquid is given by,

$$\beta = \frac{\omega^2 \left(\frac{4}{3}\eta + \eta'\right)}{\rho_f c_f^3} \qquad (m^{-1}) \tag{2.32}$$

where η and η' are shear and bulk viscosity coefficients of the the fluid, accordingly. Actually, this attenuation along the Rayleigh angle is the driving force behind the acoustic streaming in SAW based microfluidic channels. [223]

Across the solid-fluid interface, the attenuation length (the inverse of attenuation coefficient as shown in Fig. 2.6e) is defined as a length that the wave decays to $1/e$ of its initial amplitude ($\approx 38\%$). For a typical SAW device using LN as substrate and water as fluid, with $\rho_f \approx 1000$ kg/m^3, $c_f \approx 1500$ m/s, $\rho_s = 4650$ kg/m^3 and $c_s \approx 4000$ m/s (in x-direction of 128° Y-cut LN) the attenuation length of the surface wave is $l_{saw} \approx 12.4\lambda_{saw}$. However, in the liquid domain, the attenuation coefficient as given in Equation 2.32 is mainly a function of the frequency. At typical SAW frequency of 100 MHz, this length is approximately 2.2 mm which is significantly larger than the height of the channels normally used in microfluidics. That means sound wave has sufficient energy to interact with fluid and solid particles inside channel boundaries.

One of the major advantages of SAW over bulk acoustic wave systems is its capability to modify the pressure field by reconfiguring the IDTs. There are a wide range of IDT configurations that have been developed or adopted for different applications. Here, some of the more commonly used configurations will be introduced. Straight IDTs have the most basic design though very efficient operating at single designed frequency, hence majority of microfluidic SAW devices use this configuration. It consists of uniform distribution of straight electrodes or fingers with equal width and spacing ($1/4\lambda_{saw}$) (Fig. 2.7b). The number of fingers are chosen in a way to match the impedance and minimise the reflected power. [224]

Focused IDTs with cocentric curved fingers will provide a wave focused at a desired point near the IDT while the majority of the wave energy is confined to a narrow beam. [182,225,226] This configuration is favourable when a highly localised transfer of energy into a specific area in the channel is needed, for example droplet breakup. Configuration with varied spacing or

dimensions, such as chirped [66] or slanted IDTs, [227] enables excitation is a wide range of frequencies rather than a single frequency (as in straight IDTs). Although they may not be as efficient in terms of maximum power transmission or providing a clean sinusoidal waveform they are very essential in studies and applications that different range of wavelengths or frequencies are required within a single device. [12]

The studies presented in chapters 4 and 5 establish and focus on the effect of the elastic solid particle's resonance on the secondary Bjerknes force; so, chirped IDTs were a critical tool for these studies. Different chirped IDTs with varied wavelengths have enabled the finding of the optimum frequencies that the novel method of sound wave activated packed bed of microparticles can trap and enrich nanoparticles efficiently in a continuous flow system. [2]

2.6 Fabrication

Certainly, micro/nanofabrication technology is the backbone of SAW-based acoustofluidic systems. Considering the frequency range that is common in these systems (10 $\sim$ 1000 MHz), the width of electrodes could be as thin as 0.37 μm. Also, microchannels could be as narrow as 10 μm with much smaller features inside them. Fabricating patterns at this scale is only achievable via micro/nanofabrication.

A widely used piezoelectric substrate material is lithium niobate. Some of these characteristics are crystal orientation dependant. LN with 128° rotated Y-cut is generally preferred for its high electromechanical coupling coefficient and surface mechanical wave speed. Devices in the experimental part of this thesis, i.e. Chapter 4 and 5, used IDTs chips made from 4 in (10 cm), 0.5 mm thick 128° rotated Y-cut wafer. The speed of sound on metallised chips of this cut in its X direction is about 3888 m/s and at 45 degree (in rotated X-Z plane) is around 3690 m/s (X, Y and Z indicate the original crystal coordinates). While different chirped IDTs were used for experimental setups to cover different frequency ranges, all of them, were aligned 45° with respect to the X-propagating axis.

For the microchannel part, PDMS is the most common material in microfluidic systems although some other materials like PMMA, glass, silicon and SU8 have been used as well, however, PDMS has unique characteristics that make it a favourable choice such as optically transparent nature facilitating visualisation and observation, permeability to gases and excellent elasticity, relatively cheap to make, easy and simple to transfer high resolution patterns and biocompatibility. Conventionally the fabrication of IDT chips and PDMS microchannels start with photolithography which transfers the design patterns to the wafers. Before that, interdigital transducers and channels are designed and drafted in a 2-D drafting software package.

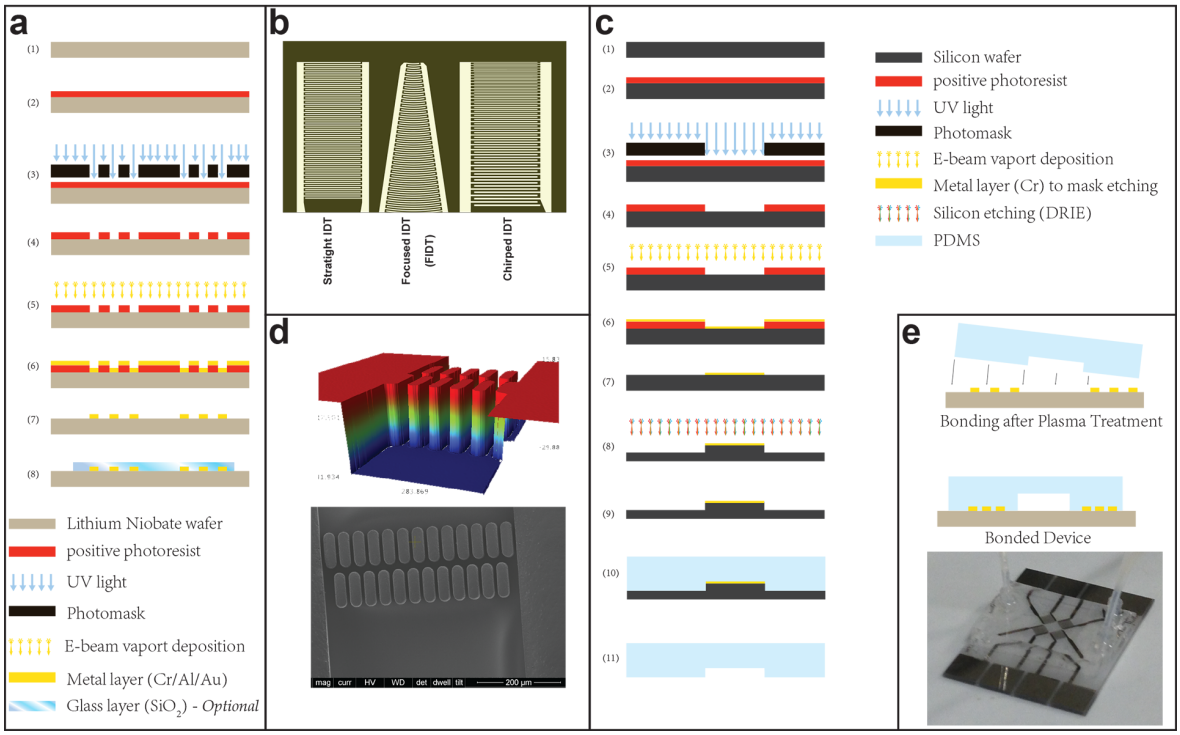

Figure 2.7: To fabricate SAW chip with IDTs, lithium niobate wafer(1) is spin coated by positive resist(2). IDT patterns are transferred by lithography using a photomask and then developed(3-4). Metal is deposited(5-6) by E-beam vapour deposition and excess metal is removed by lift-off(7). Optionally, a glass layer can be deposited (8). After dicing, single SAW chips are ready for bonding to PDMS. (b)Examples of common configurations of IDTs. (c)In this work, to fabricate PDMS microchannels, Si wafer was spin-coated by positive resist, exposed to UV through the photomask and developed(1-4 respectively). Then, a thin film of Cr covered the patterns by E-beam deposition and lift-off(5-7). Thin Cr layer allowed for deep etching by DRIE(8) and achieving the complete mould(9). By soft lithography, i.e. pouring PDMS onto the mould(10), heat treatment and peeling it off, PDMS chips are complete(11) and ready for bonding. (d)Optical profilometry and scanning electron microscopy (SEM) images shows successful fabrication of deep channels with complete micropillars which are essential in experiments of Chapters 4 and 5. (e) PDMS and SAW chips are treated by plasma and then bonded together. The final device with connections and tubing is shown.

2.6.1 SAW Device Fabrication

The main design criteria of SAW device are the target frequency/wavelength because, for most applications such as patterning and trapping, they dictate the particle manipulation regime. Knowing or selecting either of them (see Equation 2.29), we can obtain the width and spacing of the electrode fingers. Other essential factors are the overlapping length of fingers (known as IDT aperture) and the number of finger pairs (also known as IDT length) (see Fig. 2.6g). These two parameters are optimised based on minimum power reflection and impedance mismatching of the IDT [204] along with geometrical requirement arising from the microfluidic application.

Upon completion of the design of the IDTs considering above criteria and factors, SAW chips complete with the inclusion of connection pads and bus bars and alignment with the microchannel design. The 2D design can be directly transferred to wafers from the digital

image, however, usually a photomask is developed; thus, the number of photolithography replications from single design will be unlimited.

Fig. 2.7a schematically shows the fabrication steps starting with the spin coating of photoresist on a lithium niobate wafer. The designed patterns of IDTs are then transferred to the photoresist by conventional UV lithography. Instead of direct writing from a digital file, we use a photomask due to its convenience, speed of fabrication and reproducibility. After UV exposure of the photoresist, depending on its polarity it will be cross-linked: Negative photoresist will be cross-linked and polymerised at regions exposed to light, so in the developing stage, a chemical developer dissolves and washes away the unexposed resist material. The desired patterns then remain on the wafer. Conversely, the positive resist is dissolved by the chemical developer from the UV-exposed regions, then the unexposed regions will remain. For IDTs, as the aim is to metallise (and later electrically charge) the substrate due to its higher resolution, positive resist is used.

After development, the metal layer is deposited and selectively lifted off. Aluminium (Al) and gold (Au) were used for their excellent conductivity on top of a thin adhesive layer of chromium (Cr). The deposition step uses the electron-beam vapour deposition method for its uniform thin film deposition quality and anisotropic deposition that enables lift-off. In the lift-off process, chemical solvent attacks non-UV-exposed photoresist, dissolves it and along with that lifts off and remove metal from undesired regions. The remaining metal on the LN water will be only IDT circuits, connection bars and pads. Optionally, an extra layer of glass (SiO_2) is often deposited on the 1DT area to provide extra protection against corrosion and facilitate bonding to PDMS. At this stage, the wafer fabrication is completed, and individual chips are cut-out using a high-speed dicing saw and single IDT chips can be characterised by visual microscope inspection and measuring their S parameters using a Network Analyser.

2.6.2 Microchannel Fabrication and Bonding

In addition to the previously mentioned advantages, PDMS has an excellent mould release property that makes it ideal for the micro-moulding process. The process of replicating micron-sized features and patterns on PDMS using a solid mould is called *soft-lithography* emerged in the early 90s, and it greatly helped the advance of microfluidic and lab on chip systems especially in research and development. To fabricate a mould for PDMS castings, 2D patterns of the microchannels, chambers and other associated patterns are transferred to a resist-coated Si wafer using conventional UV lithography (Fig. 2.7c).

Generally, negative resists are used, and after developing, the etching creates an inverse of the channel designs with a certain height that is equivalent to the channel height on the PDMS chip. In this thesis, a packed bed of microparticles with sizes about 7 microns or larger needed to form in the channel; so a row of tightly posed small micropillars were designed to hold and retain this packed bed (see an example in Fig. 2.7d). For this reason, a modified

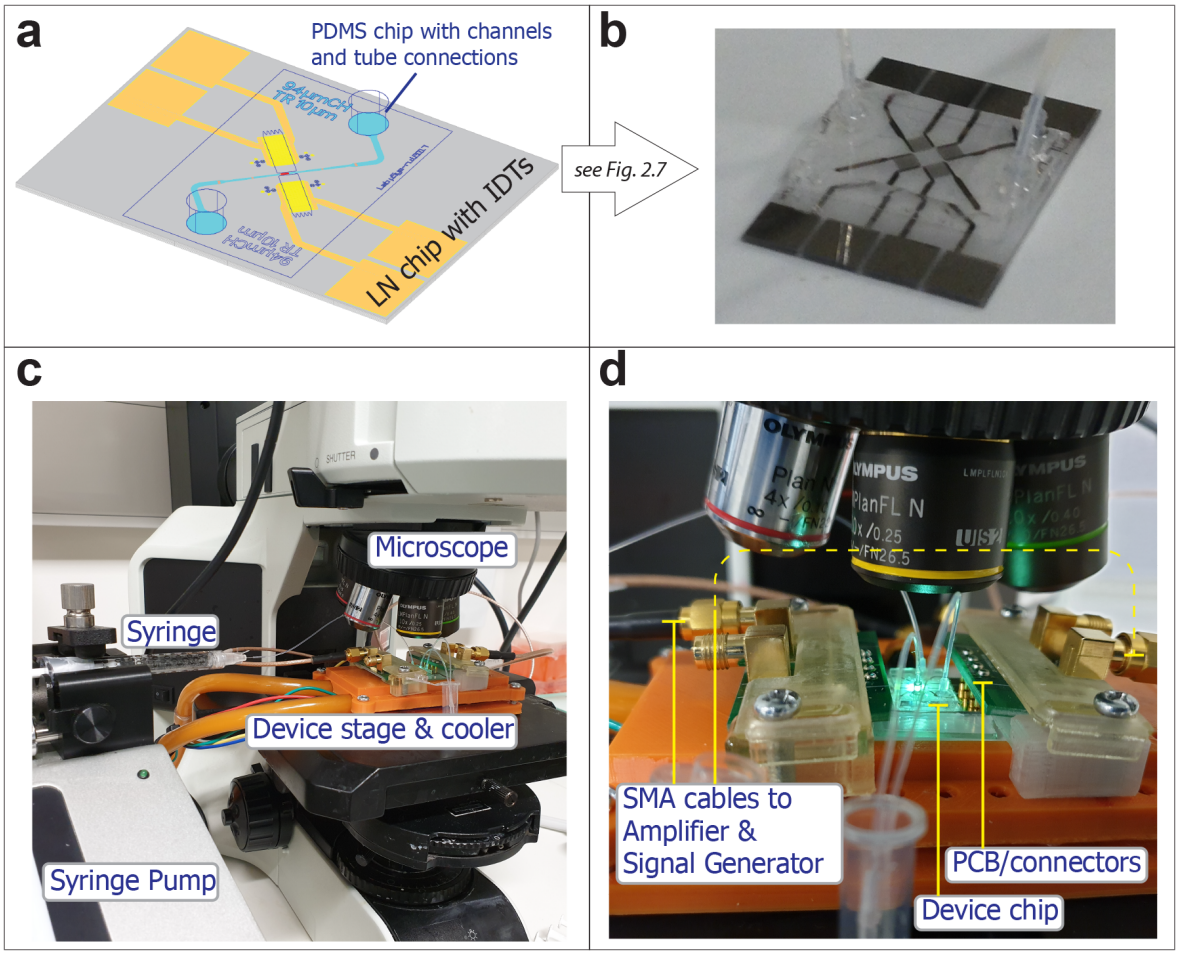

Figure 2.8: (a) CAD design of a device used in this work, Chapters 4 and 5, for trapping of nanoparticles (SWANS). Single outlet version is shown here for clarity. (b) Fabricated chip after processes described in Fig. 2.7. While the fabricated chip has 4 IDTs, only those perpendicular to channel as shown in (a) are always activated. (c) Experimental set-up showing the assembled chip with tubes connected to a syringe, containing nanoparticle sample, under a fluorescent microscope. Cooler set-up depicted here (orange stage and tubes) is only activated and used for sensitive biological samples. (d) Close-up view of the experiment device chip, with PCB board used for connecting SMA cables to IDT pads. SMA cable are connected to an amplifier and a signal generator at the other end that provide oscillating signal for IDTs, to generate surface acoustic wave.

fabrication approach, instead of using negative resists, were used. UV lithography printed the channel designs on a positive-resist coated wafer. Similar to the IDT fabrication process, e-beam deposition proceeded lithography with a thin layer of chromium. After lift-off, while Cr acted as an etching mask, deep reactive ion etching (DRIE) etched the water to the desired depth. Using a very thin layer of positive resist ($\sim$ 1 µm) helped to achieve high resolution and Cr permitted for deep etching as the etching rate of Cr is considerably lower than Si (e.g. a 75 nm Cr layer allows for 100 um depth of Si etching). DRIE is an established deep etching method where repeated cycles of silicon etching (using SF_6 as etchant) and passivation (by depositing C_4F_8) achieve required depth with a near-vertical anisotropic wall. At this stage, the microfabrication process of the Si mould is complete.

Upon completion of silicon mould fabrication, the soft lithography can be done by pouring a mixture of PDMS and its curing agent (the ratios depend on the desired stiffness or flexibility, commonly 10: 1 is used) into the mould. After casting the PDMS as it is a thermoset polymer, heating speeds up the cross-linking of the siloxane monomer chains, forming a flexible rubber-like solid polymer. At this stage, PDMS channels are ready to be cut and peeled off the mould (Fig. 2.7c). Soft lithography is cheap and very flexible as several different designs can be produced at the same time, moreover with theoretically unlimited reproduction. Although its reproducibility may not be comparable with mass-production methods, its low cost, flexibility and simplicity make it the favourite method in microfluidic, particularly among researchers.

Finally, when both SAW chip (the IDT) and microchannel (the PDMS chip) are fabricated, they are ready for bonding to make a sealed SAW-based microfluidic device (Fig. 2.7e). The PDMS chip is appropriately punched at inlet and outlet points, and then both chips are treated by air/oxygen plasma, so the deposited surface of LN and imprinted side of the PDMS block are activated and energised for binding. Surface treatment by air/oxygen plasma creates hydroxyl groups on both PDMS and glass layer (deposited on LN), so upon close contact of these to surfaces (immediately after plasma treatment) an intermolecular waterproof and irreversible bond is formed between PDMS and glass-coated LN chip. During the bonding process, precise alignment of IDTs and the channel is crucial and carefully monitored under a stereo microscope. Fabrication is complete at this point; attaching the connection tubes and fittings make the device ready for experiments (see a demonstration of a complete device and experimental set-up in Fig. 2.8).

Chapter 3

Trapping and Patterning of Large Particles and Cells in the Acoustic Field

3.1 Overview

Trapping and patterning cells individually and in single wells provides enormous opportunities for studying them while preserving information that is lost in conventional laboratory approaches. In single-cell analysis, cell to cell communication and drug screening can be studied and used for tuning tissue engineering applications and further knowledge in stem cell research could be obtained. Acoustic forces have been very successful in achieving single-cell trapping as they only exploit the physical properties of the cells, cell pre-treatment or modification is not required.

When an acoustic wave approaches the suspended particles, the wave gets scattered, and this scattering can generate two types of forces; primary and secondary acoustic radiation forces. Primary acoustic radiation forces are the direct result of scattering of the wave by the particle and the secondary forces arise from the interaction between the suspended particle and other neighbour particles. In most microfluidic systems, the wavelength of the ultrasound wave required to pattern particles is usually significantly larger than the size of the particles. This results in patterning of particles in clusters at nodal points instead of single particles. By acoustically increasing the size of the particle ($d \rightsquigarrow \lambda$), i.e. increasing the frequency, interplay between primary and secondary forces can allow for locating single particles at pressure nodes (or antidones). Achieving single particle patterning requires full understanding of this interplay mechanism by investigating both primary and secondary forces on large particles in a standing wave.

In this work, a systematic numerical method is proposed that enables the investigation of particle behaviour when its size is acoustically large under 1D standing wave. In the

method presented to investigate primary and secondary force regimes for large particles, a finite element method (FEM) numerical simulation were used. Firstly, frequency response of the primary acoustic radiation force for three different materials (polystyrene (PS), PMMA and silica glass) is studied. The study identified regions of different force response defined by change in force direction influenced by resonance frequencies. Polymeric materials, PMMA and PS, show their first two resonance frequencies at sizes smaller than half a wavelength. Further, study focuses on PMMA and shows that secondary Bjerknes force is also influenced by these regions and natural frequencies. The interplay between primary and secondary forces define the patterning regime at each region.

In the first region (Region A, $0 < d/\lambda < 0.33$ for PMMA), the primary force pushes the particles to the pressure nodes while the secondary force, which are attractive at small gaps between particles, causes small clumps to form at nodal points. In the next region (B, $0.33 < d/\lambda < 0.42$ for PMMA), where the first resonance appears, the primary forces collect the particles at antinodes and the secondary forces become dramatically high. This will lead to clusters of particles to form at the antinodes. In the third region, further resonance frequencies appear, however, primary forces keep the particle at nodes, and the secondary forces, being negative, do not lead to particle aggregation. In this region the frequency range is narrow, as are the particle diameters. The range of frequencies is ideal for single-particle patterning, which is in agreement with recent experimental results of single-particle, and cell patterning demonstrated in a surface acoustic wave (SAW) based microfluidic system. However, in the case of cells, the attractive secondary acoustics forces are rather weak due to lower wave scattering. Hence, in order to obtain the same results as with particles, the cell diameter must be on the order of the wavelength for single-cell patterning to be achievable.

These finding shows how natural resonant frequencies of particles play an important role in not only frequency response of single particle, but the inter-particle secondary forces. By this effect, resonant modes shape distinct ranges of frequencies that demonstrate different patterning behaviour. A key finding that can be exploited for trapping and clustering of target particles is that the 'attractive' secondary force is exceptionally high under the influence of resonance.

3.2 Publication

The following publication was reproduced from [1] with kind permission from the Royal Society of Chemistry.

Lab on a Chip

PAPER

View Article Online
View Journal | View Issue

Cite this: *Lab Chip*, 2017, **17**, 3279

Trapping and patterning of large particles and cells in a 1D ultrasonic standing wave†

Ruhollah Habibi, Citsabehsan Devendran and Adrian Neild *

Received 19th June 2017,
Accepted 14th August 2017

DOI: 10.1039/c7lc00640c

rsc.li/loc

The use of ultrasound for trapping and patterning particles or cells in microfluidic systems is usually confined to particles which are considerably smaller than the acoustic wavelength. In this regime, the primary forces result in particle clustering at certain locations in the sound field, whilst secondary forces, those arising due to particle–particle interaction forces, assist this clustering process. Using a wavelength closer to the size of the particles allows one particle to be held at each primary force minimum. However, to achieve this, the influence of secondary forces needs to be carefully studied, as inter-particle attraction is highly undesirable. Here, we study the effect of particle size and material properties on both the primary and secondary acoustic forces as the particle diameter is increased towards the wavelength of the 1-dimensional axisymmetric ultrasonic field. We show that the resonance frequencies of the solid sphere have an important role in the resulting secondary forces which leads to a narrow band of frequencies that allow the patterning of large particles in a 1-D array. Knowledge regarding the naturally existent secondary forces would allow for system designs enabling single cell studies to be conducted in a biologically safe manner.

1 Introduction

The ability to trap and pattern individual cells and particles within a microfluidic system allows highly detailed studies into cell responses. Such single-cell analysis offers the advantage of preserving the information that is lost when population based averages are made in standard methods, especially as a population inevitably includes cells with a range of sizes and chemistries resulting in varying response and reactions to drugs or virus agents.[1,2] In addition, single-cell analysis can provide detailed information about cell–cell interaction, drug screening and a platform for tunable engineered tissues or stem cell research.[3–5] Given the nature and scope of the applications, it is perhaps unsurprising that a range of techniques have been developed to create single-cell arrays. These include passive methods which are typically dictated by the channel geometry and flow profiles,[3,4] as well as active approaches utilising optical forces,[6] magnetism,[7] dielectrophoresis[8] and acoustophoresis.[9] Whilst each of these approaches offers certain benefits, the latter, acoustic manipulation, offers excellent biocompatibility[10–13] and good on-chip integration[14,15] and as it exploits the physical properties of the particles/cells, it does not require the tagging or labelling of cells.[16]

Laboratory for Micro Systems, Department of Mechanical and Aerospace Engineering, Monash University, Clayton, Victoria 3800, Australia.
E-mail: adrian.neild@monash.edu

† Electronic supplementary information (ESI) available. See DOI: 10.1039/c7lc00640c

Acoustophoresis is the use of ultrasound in microfluidics to generate forces required to trap cells or microparticles,[17] encapsulate them in droplets,[18,19] pattern them in segregated clusters,[20,21] and gain control over their trajectories.[22–24] The required ultrasonic fields can be generated in a number of ways, but most commonly *via* bulk acoustic waves, which are used to excite fluid resonances,[25,26] or surface acoustic waves (SAW) in which patterned electrodes are driven at a frequency such that constructive interference between each pair of electrodes results in a high amplitude wave which couples into fluid volumes in contact with the substrate.[27,28] Regardless of how the waves are generated, when they impinge and are scattered by a suspended particle, forces are generated on the scattering object. This acoustic radiation force has two contributing components, firstly the primary radiation force which arises as a result of the interaction between the incident wave and the suspended matter (*i.e.* particles), in contrast to the secondary radiation force which is experienced as a result of the interactions between the scattered wave from another surface (*i.e.* particle/wall/bubble) and the suspended matter.

The vast majority of acoustofluidic systems developed for particle handling and sorting[29–31] use wavelengths which are considerably larger than the diameter of the particles being manipulated. This causes particles to cluster at defined locations within the pressure field.[32] In this scenario, the primary forces drive the particles to these locations, typically the pressure nodes in a standing wave, further reinforced by the secondary forces, which are predominantly attractive in this regime, which assists the formation of these clusters.[33]

View Article Online
Paper Lab on a Chip

However, as Collins *et al.* noted,[9] the unique requirement for acoustic single cell patterning is that the primary force should create the patterning, whilst the secondary force must be weak enough to not promote particle clumping.

In this work, we examine the relative importance of primary and secondary forces for particle and cell manipulation over a range of particle sizes, up to half the wavelength, in a one-dimensional sound field. For the primary force, whilst most previous studies assume a small particle size,[16,34–37] Hasegawa's work[38] is very helpful as an analytical approach capable of predicting the acoustic radiation force on an elastic solid sphere in both one-dimensional standing and travelling waves, valid for any size range. A second useful feature of previous studies is the influence of viscosity. Doinikov demonstrated that viscosity (most studies assume an inviscid fluid) only significantly affected the forces generated on small size particles[36] and Muller *et al.* compared the magnitude of the primary force with drag from acoustic streaming in a viscous fluid, showing that the drag will not dominate for diameters larger than 0.05 of the wavelength.[39] As such, we will assume an inviscid fluid and neglect the influence of acoustic streaming.

The secondary forces have also been studied widely, originally by Bjerknes who examined the forces between two oscillating bubbles.[40] Furthermore, there have also been studies of bubble–particle interaction[41,42] and two small rigid particles.[43] None, however, provide a basis for understanding the interparticle forces as the particle size approaches the wavelength.

Collins *et al.*[9] demonstrated experimentally that single cells and particles can be patterned in a 2D sound field; however, they observed a link between the success of patterning and the particle size. To understand this link, albeit in a simpler 1D sound field, we have utilised numerical simulations to examine the primary and secondary forces over a range of particle sizes. We demonstrate the existence of distinct regimes of behaviour, with shifts in the direction of the forces as the particle's resonance conditions are approached. As we employ a 1D field, to apply the findings to one cell per well (OCPW), we must assume a physical restriction in the second dimension. Based on this assumption, we use simulations to demonstrate that the likelihood of successful OCPW particle capture is highly dependent on which of these regimes are at play, as well as the nature of the particle or cell being captured.

2 Theory

Perturbation theory is applied to obtain the second order non-zero forcing terms, the resultant acoustic radiation forces.[44,45] In this approach the pressure field is assumed to consist of the stationary part P_0, first order P_1, and second order P_2 expansions, in which P_1 and P_2 are assumed to be time dependent and harmonic. This expansion to the second order is sufficient when the perturbation ε is small. Considering the stationary state density ρ_0 and velocity v_0 (which is equal to zero), the pressure, density and velocity fields can be expanded as:

$$P = P_0 + \varepsilon P_1 + \varepsilon^2 P_2 + \ldots, \tag{1a}$$

$$\rho = \rho_0 + \varepsilon\rho_1 + \varepsilon^2\rho_2 + \ldots, \tag{1b}$$

$$\boldsymbol{v} = \boldsymbol{v}_0 + \varepsilon\boldsymbol{v}_1 + \varepsilon^2\boldsymbol{v}_2 + \ldots. \tag{1c}$$

Implementing eqn (1) alongside the continuity and the Navier–Stokes equations, and taking the time average ($\langle\rangle$ denotes a time average operator) of the terms over a harmonic cycle, yields:

$$\rho_0\nabla\cdot\langle\boldsymbol{v}_2\rangle = -\nabla\cdot\langle\rho_1\boldsymbol{v}_1\rangle \tag{2a}$$

$$\eta\nabla^2\langle\boldsymbol{v}_2\rangle + \beta\eta\nabla(\nabla\cdot\langle\boldsymbol{v}_2\rangle) - \nabla\langle P_2\rangle = \langle\rho_1\partial_t\boldsymbol{v}_1\rangle + \rho_0\langle(\boldsymbol{v}_1\cdot\nabla)\boldsymbol{v}_1\rangle. \tag{2b}$$

While the time average of the static and first order components of the fields equates to zero, the time average of the first order products or second-order components of the velocity and pressure fields is non-zero and thus, $\langle P_2\rangle$ contributes to the acoustic radiation force.[44] This force is derived from the integration of the second-order pressure field over the surface of the particle (in an ideal inviscid fluid). For this reason, it is also a time averaged phenomenon and as such acts over numerous harmonic cycles, allowing a steady migration of particles in a rapidly oscillating sound field. The resulting force is:

$$\langle\boldsymbol{F}\rangle = \left\langle\int_{S(t)} P_2(-\boldsymbol{n})\mathrm{d}\boldsymbol{S}\right\rangle. \tag{3}$$

Here, $\boldsymbol{n}$ indicates the normal vector facing outward to the surface of the particle, S. However, as the surface of the particle $S(t)$ deforms and moves under the effect of the incident field, integration over this surface is problematic. Instead, by applying Reynolds' transport theorem and expanding the second-order pressure field,[45] the acoustic radiation force on the particle is determined, by integration over the unperturbed surface, in this form, S_0:

$$\langle\boldsymbol{F}\rangle = \int_{S_0}\left(\frac{\rho_0}{2}\langle v_1^2\rangle\boldsymbol{n} - \frac{1}{2\rho_0 c_a^2}\langle P_1^2\rangle\boldsymbol{n} - \rho_0(\boldsymbol{n}\cdot\boldsymbol{v}_1)\boldsymbol{v}_1\right)\mathrm{d}\boldsymbol{S}, \tag{4}$$

where c_a is the wave speed in the fluid. This formula uses only the first-order velocity and pressure fields applied over the stationary surface of the particle. The integrand has three distinct parts. The first two terms make up the momentum flux in/out of particle volume surface where the former is the kinetic and the latter is the hydrostatic energy, contributing to the force. The third term is the convective momentum flux so the particle's motion and surface fluctuation are taken into consideration. In eqn (4), the first-order acoustic pressure and velocity fields have two contributing parts

View Article Online
Lab on a Chip Paper

corresponding to the incident and scattering effects, as expressed here for the velocity term:[46]

$$\boldsymbol{v}_1 = \boldsymbol{v}_\mathrm{i} + \boldsymbol{v}_\mathrm{s}, \tag{5}$$

Accordingly, the squared velocity term can be written as:

$$v_1^2 = v_\mathrm{i}^2 + 2v_\mathrm{i}v_\mathrm{s} + v_\mathrm{s}^2 \tag{6}$$

The scattered wave v_s is also a first-order approximation in this case. This approach was used by Yosioka and Kawasima[16] and later by Gor'kov[34] to derive the formula of the force on an elastic spherical particle in an acoustic wave.

However, they assumed that the particle is much smaller than the wavelength, ($d \ll \lambda$),[46] and as such the scattered–scattered term is very small compared to the incident and scattered–incident fields, $v_s^2 \ll v_i v_s$ (eqn (6)). Hasegawa and Yosioka[50] also broke the potential field down into the incident and scattering components and then expanded them analytically using spherical Bessel and Hankel functions. Their approach provided an analytical solution for the force on elastic particles with an arbitrary size compared to the wavelength. Similarly, Doinikov[36] derived the force relations within a viscous fluid. However, for large spheres, the scattered field cannot be neglected, so a higher order of approximation is required for an analytical solution.

In summary, for very small spherical particles, Gor'kov's[34] solution provides sufficient accuracy and the expression of force is convenient and widely used; however for larger particles, it cannot provide accurate results as it ignores the scattered–scattered field effects. Using perturbation theory, we are able to express the force with known first-order terms. As our subject particles are in the order of the wavelength, we must consider the scattering effects as well. In this study, we chose to adopt a finite element method (FEM) to solve the problem directly. Glynne-Jones *et al.*[46] have used this approach and shown that calculating the acoustic radiation force (ARF) on large size particles using FEM is in good agreement with Hasegawa's[38] analytical approach.

In this work, we will apply a similar approach to that in Glynne-Jones' work,[46] using an axisymmetric model of a particle in cylindrical coordinates, to first compute forces on a single particle in a one dimensional (1D) field, followed by the extension of this approach to investigate secondary forces between two neighbouring identically sized spheres.

3 Method

3.1 Establishing the FEM model

To construct the finite element model, COMSOL Multiphysics® was employed. The acoustic wavelength λ in the fluid is set to 100 μm and all other geometrical parameters such as the particle size and particle position are made proportional to the wavelength. All spatial parameters including the size, position, gap between pairs of particles and position of the gap (centre of the gap) are normalised with respect to λ. The solid material for the particle is selected as poly(methyl methacrylate) (PMMA) while other materials such as polystyrene (PS) and silica glass (SG) will also be used for comparison. The basic parameters used in the model are listed in Table 1. Material data are taken from the COMSOL library, with the exception of polystyrene.[51]

The size of the particle is used as the basis for a parametric study, with the force calculated for a range of sizes, from very small relative to the wavelength ($0.03 \times \lambda$) up to one wavelength. A 2D axisymmetric geometry model was used, with a fluid domain of dimensions as listed in Table 1. The fluid and solid domains were meshed with free triangular elements (maximum size limited to 0.4 μm and $0.1 \times R_\mathrm{p}$, respectively). The growth rate was set to 1.05 for the fluid domain and 1.3 for the solid domain. The interface at the solid–fluid domains (the surface of the spherical particle) was meshed using an edge mesh (0.1 μm) to accurately capture the physics arising from the scattering effects. The standing acoustic wave was defined as a plane wave along the axisymmetric z-axis as $P = P_0\cos(kz)$ (with P_0 = 100 kPa) and the boundary conditions: cylindrical wave radiation was used to transmit out through the modelled domain with minimal reflection (Fig. 1). The maximum ARF is experienced when the sphere's centre is located at $z = +\lambda/8$, with z = 0 located at the pressure antinode. The pressure field conditions are given in Table 1, and all the resulting forces are expressed in nN throughout this work. The model set-up for a single particle was benchmarked against the approach and the model set-up utilised by Glynne-Jones *et al.*[46] to ensure accuracy and conformity.

3.2 Particle–particle interaction

Following the examination of ARF on a single particle for a wide range of sizes (analogous to a range of frequencies), two equally sized spheres were modelled to represent two proximal particles in a 1D field. As the aim is to pattern single particles individually at each node, given the fact that in a 1D field, the inter-node distance is half a wavelength ($\lambda/2$) and the limiting size of the particle is $d = \lambda/2$.

The model schematic is depicted in Fig. 1. Here, it can be seen that neighbouring particles are modelled starting with a minimum gap ($G = \lambda/100$) around the antinode, and increasing this gap to investigate the influence of the other particle's presence. Each particle is swept through the axis toward the nearest node and slightly further to realize the effect of the gap on the acoustic force. Further, simulations also vary the location of the centre of this gap away from the antinode. The particle–particle interaction study was meshed in a similar manner as the previously discussed single particle study (section 3.1), accommodating for both solid–fluid interfaces present now.

4 Results and discussion

4.1 ARF on single particle: primary force

Fig. 2 shows the axial force on an elastic sphere of three different materials, PMMA, PS and SG, positioned at a $\lambda/8$ distance from the 1D standing wave's node/antinode, as the

Table 1 Basic parameters of the model. Material data are obtained from the COMSOL material library unless otherwise stated

Parameters	Symbol	Value	Unit
Fluid domain			
Water			
Wavelength	λ	100	μm
Density[47]	ρ_0	997	kg m^{-3}
Speed of sound[47]	c_0	1497	m s^{-1}
Domain height (along z)	L	1*λ	μm
Domain width	W	$\frac{1}{2} * \lambda$	μm
Frequency	f	14.97	MHz
Wavenumber	k	6.28×10^4	m^{-1}
Acoustic pressure amplitude	P_0	100	kPa
Solid domain			
Domain dimensions:			
Particle diameter	d	Parametric, $d = d(\lambda)$	μm
Particle radius	R_p	$d/2$	μm
PMMA			
Density	ρ_p	1190	kg m^{-3}
Speed of sound (long.)	c_p	2270	m s^{-1}
Modulus of elasticity	E_p	3.0	GPa
Poisson ratio	ν_p	0.4	—
Polystyrene			
Density[39]	ρ_{ps}	1050	kg m^{-3}
Speed of sound (long.)[39]	c_{ps}	2350	m s^{-1}
Modulus of elasticity[a]	E_{ps}	3.69	GPa
Poisson ratio[48]	ν_{ps}	0.35	—
Silica glass			
Density	ρ_{si}	2203	kg m^{-3}
Speed of sound (long.)	c_{si}	5972	m s^{-1}
Modulus of elasticity	E_{si}	73.1	GPa
Poisson ratio	ν_{si}	0.17	—

[a] Calculated from the bulk modulus (K) as $E_{ps} = 3K_{ps}(1 - 2\nu_{ps})$ from ref. 48 and 49.

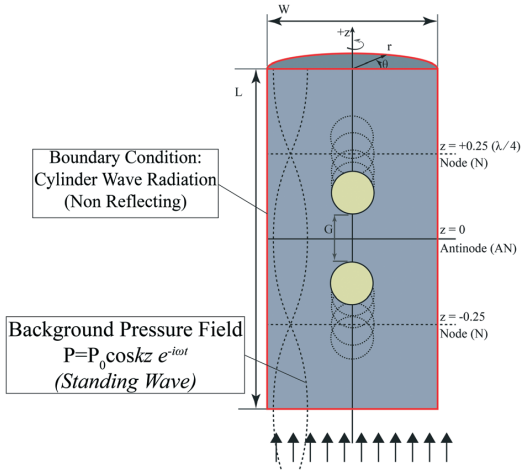

Fig. 1 Schematic of the axisymmetric FEM model defining the field and boundary conditions. The figure shows two neighbouring particles while their face-to-face gap (G) increases symmetrically to investigate their interaction.

normalised size of the particle (d/λ) is increased from 0 to 1. In all cases, the incident pressure amplitude of the 1D wave is 100 kPa. From Fig. 2(a), it is observed that for the PMMA particle the force increases gradually with size until a local maximum at 0.25 and as the size increases further there is a sharp drop in force to a minimum of about −7 nN at size 0.4, followed by a rapid rise to the second maximum with a magnitude of +7.92 nN at size 0.425. It is noted that a positive force means that the particle is pushed towards the neighbouring pressure node while a negative sign indicates that the particle will be moved towards the nearest antinode.

As larger sizes of PMMA is considered, we observe a repeating pattern of minima and maxima points occurring at certain (normalised) sizes which can be correlated to certain distinct frequencies. Hasegawa and Yosioka[50] attribute these points to resonance frequencies of an elastic sphere. We can see similar patterns in Fig. 2(b) and (c) for the other materials considered.

The resonance frequencies (natural frequencies or eigenfrequencies) of an elastic sphere immersed in a fluid[69] are proportional to Young's modulus and the inverse of a polynomial function of the Poisson ratio, $f(\nu) = a_i\nu^i + a_{i-1}\nu^{i-1} + \cdots + a_1\nu + a_0$:[52]

$$\omega_n \propto \sqrt{\frac{E}{f(\nu)}} \tag{7}$$

As a result, the natural frequencies for the PS particle are higher than those of the PMMA particle, as PS has a lower Poisson ratio and larger E. Whilst silica, with a much higher stiffness, has a larger resonant frequency, indeed, Fig. 2(c) only shows two extrema within the range of $d/\lambda < 1$. It is clear that these eigenfrequencies strongly affect inter-particle forces and as such the patterning that can be expected. Thus, it is very important to understand the effect of the stiffness matrix components of the particle material. When damping effects are considered, the ARF trend remains similar to that of a linear elastic solid model with the exception of a reduced magnitude at the resonating sizes (frequencies) (see Fig. S1 in the ESI†).

The area of interest in manipulating particles, and later, cell trapping in a 1D field is limited to sizes less than half a wavelength due to geometrical constraints. Namely, in order to obtain one particle per acoustic force well, which is spaced at half wavelength intervals, the particles need to be less than half of a wavelength to physically fit in the available space, as indicated in Fig. 3. Hence we focus on this part of the force–size plots. As presented in Fig. 2, there are three distinguishable regions in the range from 0 to 0.5:

Region A: the ARF or the primary force is positive, and as a result, particles will be pushed towards the pressure nodes. For PMMA and PS, this region covers very small to medium sized particles. However, the whole size spectrum of silica

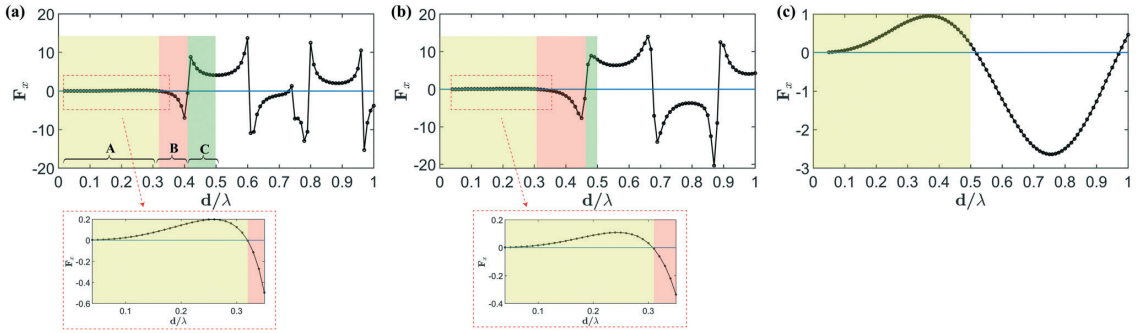

Fig. 2 Acoustic radiation force acting on (a) PMMA (b) PS (c) and silica glass (SG) spherical particles in the 1D field for sizes up to $d = \lambda$. All forces are in nN as a 100 kPa pressure amplitude is applied for all cases. ARF for other materials and sizes can be found in ref. 38. In region A (highlighted in beige) the primary force is positive but no resonance is observed. In region B (pink) the primary force is negative thus pushing particles to the antinodes and the first resonance is observed. In region C (in green) positive primary force pushes the particles to the nodes and the second resonance appears. PMMA and PS show these three distinct regions in the range $d < \lambda/2$ but SG only shows region A in this range. The insets show enlarged region A for PMMA and PS for clarity.

glass particles (small to large) fall in region A (highlighted in beige).

Region B: the ARF is negative, and as a result, it pushes the particle to the antinode. This region (highlighted in pink) occurs for both PMMA and PS.

Region C: The ARF/primary force is positive, and as a result, it pushes the particle to the node (highlighted in green).

These regions, whilst being identified for single particles in a fluid, become relevant when we turn our attention to pairs of particles and the consideration of Bjerknes secondary forces experienced as a result of the second particle's presence.

These three distinct regions are observed in PMMA and PS, while SG only demonstrates behaviour typical of region A (see Fig. 2). However, as region C is comparatively narrow for PS, PMMA was chosen to examine the Bjerknes secondary forces to better exhibit the different types of particle–particle interactions.

4.2 Interparticle or Bjerknes secondary force

To investigate the role of secondary forces we add a second particle to the simulations as described in section 3.2, whereas the total force acting on the particles is examined in order to determine whether attraction or repulsion occurs (Fig. 1).

Each sphere scatters the incident field around it, which in turn results in the time-averaged phenomenon of radiation force–primary force (F_{prim}). This respective (scattered) field also deforms and changes the (scattered) field of other neighbouring spheres, if this deformation effect could be completely separated from the primary force scenario (scattering of incident field by single particle), that is this net scattered–scattered field contributes to the net inter-particle or Bjerknes secondary force (F_{sec}). By determining the total and primary forces, the secondary force can be calculated indirectly:

$$F_{\text{total}} = F_{\text{prim}} + F_{\text{sec}} \Rightarrow F_{\text{sec}} = F_{\text{total}} - F_{\text{prim}} \quad (8)$$

where F_{prim} indicates the primary force measured in a single particle scenario and F_{total} is the total acoustic force on each particle in the presence of the other one. F_{sec} is denoted as the Bjerknes secondary force, in this case.

Fig. 4 shows the primary and total forces on single and two PMMA particles at different positions along the wave axis. Spheres with very small sizes (here represented as d = 0.03) follow their primary force field even when they are very close. For sizes 0.10 and 0.20, their scattering effect on the other particle field is notable but not dominant, with the primary force still significant enough to push them to the corresponding nodes. For size 0.25, we see that when the particles are close together (gap $<$ 0.05), the total acoustic radiation force F_{total} acts in the opposite direction of the primary force, thus resulting in the attraction of particles.

As such, the trend in region A is that as the particle size is increased, F_{sec} increases and it acts in the opposite direction of the primary force, and as such acts to attract the particles together. At a size equal to 0.25, we can see that this effect

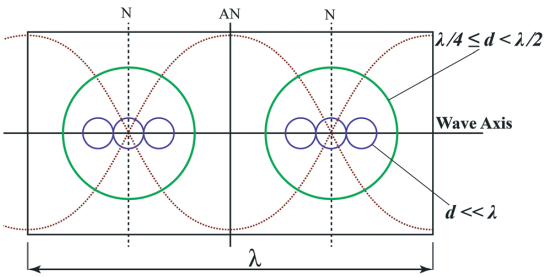

Fig. 3 In a 1D standing wave field due to geometrical constraints, one particle per node is only possible for sizes less than $\lambda/2$. If the sizes are much less than $\lambda/4$ (small and very small particles) the clusters are shaped around the nodes due to inter-particle attraction around them.

View Article Online
Paper Lab on a Chip

dominates over the primary force for gaps that are small enough.

For larger sizes, moving into region B, the trend changes significantly. The primary forces reverse in sign, acting to move the particles towards the antinode, whilst the secondary force continues to act in bringing the particles together, hence they act in unison with each other. In addition, the magnitude of the secondary force is considerably significant at small gap sizes.

For PMMA particles of size 0.45 located in region C, the total force pushes particles toward the nodes, which is the same as the primary force does with a small deviation. Secondary forces are relatively small and act repulsively. At this size, the corresponding frequency is very close to the natural frequency, resulting in an intensified acoustic radiation force (positive direction), that is, the primary force is dominant and acts to position the particles in the local pressure nodes.

4.3 Bjerknes secondary force at other positions

Thus far, we investigated two particles separated by a gap, the centre of which is at the antinode and varied the gap size about the gap centre, C_g. In doing so, we observe that the regions of different behaviours align with the resonant frequencies of individual particles. We now examine the forces acting on the two neighbouring particles which are centred at positions other than the antinode (Fig. 5). In Fig. 6 plots are given for three particle sizes, (0.25, 0.35 and 0.45) one from each of the identified regions, and for each, we plot the secondary force as a function of C_g as it is moved from the antinode to the node (0 to 0.25). In each case we do this for a minimum of three gap sizes.

The attraction force is defined to determine if the total net secondary force of the two particles results in attraction or repulsion (Fig. 5(b))

$$\boldsymbol{F}_{\mathrm{sec}})_{\mathrm{A}} = \boldsymbol{F}_{\mathrm{sec}} \text{ on Particle A} = \boldsymbol{F}_{\mathrm{total_A}} - \boldsymbol{F}_{\mathrm{prim_A}} \tag{9a}$$

$$\boldsymbol{F}_{\mathrm{sec}})_{\mathrm{B}} = \boldsymbol{F}_{\mathrm{sec}} \text{ on Particle B} = \boldsymbol{F}_{\mathrm{total_B}} - \boldsymbol{F}_{\mathrm{prim_B}} \tag{9b}$$

$$\boldsymbol{F}_{\mathrm{att}} = \boldsymbol{F}_{\mathrm{sec}})_{\mathrm{B}} - \boldsymbol{F}_{\mathrm{sec}})_{\mathrm{A}} \tag{9c}$$

When $\boldsymbol{F}_{\mathrm{att}}$ is positive it means particle B is pushed rightward, thus secondary forces are attractive in nature, whilst a negative sign indicates a repulsive force. It is shown in Fig. 6(a and b) that $\boldsymbol{F}_{\mathrm{att}}$ decreases as the centre of the gap is moved away from the antinode, and is negative in the vicinity of the node. It appears that the main difference between these two particle sizes representing region A and B is that particles within region B experience much larger secondary forces.

The representative of region C, size 0.45, shows interesting behaviour. Fig. 4(f) revealed that two 0.45 sized spheres positioned around an antinode will be forced to their counterpart nodes and repel each other despite being in close proximity (C_g of $\sim$ 0.01). In addition, Fig. 6(c) shows that the secondary force is repulsive even around the node (C_g = 0.25). This means that two neighbouring particles of this size are not brought together making them ideal candidates for single particle trapping.

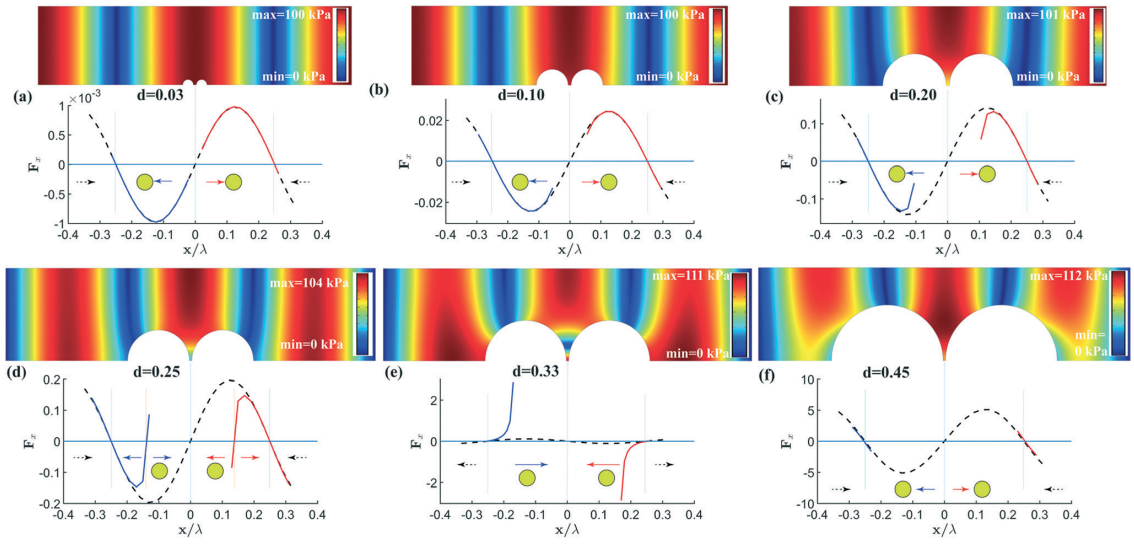

Fig. 4 Force *vs.* position for different sizes: black dashed line shows primary forces on single particles along their positions sweeping from a node to the opposite node for different sizes, (a) d = 0.03λ, (b) d = 0.10λ, (c) d = 0.20λ, (d) d = 0.25λ, (e) d = 0.33λ and (f) d = 0.45λ. Red and blue solid lines show the total force on particles A (top/right side) and B (down/left side), respectively, as their gap increases. All forces are in nN with 100 kPa pressure applied.

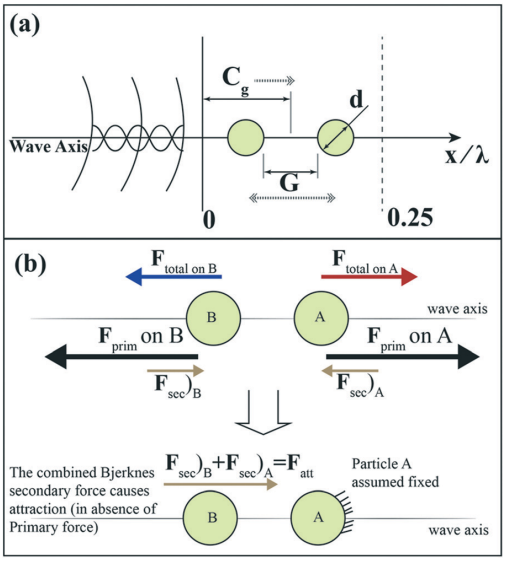

Fig. 5 (a) The centre of the gap was moved along the axis line to evaluate the secondary force at the other positions. (b) The attraction force (F_{att}) is shown as the sum of the absolute net secondary forces on each particle, as if particle A is fixed and this force pushes B toward A, in this way, the positive sign (arrow pointing to the right side) indicates attraction and the negative sign (arrow pointing to the left side) indicates repulsion.

In Fig. 7, we can see the impact of the normalised size (or equivalently the frequency for a certain size) on the secondary force for different gaps around the antinode. Fig. 7 demonstrates that the attraction force follows a similar pattern to that of the primary force with change in size, however close to the resonance size (frequency), a large surge in its magnitude is observed resulting in a significantly larger force as compared to the primary force. Its magnitude then drops with the increase of the normalised size followed by its approaching zero after the second resonance size (frequency). Hence, at these larger sizes, its magnitude is very small compared to the corresponding primary force.

Thus far, we have analysed the resonant behaviour of individual particles demonstrating a change in the sign of the primary force at resonant sizes. For the analysed pairs of particles, the primary forces acted on particles in regions A and C such that they migrate to the pressure nodes, whilst region B particles engender forces which act to move them to the antinodes. In addition to these primary forces, the secondary forces were examined, showing that particles in regions A and B follow a similar trend to the forces which are typically attractive, whilst in region C particles experience repulsive secondary forces across a full range of locations. With these trends isolated, and the link with the size regions established, we now turn to the central question: which of these particle sizes are best suited for single particle trapping? To assess this, we examine the combination of primary and secondary forces acting on a pair of particles whose starting location falls into a wavelength of the pressure field. In an ideal situation, these two particles would move to adjacent nodes or antinodes, and as such be held at positions separated by half a wavelength. This would mean that if the concentration of particles is suitable, one particle per force minima can be expected. As discussed previously, for a certain size range this is deterministically achievable. Sizes from region C are an ideal candidate for this. However, this range is very narrow and similar to the findings of Collins *et al.*[9] for an elastic solid. In contrast, the majority of particle sizes will present a more complex picture. To examine this, we place a pair of particles from each size region, in a standing wave in a range of different gap centres, and vary the gap size. At each location we examine where the particle will move to, and the outcomes are plotted in Fig. 8.

In Fig. 8, each line in the figure corresponds to a different gap centre. Within each of these sub-images the shading indicates where particles at each starting location will migrate to. In the case of the region A particle, d = 0.25, each sub-image has a central red box. Particles starting within this box will be dominated by secondary forces and thus attracted to each other (the centre of this red box is also the centre of the gap between the two particles). The size of the box is indicated to the left of each sub-image. It should be noted that a box size of 0.26, for this particle which has a size of 0.25, means that the maximum gap between the particles at which attraction occurs is 0.01. Outside the red boxes, particles migrate to their nearest node, as such one particle per well is achieved. Note that had we examined a smaller particle size

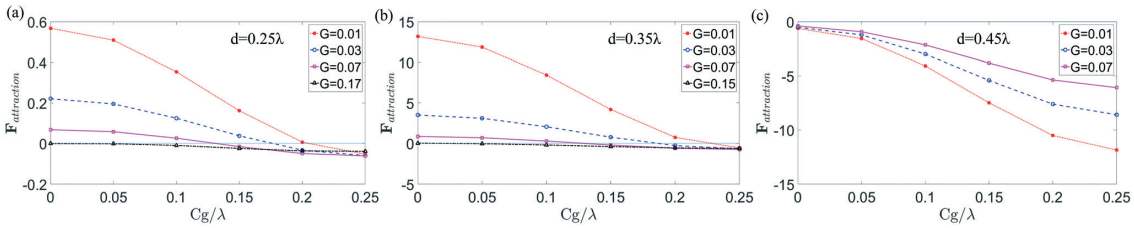

Fig. 6 Attraction force acting on particle B toward A with different gaps (G) and with the centre of the gap (C_g) at different positions from the antinode to the node. Each size represents its corresponding region, (a) d = 0.25λ for region A, (b) d = 0.35λ for region B (c) and d = 0.45λ for region C. In the third region, the attraction force is negative and hence becomes repulsive and its repulsion even increases when C_g is shifted toward node. All forces are in nN with 100 kPa pressure applied.

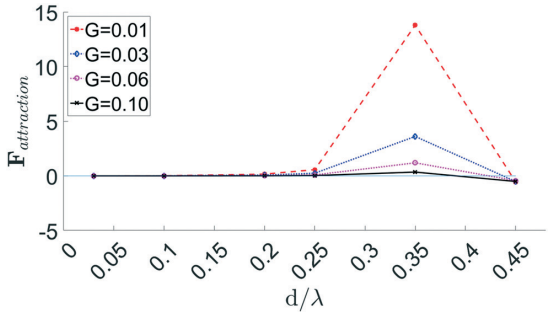

Fig. 7 Attraction force (and proportionately the Bjerknes secondary force) between two identical size spheres *versus* their normalised size at different gaps. All forces are in nN with 100 kPa pressure applied.

in region A, then there would also be the possibility that both particles could start in locations such that their nearest node is common. The physical size of the 0.25 particles makes this scenario impossible. If the assumption of two particles per half wavelength is presumed, the probability that the particles are attracted to each other can be approximated to the size of the attraction box minus the size of the particle divided by 0.5 (half the wavelength) minus the particle size. If we assume the centre of the gap is evenly distributed, we can say that the probability that they collect in different nodes is approximately 70%.

In the case of region B, there is a large attractive zone in most cases, and outside of which the particles are collected in the nearest antinode. In the case of a gap centre located at the node, the particles repel each other. Taking the same approach to estimate the single particle trapping probability, a value of 58% is obtained. Based on this measure, the particles in this region are less suited for single particle collection than those at the upper end of region A, as attraction is more likely.

Finally, for region C, attraction does not occur. The secondary force is always repulsive. As such, the particles are always predicted to move to the nearest node. This region, when it exists, is ideal for single particle trapping.

4.4 Cell patterning

We have used a study of solid particles to describe the different types of behaviour that can be expected as the particle size is increased within a 1D wave. In doing so we have identified regions of size, bounded by resonant modes, within which different types of outcomes can be expected. A significant application of trapping one object per well is in the use of ultrasound to pattern individual cells, hence one cell per well (OCPW).[9] As such, with the initial characterisation complete for well-defined solid materials, we now turn to examining cells. The first challenge this poses is in identifying the suitable cell mechanical properties as they are not well reported in the literature.

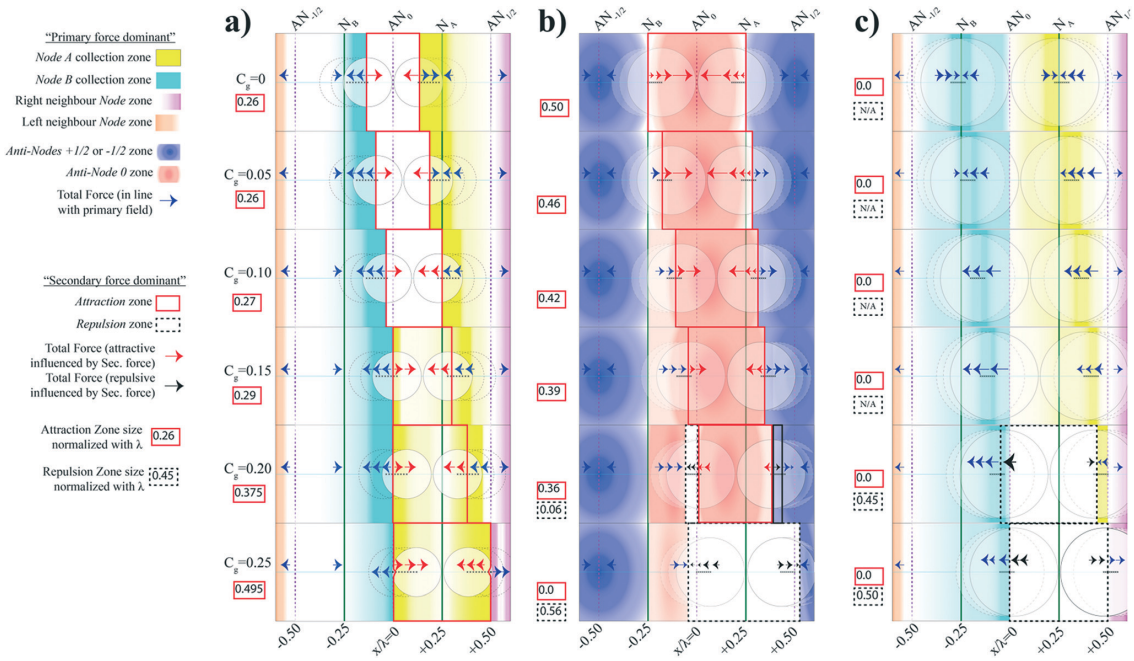

Fig. 8 Patterning map of the PMMA particles in a 1D acoustic field showing the attraction or repulsion zones along with the primary force dominant zones for three representative sizes, (a) d = 0.25λ, (b) d = 0.35λ and (c) d = 0.45λ. Values in the red (attraction) or black dotted (repulsion) boxes indicate the normalised size of each band.

4.4.1 Cell mechanical properties. The term cell refers to a diverse range of biological units that vary vastly in shape, composition, construction and function. Human cells as a subset of eukaryotes are made of nuclei, cytoplasm, cytoskeleton and membrane that make modelling of the cell as a classic mechanical system a very complicated task. Viscoelastic models of cells are generally used to predict or validate phenotyping of its physical characteristics.[55–58]

To understand blood cells' behaviour in blood vessels, arteries and hypertension, red blood cells are being studied and their biomechanical properties are of interest. The focus has been on the mechanical properties of the cell membrane which are themselves highly dependent on the load and speed of sample loading.[59–61] Ultrasound waves can provide an average reading of the cell properties as a single unit by measuring its contrast factor or acoustic impedance.[54,62]

In this study, for simplicity, the cell will be modelled as uniphase isotropic elastic solid spheres rather than a multilayered viscoelastic solid–liquid system. As this assumption is based on sample cells acoustic impedance,[54] it is valid and justifiable for the physical effects being studied. Suitable values are available for both red blood cells (erythrocytes) and white blood cells (leukocytes). Although WBCs comprise a wider variety of types they were selected due to their spherical shape. Table 2 shows WBCs' properties. The Poisson ratio of WBCs has been assumed to be 0.499 (instead of 0.5 to avoid mathematical singularity) in several studies on mechanical modelling of cells.[63–65] Measuring acoustic impedance returns in the average speed of sound for the whole cell structure, $Z_c = \rho_c c_c$,[66] taking the density as given in Table 2.[53] With this ν, all elastic moduli can be calculated. The resulting bulk modulus (2.66 GPa, close to the bulk moduli of water or blood) and Young's modulus are in a reasonable range, and moreover are in line with the values cited in some of the literature.[58,67,68]

4.4.2 Acoustic force on cells and the resulting patterning. As Young's modulus of cells is less than the previously examined polymers, it might be expected that an individual white blood cell's force–size curve would be similar to those of PMMA and PS but with a leftward shift, accounting for a lower stiffness, thus, yielding lower natural frequencies. However, the natural frequencies are also affected by the Poisson ratio in a non-linear manner. Upon calculation of the force curve, shown in Fig. 9, the ARF on a single cell (with properties from Table 2) actually is more closely aligned to the case of silica than the less stiff PMMA or PS. Indeed, for sizes smaller than half a wavelength ($\lambda/2$), the whole range is in region A (positive ARF), so the primary force tends to push the particles to the nearest node.

As performed previously, a study was completed using pairs of cells for size/wavelength ratios of 0.033, 0.10, 0.20, 0.25, 0.35 and 0.45 (Fig. 10). For all these sizes, the primary force tends to push the particles to the corresponding node. Similar to PMMA region A, the secondary force acts to attract two cells positioned on the opposite sides of an antinode. However, in contrast to PMMA, this secondary force is not strong enough to prevail over primary forces (with the exception of size 0.03 only at gap 0.01) even for larger sizes/λ ratios. The modelled cell material allows acoustic waves to transmit through with less scattering, consequently reducing secondary forces.

Herein, a map (Fig. 11) has been produced showing the forcing outcomes for two cells with different gaps between them for a range of locations of the centre of the gap. It too shows that the WBCs follow the primary force field at all positions. Secondary forces always act in the 'attraction' direction but if cells are on the opposite sides of the antinode, the secondary forces are too weak to bring them together. In this case, each cell will go to its nearest node (cell A to node A and cell B to node B). However, if both cells are initially located on the same side of the antinode, they will both be moved towards the same node (node A in this case). This behaviour appears in the force map as an attraction zone, as the end result is that the cells will migrate to the same location, nonetheless, due to the primary force.

With the dominance of the primary force field, the effectiveness of the single cell patterning is dependent on the probabilities of the initial random distribution. The chance of single cells per well is equal to the chance that the cells initially are located on either side of an antinode. For two

Table 2 White blood cell (WBC) mechanical properties

Parameter	Symbol	Value	Unit
Physical properties:			
Density[53]	ρ_c	1070	kg m^{-3}
Acoustic impedance[54]	Z_c	1.69	MPa m s^{-1}
Speed of sound[a]	c_c	1579.5	m s^{-1}
Calculated mechanical properties:			
Poisson ratio	ν_c	0.499	—
Young's modulus[b]	E_c	16	MPa
Bulk modulus[b]	K_c	2.66	GPa
Rigidity modulus[b]	G_c	5.33	MPa

[a] Calculated as $c_c = Z_c/\rho_c$. [b] Calculated as $E_c = \rho_c c_c^2 \frac{(1-\nu_c)}{(1+\nu_c)(1-2\nu_c)}$, $K_c = \frac{E_c}{3(1-2\nu_c)}$ and $G_c = \frac{E_c}{3(1-2\nu_c)}$, respectively, from ref. 70.

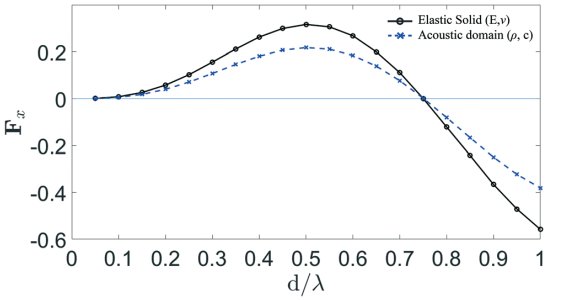

Fig. 9 Acoustic radiation force (in nN) on a white blood cell which was modelled as an elastic solid with E_c and ν_c (black line) *versus* normalised sizes. Here, the results for a cell modelled with an acoustic domain with ρ_c and c_c (dashed blue line) are also shown for comparison which justifies the elastic solid assumption.

identical cells with a diameter of d the probability of being randomly in one half or the opposite halves of a wavelength can be derived as follows:

$$P^*(\mathrm{H}) = \frac{2(0.5-\delta)^2}{(1-\delta)^2} \quad (10a)$$

$$P^*(\mathrm{O}) = \frac{0.5-\delta^2}{(1-\delta)^2} \quad (10b)$$

where, $P^*(\mathrm{H})$ and $P^*(\mathrm{O})$ are the probability of two particles randomly located at same half or opposite halves of the wavelength, respectively, as a function of normalised size, $\delta = d/\lambda$. The plot for different sizes from 0.05 to 0.5 is shown in Fig. 12. This figure shows that for sizes greater than 0.35 the chance of two spherical and identical cells to be in the same half of a wavelength (in one side of an antinode) is less than 10% and this approaches zero with increasing size. On the other hand, the chance of these two cells being randomly positioned on the opposite halves of a wavelength is more than 90% and higher for those of bigger sizes. Contrary to PMMA or PS where we had a very narrow range of sizes that made patterning possible (although guaranteed) for cells we have a much wider range of sizes that make single cell patterning possible. This can explain the findings of Collins *et al.* that cells were easier to manipulate as compared to synthetic particles; a wider range of sizes could be patterned in a single cell per node.[9]

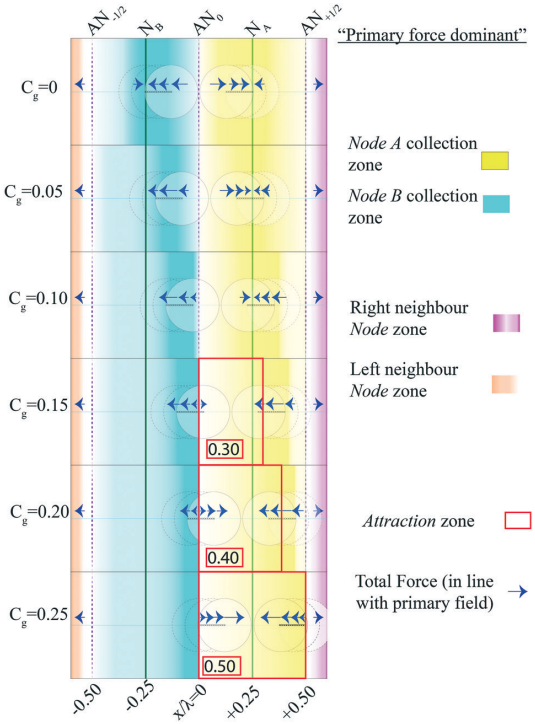

Fig. 11 Patterning map of the cell, depicted here for size d 0.25λ as the representative of the whole range, shows that cells always follow the primary force field. The attraction occurs only if both cells are in the same side of the antinode, mainly due to the primary force. However, the secondary force also contributes toward attraction in such cases.

5 Conclusions

This analysis of the forces generated on large particles in an axisymmetric plane wave has identified regions of behaviour bounded by the resonant frequencies of the particles. Before the first resonant mode, the primary forces collect the particles at pressure nodes, and the secondary forces are attractive, however, the weakness of the latter allows a good probability of single particle patterning. In the case of the white blood cells studied, this weakness is further emphasised by

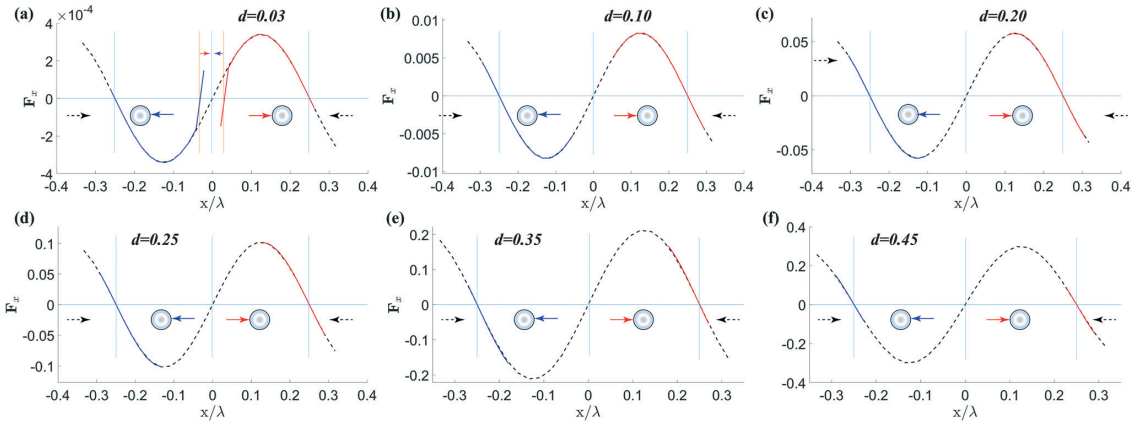

Fig. 10 Force (in nN) *vs.* position for different sizes of modelled white blood cells: black dashed lines show primary forces on single cells along their positions sweeping from the node to the opposite node for different sizes, (a) d = 0.03λ, (b) d = 0.10λ, (c) d = 0.20λ, (d) d = 0.25λ, (e) d = 0.33λ and (f) d = 0.45λ. Red and blue solid lines show the total force on particles A (top/right side) and B (down/left side), respectively, as their gap increases.

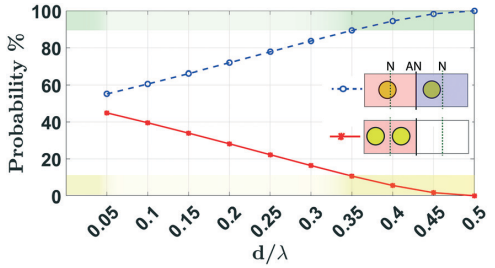

Fig. 12 The probability distribution of identical cells within a wavelength. For larger sizes, the probability that both cells are in one half wavelength (consequently in one node attraction zone) becomes smaller. At the same time, the possibility of these two cells to be located at opposite sides is closer to 100%.

their very weak scattering nature making them excellent candidates for patterning. Above the first resonant mode, the primary forces act to collect particles at the pressure antinodes. Again this patterning is opposed by the attractive secondary forces, though in this case, the strength of the latter is much more significant. Finally, the next region of behaviour again shows the primary forces acting towards the pressure nodes, but in this case, the secondary forces are repulsive, thus beneficial for individual patterning. Clearly, the behaviour in the regimes is strongly varied, and by establishing this framework a more robust understanding of the potential of single particle patterning using ultrasonic forces is offered.

Conflicts of interest

There are no conflicts to declare.

Acknowledgements

The authors gratefully acknowledge the support of the Australian Research Council by way of grant no. DP160101263 which has made this work possible.

References

1 H. Yun, K. Kim and W. G. Lee, *Biofabrication*, 2013, **5**, 022001.
2 X. Mu, W. Zheng, J. Sun, W. Zhang and X. Jiang, *Small*, 2013, **9**, 9–21.
3 J. R. Rettig and A. Folch, *Anal. Chem.*, 2005, **77**, 5628–5634.
4 S. Yamamura, H. Kishi, Y. Tokimitsu, S. Kondo, R. Honda, S. R. Rao, M. Omori, E. Tamiya and A. Muraguchi, *Anal. Chem.*, 2005, **77**, 8050–8056.
5 J. Fink, M. Thery, A. Azioune, R. Dupont, F. Chatelain, M. Bornens and M. Piel, *Lab Chip*, 2007, **7**, 672–680.
6 P. Y. Chiou, A. T. Ohta and M. C. Wu, *Nature*, 2005, **436**, 370–372.
7 P. Tseng, J. W. Judy and D. Di Carlo, *Nat. Methods*, 2012, **9**, 1113–1119.
8 N. Mittal, A. Rosenthal and J. Voldman, *Lab Chip*, 2007, **7**, 1146–1153.
9 D. J. Collins, B. Morahan, J. Garcia-Bustos, C. Doerig, M. Plebanski and A. Neild, *Nat. Commun.*, 2015, **6**, 8686.
10 D. Bazou, R. Kearney, F. Mansergh, C. Bourdon, J. Farrar and M. Wride, *Ultrasound Med. Biol.*, 2011, **37**, 321–330.
11 O. Manneberg, B. Vanherberghen, B. Onfelt and M. Wiklund, *Lab Chip*, 2009, **9**, 833–837.
12 M. Gedge and M. Hill, *Lab Chip*, 2012, **12**, 2998–3007.
13 J. Hultström, O. Manneberg, K. Dopf, H. Hertz, H. Brismar and M. Wiklund, *Ultrasound Med. Biol.*, 2007, **33**, 145–151.
14 X. Ding, P. Li, S.-C. S. Lin, Z. S. Stratton, N. Nama, F. Guo, D. Slotcavage, X. Mao, J. Shi, F. Costanzo and T. J. Huang, *Lab Chip*, 2013, **13**, 3626–3649.
15 L. Yeo and J. Friend, *Annu. Rev. Fluid Mech.*, 2014, **46**, 379–406.
16 K. Yosioka and Y. Kawasima, *Acustica*, 1955, **5**, 167–173.
17 M. Wiklund, S. Nilsson and H. M. Hertz, *J. Appl. Phys.*, 2001, **90**, 421–426.
18 U. Demirci and G. Montesano, *Lab Chip*, 2007, **7**, 1139–1145.
19 D. J. Collins, A. Neild, A. deMello, A.-Q. Liu and Y. Ai, *Lab Chip*, 2015, **15**, 3439–3459.
20 A. Neild, S. Oberti, G. Radziwill and J. Dual, *Biotechnol. Bioeng.*, 2007, **97**, 1335–1339.
21 J. Shi, D. Ahmed, X. Mao, S.-C. S. Lin, A. Lawit and T. J. Huang, *Lab Chip*, 2009, **9**, 2890–2895.
22 X. Ding, J. Shi, S.-C. S. Lin, S. Yazdi, B. Kiraly and T. J. Huang, *Lab Chip*, 2012, **12**, 2491–2497.
23 X. Ding, S.-C. S. Lin, B. Kiraly, H. Yue, S. Li, I.-K. Chiang, J. Shi, S. J. Benkovic and T. J. Huang, *Proc. Natl. Acad. Sci. U. S. A.*, 2012, **109**, 11105–11109.
24 F. Guo, Z. Mao, Y. Chen, Z. Xie, J. P. Lata, P. Li, L. Ren, J. Liu, J. Yang, M. Dao, S. Suresh and T. J. Huang, *Proc. Natl. Acad. Sci. U. S. A.*, 2016, **113**, 1522–1527.
25 H. Mulvana, S. Cochran and M. Hill, *Adv. Drug Delivery Rev.*, 2013, **65**, 1600–1610.
26 M. Hill, R. J. Townsend and N. R. Harris, *Ultrasonics*, 2008, **48**, 521–528.
27 J. Shi, S. Yazdi, S.-C. Steven Lin, X. Ding, I.-K. Chiang, K. Sharp and T. J. Huang, *Lab Chip*, 2011, **11**, 2319–2324.
28 T. Franke, A. R. Abate, D. A. Weitz and A. Wixforth, *Lab Chip*, 2009, **9**, 2625–2627.
29 G. Destgeer, K. Lee, J. Jung, A. Alazzam and H. Sung, *Lab Chip*, 2013, **13**, 4210–4216.
30 J. Shi, H. Huang, Z. Stratton, Y. Huang and T. Huang, *Lab Chip*, 2009, **9**, 3354–3359.
31 D. Collins, T. Alan and A. Neild, *Lab Chip*, 2014, **14**, 1595–1603.
32 T. Laurell, F. Petersson and A. Nilsson, *Chem. Soc. Rev.*, 2007, **36**, 492–506.
33 R. Walker, I. Gralinski, K. K. Lay, T. Alan and A. Neild, *Appl. Phys. Lett.*, 2012, **101**, 163504.
34 L. Gor'kov, *Sov. Phys. Dokl.*, 1962, 773.
35 M. Settnes and H. Bruus, *Phys. Rev. E: Stat., Nonlinear, Soft Matter Phys.*, 2012, **85**, 016327.
36 A. A. Doinikov, *J. Fluid Mech.*, 1994, **267**, 1–22.
37 F. Mitri, *Ultrasonics*, 2005, **43**, 681–691.
38 T. Hasegawa, *J. Acoust. Soc. Am.*, 1979, **65**, 32–40.

39 P. B. Muller, R. Barnkob, M. J. H. Jensen and H. Bruus, *Lab Chip*, 2012, **12**, 4617–4627.
40 V. F. K. Bjerknes, *Fields of Force*, Columbia University Press, New York, 1906.
41 A. A. Doinikov and S. T. Zavtrak, *Phys. Fluids*, 1995, **7**, 1923–1930.
42 A. Doinikov and S. Zavtrak, *Ultrasonics*, 1996, **34**, 807–815.
43 S. Sepehrirahnama, K.-M. Lim and F. S. Chau, *J. Acoust. Soc. Am.*, 2015, **137**, 2614–2622.
44 H. Bruus, *Lab Chip*, 2012, **12**, 20–28.
45 H. Bruus, *Theoretical microfluidics*, 2008.
46 P. Glynne-Jones, P. P. Mishra, R. J. Boltryk and M. Hill, *J. Acoust. Soc. Am.*, 2013, **133**, 1885–1893.
47 W. M. Haynes, *CRC handbook of chemistry and physics*, CRC press, 2014.
48 P. Mott, J. Dorgan and C. Roland, *J. Sound Vib.*, 2008, **312**, 572–575.
49 R. Kono, *J. Phys. Soc. Jpn.*, 1960, **15**, 718–725.
50 T. Hasegawa and K. Yosioka, *J. Acoust. Soc. Am.*, 1969, **46**, 1139–1143.
51 P. B. Muller, R. Barnkob, M. J. H. Jensen and H. Bruus, *Lab Chip*, 2012, **12**, 4617–4627.
52 E. Hanukah, 2013, arXiv preprint arXiv:1311.0741.
53 A. Zipursky, E. Bow, R. Seshadri and E. Brown, *Blood*, 1976, **48**, 361–371.
54 P. Augustsson, J. T. Karlsen, H. Su, H. Bruus and J. Voldman, *Nat. Commun.*, 2016, **7**, 11556.
55 C. Dong and R. Skalak, *J. Theor. Biol.*, 1992, **158**, 173–193.
56 C. Lim, E. Zhou and S. Quek, *J. Biomech.*, 2006, **39**, 195–216.
57 S. Suresh, *Acta Mater.*, 2007, **55**, 3989–4014.
58 M. Starodubtseva, *Ageing Res. Rev.*, 2011, **10**, 16–25.
59 N. Guz, M. Dokukin, V. Kalaparthi and I. Sokolov, *Biophys. J.*, 2014, **107**, 564–575.
60 M. Dao, C. Lim and S. Suresh, *J. Mech. Phys. Solids*, 2003, **51**, 2259–2280.
61 T. Omori, T. Ishikawa, D. Barthès-Biesel, A.-V. Salsac, Y. Imai and T. Yamaguchi, *Phys. Rev. E: Stat., Nonlinear, Soft Matter Phys.*, 2012, **86**, 056321.
62 R. Barnkob, P. Augustsson and C. Magnusson, *Proceedings of the 15th MicroTAS*, 2011.
63 A. Smith, K. Moxham and A. Middelberg, *Chem. Eng. Sci.*, 1998, **53**, 3913–3922.
64 Z. Zhang and X. Zhang, *Sci. China: Life Sci.*, 2011, **54**, 450–458.
65 T. Boudou, J. Ohayon, Y. Arntz, G. Finet, C. Picart and P. Tracqui, *J. Biomech.*, 2006, **39**, 1677–1685.
66 A. Lenshof, M. Evander, T. Laurell and J. Nilsson, *Lab Chip*, 2012, **12**, 684–695.
67 R. Hochmuth, N. Mohandas and P. Blackshear, *Biophys. J.*, 1973, **13**, 747–762.
68 M. Toubal, M. Asmani, E. Radziszewski and B. Nongaillard, *Phys. Med. Biol.*, 1999, **44**, 1277.
69 D. Chakraborty and J. E. Sader, *Phys. Fluids*, 2015, **27**, 052002.
70 L. D. Landau and E. M. Lifshitz, *Course of Theoretical Physics Vol 7: Theory of Elasticity*, Pergamon Press, 1959.

Electronic Supplementary Material (ESI) for Lab on a Chip.

Trapping and Patterning of Large Particles and Cells in a 1D Ultrasound Standing wave†

Ruhollah Habibi[a] Citsabehsan Devendran[a] Adrian Neild[a*]

LMS, Monash University LMS, Monash University LMS, Monash University

I. Supplementary Information (SI)

I.1. Damping and bulk viscosity effects

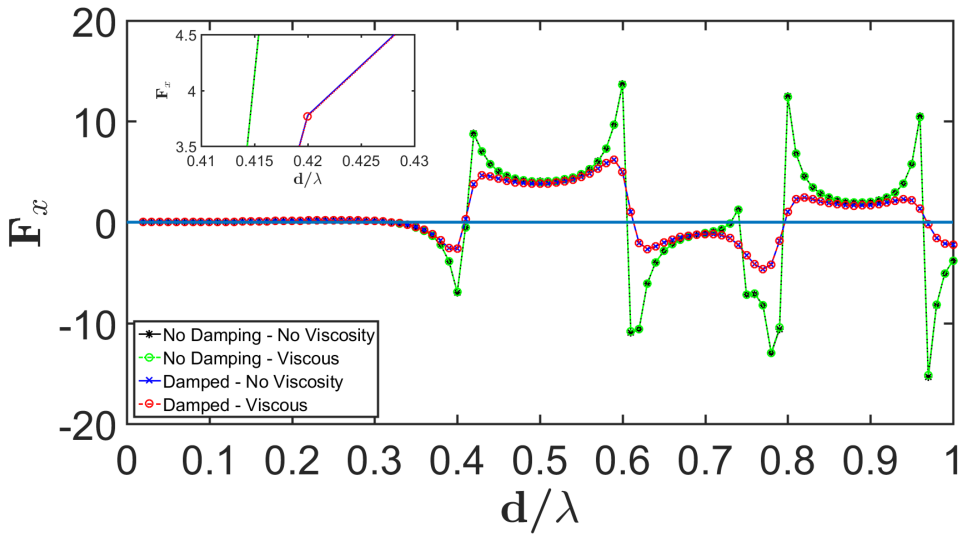

Fig. S1: *Force (in nN) versus size plot for PMMA with the consideration of the damping in the solid particle and the viscosity in the fluid bulk. Viscosity has little influence on acoustic radiation force while the damping of solid (modelled with isotropic loss factor=0.05) reduces the force magnitude at resonating sizes (frequencies). Though, damping does not have considerable effect on AFR at other sizes.*

To consider the effect of the solid damping and fluid viscosity, the axisymmetric model of the single particle under a 1D acoustic wave was simulated considering the viscosity in the fluid bulk

*Corresponding author: Laboratory for Micro Systems, Department of Mechanical and Aerospace Engineering, Monash University, Clayton, Victoria 3800, Australia.; E-mail: adrian.neild@monash.edu

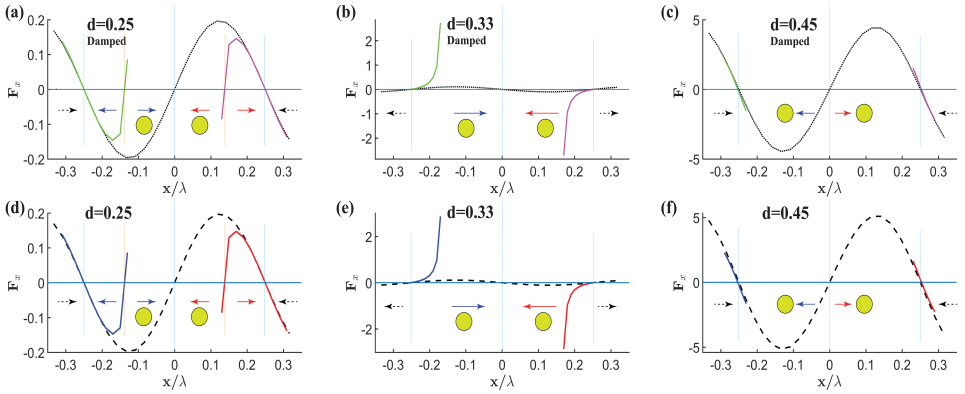

Fig. S2: *Force (in nN) vs Position for different sizes: black dashed/dotted line shows Primary forces on single particles along their positions sweeping from a node to other opposite node for previously investigated representative sizes while solid damping and fluid viscosity were included (a) $d = 0.25\lambda$ (b) $d = 0.35\lambda$ (c)$d = 0.45\lambda$. Magenta and green solid lines show Total force on particles A (top/right side) and B (down/left side) respectively as their gap increases. Figures (d), (e) and (f) reproduced from the main article's Fig. 2(d)-(f) for the same sizes without damping. Damping decreased the primary and total forces slightly but does not change the interparticle attraction / repulsion behaviour*

and loss factor for the solid. To investigate the effect of these two parameters, acoustic radiation force (ARF) on a PMMA spherical particle in a fluid (water) domain were computed while other parameters of Table 2 of the main article remained unchanged.

Fig. S1 which is comparable with Fig. 2a in the main article shows that viscosity has almost no distinguishable effect on the AFR. It should be noted that, as only large size particles are considered ($d > 0.10\lambda$), we do not consider streaming effects and the viscosity is only applied to the bulk of the fluid and the viscosity were only applied on the fluid bulk properties.

On the other hand, it is observed that damping decreases the force magnitude considerably at resonating sizes. However, its effect becomes negligible at the non-resonating size, i.e. the majority of sizes. Although, the solid damping absorbs a portion of energy from the incoming wave, thus flattens the peaks and troughs in the ARF curve, it does not change the force shifting pattern or its turning points.

Inter-particle behaviour will not change significantly and the patterning regime is still valid. Nevertheless, it is expected that the secondary force which is under influence of resonance, will reduce as well. The reduction of secondary force and consequently the total force is negligible at non-resonating sizes. This said the regions and the general trend of inter-particle secondary force at different sizes remain unchanged as it can be observed in Fig. S2.

I.2. Implementation of damping and viscosity in the COMSOL model

In the Pressure Acoustics module of COMSOL Multiphysics ver. 5.1, the fluid is modelled as viscous by considering its dynamic viscosity μ, and bulk viscosity μ_B. This will incorporate the

attenuation due to bulk viscous losses and the speed of sound is altered accordingly as denoted here in Eqn. 1:[1]

$$c_{vis} = c_0 \left(1 + i\omega \frac{\left(\frac{4\mu}{3} + \mu_B \right)}{\rho c_0^2} \right)^{0.5} \tag{1}$$

where c_{vis} indicates the altered speed of sound, c_0 fluid's speed of sound, $i = \sqrt{-1}$, ω angular frequency and ρ_0 as the density of the fluid. The damping also can be added to the solid particle's properties by implementing isotropic loss factor into its elastic moduli matrix:[1]

$$\boldsymbol{C_D} \equiv (1 + i\eta_s)\, \boldsymbol{C} \tag{2}$$

that $\boldsymbol{C_D}$ denotes 'damped' moduli matrix, η_s isotropic loss factor and $\boldsymbol{C}$ elastic moduli matrix. The isotropic loss factor, η_s of PMMA considered 0.05 which is valid for temperatures (here 25 °C) below its glass transition temperature.[2]

References

[1] C. Multiphysics, *COMSOL, Burlington, MA*.

[2] M. Dixit, S. Gupta, V. Mathur, K. S. Rathore, K. Sharma and N. Saxena, *Chalcogenide Letters*, 2009, **6**, year.

Chapter 4

Sound Wave Activated Nano-sieve (SWANS) for Trapping and Enriching of Nanoparticles

4.1 Overview

Nanoparticle trapping and enrichment is an essential step in several applications such as, drug delivery, viral studies, diagnosis and nanowire synthesis and alignment. In these applications suspended nanoparticles should either be altered or isolated and enriched. For example, exosomes with a size range between 50 - 200 nm are found at low concentration in human blood plasma, urine and milk and therefore require a rapid, clean and damage-free enrichment and collection method. This chapter proposes and establishes the foundation of such a non-contact, label-free, on-demand 'trap and release' method.

The work in this chapter is aimed at utilizing one of the key findings from Chapter 3, that identified three regions in the frequency range that equivalent to $d/\lambda < 1/2$. In the case of PMMA spherical particles, in the first region ($0 < d/\lambda < 0.33$), Region A, the primary acoustic radiation force always pushes the particles toward the minimum pressure nodes while the secondary Bjerknes force is only attractive in very close proximity. Further, in the second region ($0.33 < d/\lambda < 0.42$), Region B, the primary force drive them to antinodes and the secondary force is almost attractive in all gaps and positions (within the range of $\lambda/4$ with respect to the wave axis). Lastly, the next region ($0.42 < d/\lambda < 0.5$), Region C, where again has positive primary forces, can pattern the particles individually at single pressure nodes with the help of all-negative, i.e. repulsive, Bjerknes force.

As previously discussed, in the region B, a polymeric solid particle generates significantly higher amplitudes of attractive forces. The findings on region B are further investigated to devise a system for the trapping of nanoparticles. This sharp increase of the 'attractive' secondary Bjerknes forces occurs around a resonance frequency for a single elastic particle.

Within that frequency range, although the larger bead can attract and trap a nearby smaller particle, due to the nature of the resonance, the behaviour of single particles freely suspended in a fluid is not always predictable or completely controllable. In a microchannel, micropillars can therefore be used to hold the larger microbeads and form a packed bed. With the addition of SAW, higher frequencies can be reached and more energy can be transferred to the fluid domain. Simulations of a single microparticle and a single nanoparticle shows that there are two peaks of attractive forces in Regions B and C where the microparticle's natural frequencies appear. The packed bed of 10 μm polystyrene particles was excited between 60 - 90 MHz, corresponding to Regions B and C of those beads, with two opposing chirped IDTs so that a standing wave field is formed in the centre of the channel. The channel widths in this study were selected as 50 and 94 microns, relatively narrower that the distance between opposing IDTs to minimise the attenuation. A sample of fluorescent 500 nm polystyrene particles were then continuously pumped through the packed bed. The results reveal two peak frequencies at around 70±2 and 77±2 MHz, similar to the predicted trend where a high capturing efficiency, as high as 97%, was achieved. The resonance of the elastic particles is a function of their diameter and material properties,and as such, the performance of the system is not limited to the resonance of the fluid chamber, as is the case in a BAW system. That makes this system an ideal candidate for upscaling.

The performance of the packed bed, as a function of beads' natural frequencies, depends on their size and mechanical properties. The uniformity in beads size and compressibility makes the system more predictable and efficient as all particles will participate in collection when a resonance frequency is excited. This chapter establishes the foundation for such a non-contact, label-free, on-demand trap and release method for nanoparticles as small as 100 nm.

4.2 Publication

The following publication was reproduced from [2] with kind permission from the Royal Society of Chemistry.

Lab on a Chip

PAPER

View Article Online
View Journal | View Issue

Cite this: *Lab Chip*, 2019, **19**, 3032

Sound wave activated nano-sieve (SWANS) for enrichment of nanoparticles†

Ruhollah Habibi and Adrian Neild *

Received 16th April 2019,
Accepted 31st July 2019

DOI: 10.1039/c9lc00369j

rsc.li/loc

Acoustic actuation is widely used in microfluidic systems as a method of controlling the behaviour of suspended matter. When acoustic waves impinge on particles, a radiation force is exerted which can cause migration over multiple acoustic time periods; in addition the scattering of the wave by the particle will affect the behaviour of nearby particles. This interparticle effect, or Bjerknes force, tends to attract particles together. Here, instead of manipulating a dilute sample of particles, we examine the acoustic excitation of a packed bed. We fill a microfluidic channel with microparticles, such that they form a closely packed structure and then excite them at the particle's resonant frequency. In this scenario, each particle acts as a source of scattered waves and we show that these waves are highly effective at attracting nanoparticles onto the surface of the microparticles, and nanoparticle collection characterises the performance of this mechanically activated packed bed.

1 Introduction

Nanoscale particles and biological structures are ubiquitous, and include DNA in the cell lysate, viruses and bacteria; in addition, nanoparticles are commonly synthesized[1–4] for applications such as nanomedicine and nanoscale drug delivery.[5] Handling of matter on this scale enables a range of applications to be addressed, such as viral[6–8] or nanoparticle induced fusion of cells,[9,10] detection and diagnostics,[11–17] and alignment of nanowires.[18] In addition, due to recent developments in regenerative medicine, there has been a surge in interest in the capture of extracellular vesicles (EVs). Formed inside cells and secreted through the cell membrane, EVs contain genetic information of the parent cell[19] and are believed to be responsible for cell–cell communication, antigen-presenting cells, coagulation and transfer of proteins; as such they are considered as a valuable precursor for regenerative medicines.[20–22]

EVs refer to a broad range of vesicles including microvesicles (MVs), apoptotic bodies and exosomes.[23,24] They have a variety of sizes ranging from 30 to 1000 nm. To use them as biomarkers, they need to be separated and segregated into their particular type;[25] similarly, for drug synthesis a need for a very quick and clean method of collection and enrichment has been identified.[20] Conventional methods for EV collection include ultra-centrifugation,[26,27] ultra-filtration,[28] immunocapture,[29,30] chromatography[31] and precipitation.[32] Of these, the first two are more widely used but are time consuming, laborious and generally damaging to the bioparticles. Meanwhile, the latter examples are only applicable to small sample volumes and the chemical bonds formed can cause contamination of the captured matter.[22,25,33–35] As an alternative, emerging microfluidic-based methods show significant promise.[36–38]

Whilst microfluidics has widely been used for the separation, trapping and enrichment of microparticles,[39] there is also a growing body of literature on nanoparticle handling. To achieve this, several mechanisms have been exploited, including passive hydrodynamic methods such as micropillars,[40,41] filtration,[42] and inertial-based techniques.[43–45] In addition to these passive methods, a range of active systems have been developed. Here energy is input into the system to activate a collection mechanism; this allows a level of control and adaption of system parameters post manufacture which is unavailable in passive architectures. Various forcing mechanisms have been utilised, including electro and dielectrophoresis,[42,46–49] magentophoresis,[16,50–52] acoustophoresis[53–56] and optical tweezers.[57,58] Of these active methods, acoustofluidics has the advantage of being contactless, label-free and biocompatible.[59,60]

Acoustofluidics, the use of acoustic energy as an actuation source in microfluidic chips, offers three main forcing mechanisms. Acoustic radiation forces (ARFs) act on suspended particles causing migration to certain, ultrasonic field dependent locations in the fluid volume. The ARF is frequently used to control the position of microparticles[61–64] and

Laboratory for Micro Systems, Department of Mechanical and Aerospace Engineering, Monash University, Clayton, Victoria 3800, Australia.
E-mail: adrian.neild@monash.edu

† Electronic supplementary information (ESI) available. See DOI: 10.1039/c9lc00369j

View Article Online
Lab on a Chip Paper

cells.[65–67] However, there are only a few papers on the use of the ARF on nanoparticles;[56,68–70] this is due to scaling laws, meaning as the particle becomes smaller, the acoustic streaming induced drag forces become more dominant,[71–73] unless the streaming can be suppressed.[74] Acoustic streaming a bulk fluid flow, which results from the propagation of ultrasound, typically induces swirling flows which disrupt the patterns formed by the ARF. However, these flows can also be used to capture cells[75–77] and nanoparticles;[55,78,79] here the suspended matter becomes trapped within a vortex within the limitation of a low capacity limit and flow rate. The third focusing method arises due to particle–particle interaction. The ultrasonic wave scattered from one particle interacts with other nearby objects, and induces a Bjerknes force, which depending on the nature of the particles and their orientation can be attractive or repulsive. In a very elegant approach, Laurell's research group at Lund University held a cluster of microparticles using the ARF generated by a sound field; the scattered waves engendered Bjerknes forces to act on nanoparticles as they passed near this cluster, such that they were collected on the microparticles.[80–83] One of the challenges in acoustofluidics is to create a sufficiently large force; to tackle this, a resonance is usually exploited; by using bulk wave excitation to create a resonance in a fluid channel, the microparticles could be held at the centre of the channel and the Bjerknes forces were sufficient to allow for highly efficient capture. This system works very well for small, diagnostically relevant sample sizes; however upscaling of this approach beyond this scale would be challenging due to the requirement of a channel resonance. In this work, we present a microfluidic system for acoustic capture of nanoparticles using a previously unexploited resonance. The advantage of this approach is that it has the potential for future upscaled processing; however, here we focus on characterising the mechanism of this resonance.

Packed beds of beads have been widely used for filtration[84,85] or chemical process reactors.[86] In addition, in microfluidics, functionalised beads in a packed bed have occasionally been used to trap certain types of proteins or bioparticles.[87–89] Here, rather than using chemical functionalisation, we use mechanical (ultrasonic) actuation. The use of surface acoustic waves (SAWs) is an actuation method which gives access to a higher range of frequencies than typically excited using bulk acoustic waves. Generated by patterned electrodes on a piezoelectric substrate (interdigital transducers or IDTs), they have been used in microfluidics for patterning, sorting, sieving and trapping; however, most systems only migrate the particles instead of holding them in position.[59,69,90,91]

Notably, high frequency operation has been used for single cell patterning in which the acoustic wavelength is in the order of the size of a cell.[60] When modelling the ARF and Bjerknes forces generated in this type of system, we previously showed a very large increase in the Bjerknes force at resonance frequencies of the particles which we were trying to manipulate, such that clustering dominated over patterning.[92] Hence, here, we use the high frequency opportunities offered by SAWs to deliberately excite a packed bed of microparticles, such that each resonates. When nanoparticles are passed through the pores left between the larger particles, they get attracted and collected due to the large Bjerknes forces that occur. As such, the resonance is related to the particle size, and so is decoupled from the channel dimensions (Fig. 1). Upon switching off the SAW actuation, the enriched nanoparticles are released from the bed, avoiding issues with clogging which beset membrane filtration methods.

2 Operating principles

In most acoustically actuated microfluidic systems, the particulate matter is highly dilute and the wavelength of sound is far in excess of the particle size. In this way, phenomena such as particle migration to the pressure nodes of a standing sound wave can be observed, and used for tasks such as particle sorting and manipulation. Recently, there have been some studies which utilise higher frequencies of operation, such that the wavelength is decreased and approaches the size of the particles. But, here too, the sample is dilute as patterning effects were being sought.[60] In contrast, in this work we will use a packed bed, in which movement of the microparticles is undesirable, and seek to resonate the particles to have maximum interparticle effects. To examine if this is possible, we will first examine numerically if the interparticle forces between the microparticles are such that the packed bed will remain intact upon excitation, and secondly show the relationship between the frequency and the magnitude of the forces being exerted on nanoparticles as they pass near a vibrating microparticle.

Previously, the authors examined forces between microparticles as a function of frequency, for the purpose of finding operating conditions under which the particles will be held separate from each other in a sound field.[92] A similar work has studied the effects of different particle sizes relative to the wavelength, in other words the frequency, on the acoustic radiation force and identified different regions as well.[93] Such repulsive interparticle effects could be highly detrimental to a packed bed; however this earlier study provides the framework required to establish at what frequencies a packed bed can be expected to be stable. Namely, in that work, frequency regions were defined based on the forces which are known to act on a single particle exposed to a standing pressure wave when located in the middle of a pressure node and antinode, as shown in Fig. 2a. It can be seen that for the polystyrene (PS) particle considered, if the particle size is smaller than one third of the wavelength the acoustic radiation force is positive, meaning it will migrate to the pressure nodes (region A: $d < 0.31\lambda$) where d is the diameter of the spherical particle and λ is the wavelength of a 1D standing planar wave. At larger particle sizes the acoustic radiation force is negative; hence the particle is moved to the nearest antinode (region B: $0.31\lambda < d < 0.45\lambda$); the first particle resonance occurs in

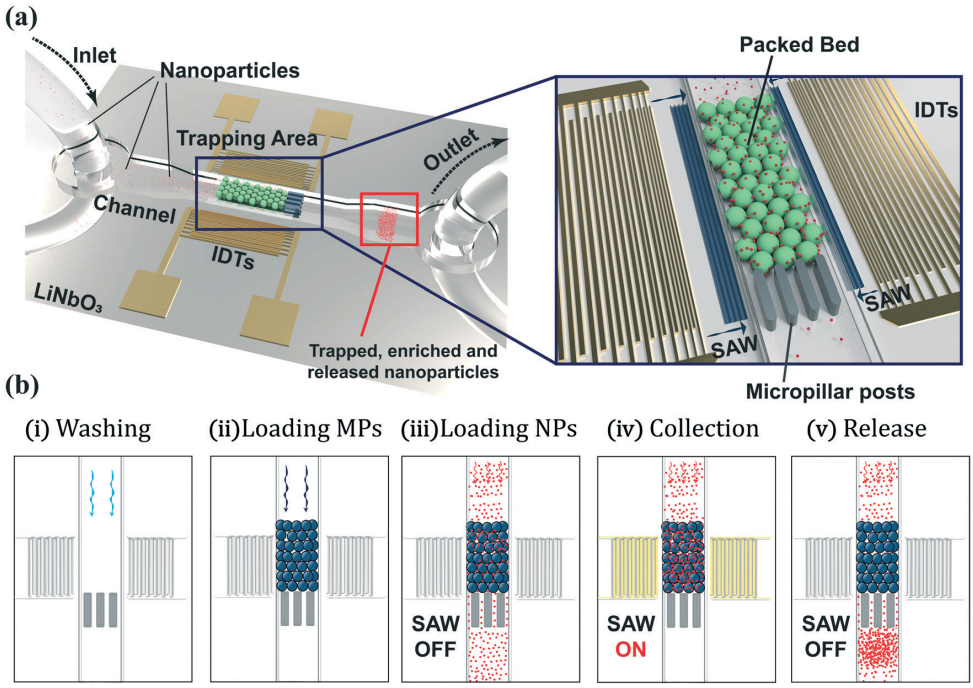

Fig. 1 (a) Schematic of the microfluidic device for trapping and enriching nanoparticles using resonance of a passively-trapped packed bed of 10 μm polystyrene beads excited by surface acoustic waves (SAWs). The enlarged view of the trapping area shows two opposing IDTs used to generate the standing SAW and the micropillars that trapped the microbeads. (b) Schematic illustration of the system that shows the sequence of the loading of microparticles (MPs) and then nanoparticles (NPs). Upon activating the SAW (here IDTs are highlighted in yellow), nanoparticles can be collected on demand and the high concentration sample can be released by switching off the SAW. Stages are further explained in the ESI.†

this region of operation, as seen by the spike in force magnitude. This alternation of the sign of the force is also used to define further regions (*e.g.* region C: $0.45\lambda < d < 0.67\lambda$). The boundaries between these ranges are dependent on the material properties of the spherical elastic particle, which can be difficult to determine exactly. It was shown that interparticle forces between two particles separated by small gaps (in the order of $\lambda/100$) about a pressure antinode are attractive in regions A, B and C except for a narrow band in region C. Based on this, we would expect the packed bed to be stable under most conditions. To confirm this and to investigate the force field acting around large particles, we model a small cluster in which the particles (having their sizes within the range of region B) are placed adjacent to each other, as would occur in a packed bed, and confirm that the interparticle forces are attractive, Fig. 2b.

We now examine the attraction force which exists between a vibrating microparticle and a nearby nanoparticle in an inviscid fluid. Again, we examine this with reference to the microparticle regions of operation. For a pair of 10 μm and 500 nm polystyrene spherical particles with a fixed gap of $\lambda/100$ (at each frequency), the total force on the NP is shown in Fig. 2d; in addition, the primary force acting on the nanoparticle in the opposite direction (negative sign) is also shown for comparison. The key features of this plot are firstly a dominance of the secondary force in the contribution to the total acoustic forces acting on the NP. Secondly, the first peak of this secondary attractive force is observed within region B (with a frequency close to the first resonance seen in Fig. 2a) followed by a drop (close to the regions' border), and then another peak in region C (Fig. 2c). The parameters of the numerical models can be found in Table S1.†

The Bjerknes force is inversely related to the distance between two particles, so whilst just a single separation is shown in Fig. 2c and d, the trend is more broadly applicable. In our case, using a packed bed, the maximum separation distance is constrained by the size of the "pores" between the microparticles (see Fig. S1†).

Moreover, it has been shown that when viscosity is considered, the acoustic radiation forces generated on a particle are larger than those in an inviscid fluid.[94] This effect becomes more significant for smaller particles. The "apparent" size of the particle is related to its actual size, as well as the thickness of the viscous boundary layer (δ, penetration depth). Such a study has not been performed for secondary forces on elastic particles; however, we can reasonably expect a similar effect to that shown by Sepehrirahnama *et al.*[95] for the secondary force under viscous conditions on rigid particles. It is worth noting that a 500 nm particle is considered in our

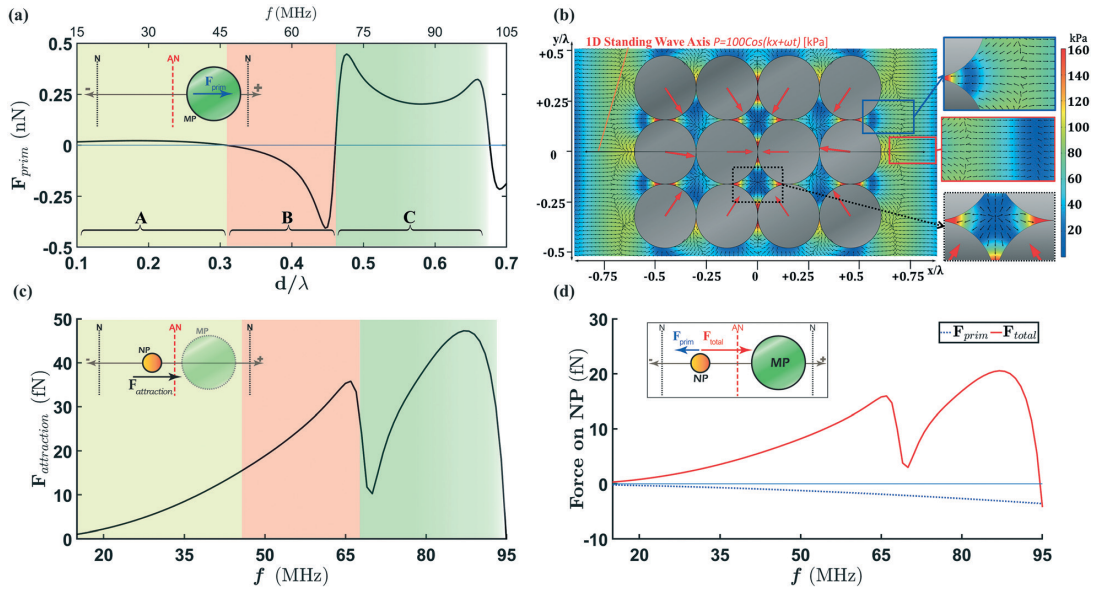

Fig. 2 Numerical results for the acoustic radiation force on micro- and nanoparticles: a) the primary acoustic radiation force on a single polystyrene (PS) particle located at a distance of $+\lambda/8$ away from the pressure antinode (indicated as AN in red and nodes as N in black in the schematic) shows distinct regions of behaviour (A, B and C). Here, a 10 μm PS particle in water is excited by a 100 kPa planar sound field. A particle resonance occurs in region B and two higher modes in C. When (b) a small cluster of microparticles (MPs) are excited in region B, it shows that (i) the forces between the microparticles are attractive, thus holding the cluster together and (ii) nanoparticles within the cluster are attracted to the microparticles, whilst those outside the cluster are pushed to the pressure nodes (by primary forces). All forces are normalised to only show the direction and not proportional to their magnitude. (c and d) The frequency regions defined by microparticle characteristics (in (a)) translate to different forcing regimes for the nanoparticles in proximity to the microparticles. Here, results are shown for a 10 μm and a 500 nm PS particle within a normalised gap of $\lambda/100$ about a pressure antinode. The NP also experiences primary forces; however these are much less significant than the force attracting them to the microparticles. Please refer to Fig. 5b of ref. 92 which explains further how the attraction force ($F_{attraction}$) which is the net Bjerknes secondary force is obtained when the primary force (F_{prim}) and the total force (F_{total}) are known.

models, and the range of viscous penetration depths over the frequencies being considered is 50 to 130 nm. As we are interested in the relative force at different frequencies, the effect is that our model will underestimate the force at lower frequencies – when the penetration depth is largest.

This theoretical study, whilst not fully modelling a mechanically actuated packed bed, shows the key underlying physics behind the operation, specifically with relation to the role of microparticle resonance. We will make use of the interparticle forces between microparticles to maintain a stable packed bed, and then choose our operating frequency based on the occurrence of a maximum force between the micro- and nanoparticles. This corresponds to conditions detailed in Table 1 as the summary of important frequencies in a system of 10 μm and 500 nm PS particles.

Table 1 Summary of frequency regions, normalised sizes of the microparticle (MP) and corresponding frequencies for a 10 μm PS particle (with its resonance frequencies highlighted in bold) based on the numerical simulation. The critical points of the attraction force on the nanoparticle (NP, 500 nm polystyrene) are also highlighted for comparison. Regions are defined based on the normalised size of the MP, so for different MP sizes, the critical frequencies can be conveniently obtained from their corresponding (d/λ)

MP normalised size, (d/λ)	Regions	Wavelength, λ (μm)	Frequency, f (MHz)	Notes	
				Attraction force on NP	Primary force on MP
0.3	B	33.33	45	—	Primary force zero, the border of regions A and B
0.45		22.22	**67.5**	*1st peak (≈65.73 MHz)	An extremum of the primary force, the first resonance
0.46		21.74	69.00	—	Primary force zero, the border of regions B and C
0.475	C	21.05	**71.26**	(Trough)	An extremum of the primary force, the second resonance
0.5		20	75	—	Half wavelength
0.55		18.18	82.5	*2nd peak	
0.63		15.87	94.52	(Zero)	

View Article Online

Paper

Lab on a Chip

3 Materials and methods

3.1 Simulation

To understand the physics behind the particles' interaction in a one-dimensional standing wave, a 10 μm and a 500 nm sphere with polystyrene materials were modelled in the COMSOL Multiphysics® 5.1 Acoustics module. The solid domain was attributed to the spheres with user-defined polystyrene materials (1050 kg m^{-3} density, 3.69 GPa Young's modulus and 0.3 Poisson ratio) and for the surrounding domain water was selected from COMSOL's database. To investigate single polystyrene microparticle frequency regions and its interparticle interaction with the 500 nm nanoparticle, we established the model in Axisymmetric 2D geometry. However, for multiple microparticle scenarios, a more time efficient 2D geometry was applied in lieu of the full 3D geometry. Further details on the simulation setup are described in the ESI.†

3.2 Fabrication

Microchannels with widths of either 50 μm or 94 μm and height of 21–22 μm were designed in AutoCAD and a silicon master mould was fabricated by positive photolithography, chromium deposition as an etching mask and DRI etching of silicon to the desired depth. Microchannel chips were produced by polydimethylsiloxane (PDMS; 1 : 10 ratio of curing agent/base) soft lithography on the Si mould.

The substrate onto which the PDMS component is bonded comes from a lithium niobate ($LiNbO_3$, LN) wafer (128° *Y*-cut). The deposition of metal electrodes on this piezoelectric material forms interdigital transducers (IDTs) capable of generating SAWs. Specifically, broadband (chirped) IDTs with 1.14 mm aperture were aligned 45 deg relative to the *x*-propagation direction and two different wavelength ranges, 14–60 μm and 20–70 μm, were used. IDT fingers and contact pads were fabricated from a 5 nm-thick Cr primer layer, 190 nm-thick Al conductive layer and 5 nm-thick Au corrosion protective layer. Another 250 nm-thick layer of SiO_2 was deposited on top of the IDT area for further protection against erosion and better bonding to PDMS. The electrodes were fabricated *via* the conventional photolithography technique followed by E-beam evaporation deposition, lift-off and finally cutting using a dicing saw. The PDMS microchannels were bonded onto the LN substrate after plasma treatment (Harrick Plasma, PDC-32G). The SAW that is generated on the surface of LN loses its energy due to attenuation when it propagates further, in particular when transmitting through the PDMS bulk material. To minimise SAW attenuation, the

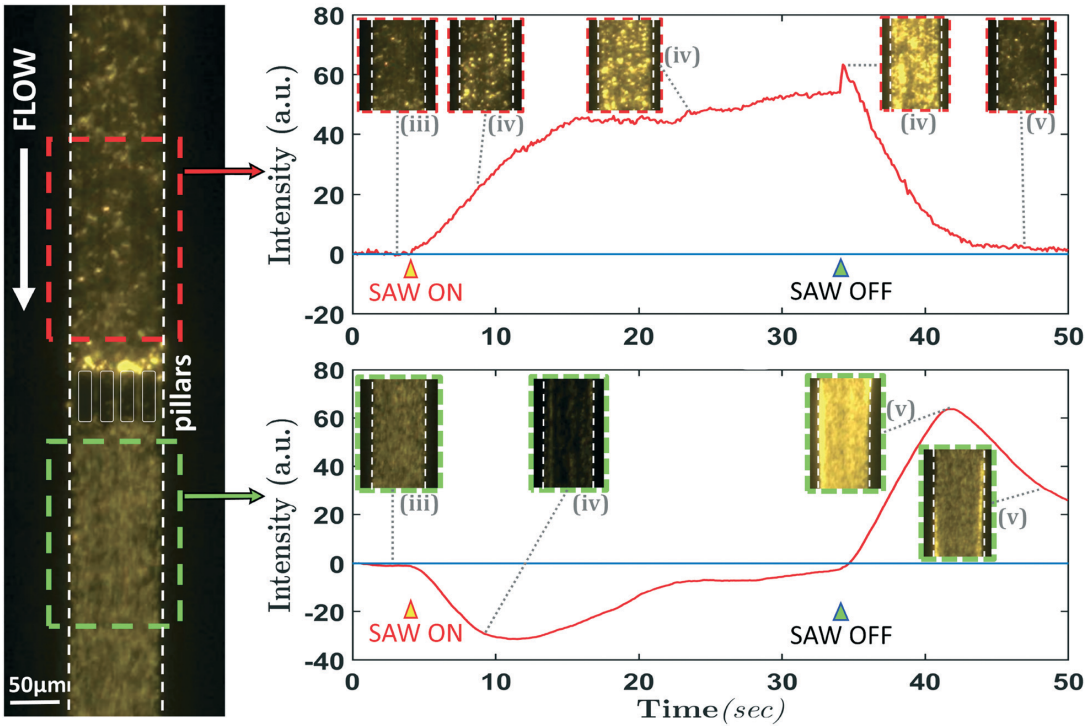

Fig. 3 The intensity change demonstrates fluorescent 500 nm NP collection (when the SAW is ON) and later the release of the enriched batch (after the SAW is switched OFF) in a 94 μm wide channel with the packed bed of non-fluorescent 10 μm MPs at the upstream. The intensity is tracked upstream and downstream of the retaining pillars (red and green dashed boxes, respectively). Excitation was at 80 MHz, 12 dBm. Captions in the plots show their side of channel at the data point time and their indices correspond to the sequence according to Fig. 2b.

View Article Online
Lab on a Chip Paper

PDMS microchannel chip has air pockets incorporated on top of IDTs with a thin 60 μm wall isolating each from the test channel. The 10 μm beads used as microparticles (MPs) for the packed bed were non-fluorescent dark red and made of polystyrene (Magsphere, USA). Three different sizes of polystyrene fluorescent nanoparticles (Magsphere, USA) were used, 500 nm in red, 190 nm in yellow-green and 100 nm in red. Solid particles were suspended in a water solution of 2% polyethylene glycol to avoid particles from attaching to channel walls. Prior to each experiment run to achieve a homogeneous suspension, the sample was shaken by a vortex mixer.

3.3 Experimental

The experimental setup consists of a signal generator (SMC100C, Rhode & Schwarz) and amplifier (25A250A, Amplifier Research) connected to LN chips to generate SAWs and micro/nanoparticle suspensions were injected to the PDMS microchannels using a syringe pump (KD Scientific). All tests were observed under an upright microscope (BX43, Olympus) *via* fluorescent light filters (Olympus and Edmund Optics). All images and videos were captured using a top mounted digital camera (Pixelink PL-B782CU and DinoCam). To facilitate timely operation of the signal generator, it was commanded by MATLAB® and simultaneously video capturing was triggered by MATLAB® Image Acquisition Toolbox™.

3.4 Data analysis

The fluorescence light intensity of the videos was processed and analysed by MATLAB to indicate the level of nanoparticle capture and release. As the collection of nanoparticles occurs randomly all over the packed bed area, the grayscale intensity level was calculated by taking the spatial average across the region of interest, *i.e.* the visible part of the packed bed, and recorded against time. This mean intensity level is referred to as Intensity in the plots.

4 Results and discussion

4.1 Collection measurement

The channel used to assess the principle of using microparticle resonance to capture nanoparticles is relatively small, measuring 20 μm by 94 μm (height and width, respectively); this limited size allowed for accurate characterisation and visualisation of the bed. At one end of the channel, a row of pillars was fabricated with a gap size of 6 μm. On either side of the channel, electrodes were deposited on a piezoelectric substrate; the downstream end of these electrodes was aligned with the pillars in the channel. This pair of interdigital transducers (IDTs) is used to excite the standing SAW. The first stage of experimentation was to load the channel with non-fluorescent 10 μm PS particles; the pillars at the end of the channel ensured that these particles were trapped and formed a small packed bed. Subsequently, a 0.04% w/v solution of fluorescent 500 nm PS nanoparticles was pumped through the packed bed at a flow rate of 1 μL h^{-1} (the sequence of loading and operating the system is shown in Fig. 1b). The locations of the nanoparticles within the channel was assessed *en masse*, by examination of the intensity of the fluorescence signal using video microscopy. When the nanoparticles pass through the packed bed without being attracted to the microparticles, an approximately uniform intensity distribution is expected. An intensity increase in the area of the packed bed and a drop in intensity downstream from the bed indicate the occurrence of entrapment, whilst a reversal of this intensity distribution, *i.e.* a higher intensity downstream of the bed, indicates the release of nanoparticles after a trapping event has taken place. These intensity changes have been accentuated by using a very high nanoparticle concentration. Fig. 3 shows an example of this, as the surface acoustic wave actuation is turned on and then off, indicating a clear concentration event occurring within the bed during the period of actuation (Movie S1†).

4.2 Optimum frequencies

We first use these changes in measured intensity to assess the effect of changing the frequency of excitation, to probe the role of microparticle resonance. To make an accurate

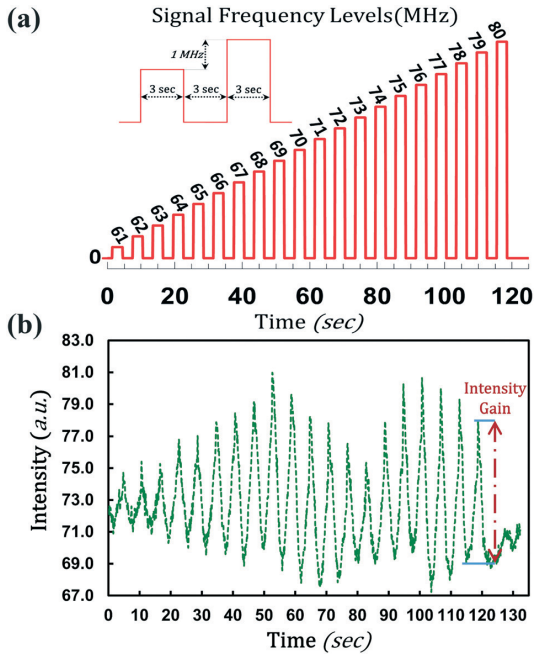

Fig. 4 (a) The frequency response of the system is analysed using a 3 second long pulsed input with constant power (during the ON cycle, 5 dBm); in each subsequent pulse, the frequency is increased by 1 MHz. (b) The mean intensity level, Intensity, in the upstream side of the pillars is measured and by finding the increase in the intensity, Intensity Gain, during the interval of the application of each frequency, optimum frequencies for nanoparticle collection can be found. The NP size in this experiment is 500 nm.

comparison across excitation conditions, we run a single experiment (to avoid any changes in the externally imposed flow conditions or the illumination settings) in which the excitation is repeatedly turned on and off, with each new cycle being at a higher frequency. To achieve this, we use chirped IDTs (*i.e.* electrodes with varied spacing), to provide a wide bandwidth over which useful data can be obtained and are designed such that the particle resonance is within this bandwidth.

Whilst sweeping through the frequencies, a stepped rectangular pulse with a fixed power level was applied as shown in Fig. 4a. The frequency range was 61 MHz to 80 MHz with each pulse 3 seconds long, followed by a 3 second off period (to allow the previously captured particles sufficient time to be washed out of the packed bed by the fluid flow). Over the actuation period, the intensity was found over a fixed area of the packed bed, and is shown in Fig. 4b.

Prior to analysing the data, it is worth noting that although the upstream side of the pillars is fully packed by 10 μm particles over a length considerably longer than the 900 μm long effective SAW length of IDTs, in the absence of excitation, the hydrodynamic influence in collection of the nanoparticles is minimal and can be neglected. The intensity varies over a range of just ±2% (Fig. S2†), whilst in comparison the sound wave activated collection growth rates are 50% and higher within the same time period of 30 s (significantly longer than that used in the data shown in Fig. 4) and experimental conditions.

A second control is the examination of the effect of SAW actuation in the absence of the microparticles, specifically looking at whether the acoustic radiation effects are sufficient to collect the nanoparticles without the Bjerknes forces which the microparticles generate. Under such conditions, whilst some of the nanoparticles are collected along nodal lines, they are not held against the flow so there is no decrease in their presence downstream during actuation (see the video for the control run of nanoparticles flowing through the channel without MPs in Movie S2†).

As a result of these two controls, the rise in the intensity seen as the SAW is actuated in Fig. 4b can be attributed to nanoparticle collection caused by secondary force arising from the presence of the microparticles. Within the short period of each actuation step, the intensity's growth is approximately linear and its gradient or gain (as depicted in Fig. 4b) can interchangeably be considered as a measure of NP collection.

In Fig. 5a and b, the intensity gain at each frequency is shown from Fig. 4b; in addition two other experimental conditions have been analysed. It can be seen that in each case there is a rise in the intensity gain with frequency to an initial peak, at 69 to 72 MHz (simulations predicted 65.7–67.5 MHz, see Table 1) followed by a

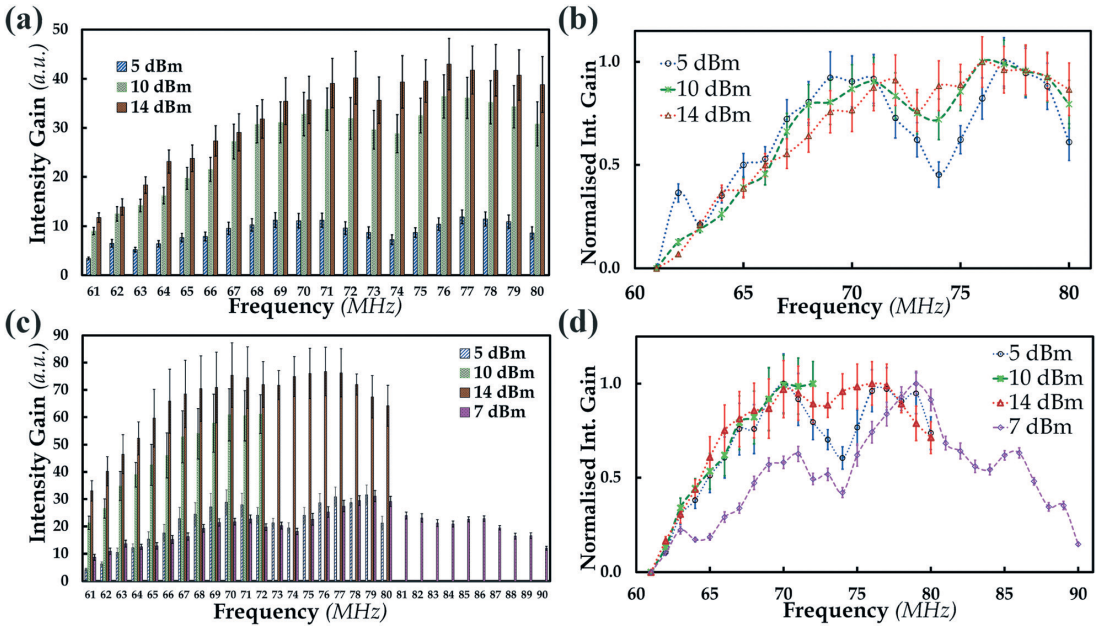

Fig. 5 (a) Upstream, Intensity Gain before normalising for SAW frequencies from 61–80 MHz in a 94 μm × 20 μm channel for 3 different power levels. (b) The normalised intensity gain, Normalised Int. Gain, of each frequency for different power levels at the upstream, (c) downstream results of the absolute Intensity Gain before normalising within the range of 61 to 90 MHz for different power levels, in the same channel. (d) Downstream normalised intensity gain of each frequency for different power levels, where a higher power level provides a greater intensity gain in the same setup, *i.e.* higher collection. The trends in (b) and (d) are similar to numerical simulation (Fig. 2c) with a slight shift in peak/trough frequencies. The NP size in these experiments is 500 nm. The error bars indicate standard error.

View Article Online
Lab on a Chip Paper

trough and then a second peak at 76–78 MHz (simulations predicted 82.5 MHz). The dip in performance, within this frequency range, occurs at 74 MHz (71.2 MHz was predicted).

The slight shift of peaks and troughs in the experiment from the simulation prediction can be attributed to the fact that in the numerical model the material properties are set to a macro-scale reported value while the microbeads' mechanical stiffness and density may differ slightly. This can shift the resonance frequencies and change the mode shapes accordingly. Nonetheless, from these experimental results, it is clear that the behaviour of the packed bed is closely linked to the resonance behaviour of the microparticles (see Fig. S3†). The key features being two peaks and one trough between 60 and 90 MHz, a greater attraction force in the second peak (region C) compared to first one (region B) and eventually a drop of the attraction force (and so NP collection) toward higher frequencies.

It is worth noting that the dip in performance is less pronounced for the two experiments conducted at high power in Fig. 5b and d; we believe that this is because the packed bed is becoming saturated at the higher optimum drive frequencies so the intensity rise seen for them is limited. This saturation can occur very quickly due to the high concentration of nanoparticles used. For most applications, a much lower concentration would be expected; however, for the purpose of characterisation the intensity changes are more reliable using such high concentrations (at lower power levels). To explore this further, a set of experiments were conducted, examining the downstream portion of the channel, over a larger range of frequencies, as shown in Fig. 5c and d. Here, again, consistency is seen across the 5 and 7 dBm cases, with the 14 dBm being the outlier indicating that this power is sufficient to capture the particles even at non-optimal frequencies. In addition, a set of data is included which encompasses higher frequencies. Within in the range previously examined, the trends are very similar, indicating that this is a phenomenon related to the microparticles rather than a quirk in the performance of the IDT sets; above this range we see a further drop in performance which also agrees with simulations.

4.3 Power sweep

We have seen that the relative gain achieved by using the optimum excitation frequencies (70 ± 2 and 77 ± 2 MHz in the case of 10 μm PS beads of the packed bed), influenced by PS resonance frequencies, plays an important role, especially at low powers, at which we observed a peak–trough difference in the order of 60–70%. At higher powers, this contrast differed (between 12 and 23%) due to saturation. Here, however, we examine the effect of power more thoroughly, and examine the performance (*via* intensity changes) as a function of power, using a swept power experiment.

To investigate the power effect, a stepped rectangular SAW pulse was introduced to the system. Starting from 1 dBm (equivalent 1.26 mW), each pulse lasted for 3 seconds followed by a 6 second off period and the step level increased by 1 dBm at each increment up to a limit of 14 dBm (equivalent to 25.12 mW). The pulse diagram along with the real-time mean intensity level (Intensity) for the downstream of the 94 μm × 20 μm channel is given in Fig. 6a and the intensity gain for 3 different frequencies at each power level that changes linearly is shown in Fig. 6b.

4.4 Capture performance and enrichment return

4.4.1 Capture efficiency. To investigate the capture performance of the SWANS system, a further set of experiments was run; this was done over a range of frequencies, but here each actuation was sustained for a longer period of time than that used in the frequency sweep experiment. The range used was between 55 MHz and 85 MHz at a fixed power level of 12 dBm. The flow rate was kept at 1 μL h^{-1} in a 94 μm × 20 μm channel and the intensity level was measured downstream of the micropillar posts and was used to quantify the percentage of NPs which were not trapped. Ideally, if all NPs are trapped at the upstream, the light intensity emitted from fluorescent NPs in the downstream area will drop to zero upon actuation; hence, the capture performance of the nanoparticle sieve is 100%. The method for measuring this performance for a sample frequency is described further in the ESI† (Fig. S5). The results, although only for representative frequencies,

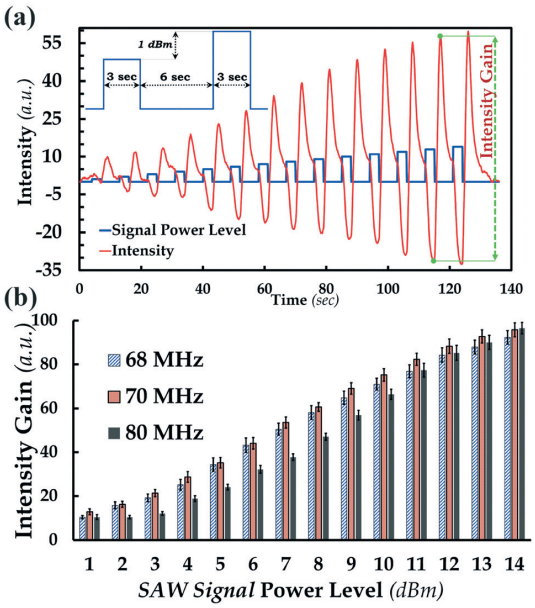

Fig. 6 The power response of the system is shown. (a) The instantaneous intensity (downstream in the 94 μm × 20 μm channel) at 68 MHz (in red), shown alongside the stepped pulse power sweep: 1 to 14 dBm. (b) The intensity gains at different frequencies show linear compliance with the power level in dBm (see Fig. S4† for linear regression errors). The NP size in these experiments is 500 nm. The error bars indicate standard error.

View Article Online
Paper Lab on a Chip

show a similar trend, that is, by increasing the frequency the capture efficiency also increases, reaching a peak, and drops after that. It can be seen that at a frequency of 80 MHz (very close to the second peak discussed earlier) we can achieve a capture efficiency, $\eta_{capture}$, of approximately 97%, Fig. 7a. For other frequencies, increasing the power will increase the intensity at the upstream and symmetrically decrease it at the downstream, as can be seen Fig. 6a; in other words, a higher capture efficiency is achievable.

It is worth noting that at such high capture rates, a further increase in power would not make a difference to the intensity which is observed; this too (along with saturation of the bed) explains why in the frequency sweep experiments at the highest power used, 14 dBm, operation at the optimal frequencies is not seen to provide more capture than off resonance.

4.4.2 Enrichment return. After realising the optimum frequency and power level that provides a reasonably high capture efficiency, the final concentration of the trapped batch of nanoparticles will be a function of time, channel size and flow rate. After a certain time of the SAW being active, t, in a flow with a known flow rate, Q, and initial concentration, R_i, the mass of nanoparticles trapped in the trapping area, m_{NP}, and the final concentration, R_f, are:

$$m_{NP} = \eta_{capture} \times R_i \times Q \times t \quad (1)$$

$$R_f = \frac{m_{NP}}{V_{chamber}} \quad (2)$$

where $\eta_{capture}$ is the capture efficiency of the SWANS under particular SAW conditions (frequency and power) and $V_{chamber}$ is the volume of the trapping area. This area only encompasses the SAW influenced part of the whole packed bed. While in the tested devices, after loading the MPs, the packed bed is filled and covers an area beyond the SAW beam; however microparticles outside the SAW beam are not observed to assist in NP trapping. To confirm this, Fig. 7d shows that in a 94 μm × 20 μm channel at the end of an experiment with 190 nm PS particles, the SAW activated area, which is slightly wider than the IDT aperture,[96,97] clearly has a brighter intensity (due to the collection of NPs) than parts of the packed bed upstream of the SAW beam. We use $V_{chamber}$ to define

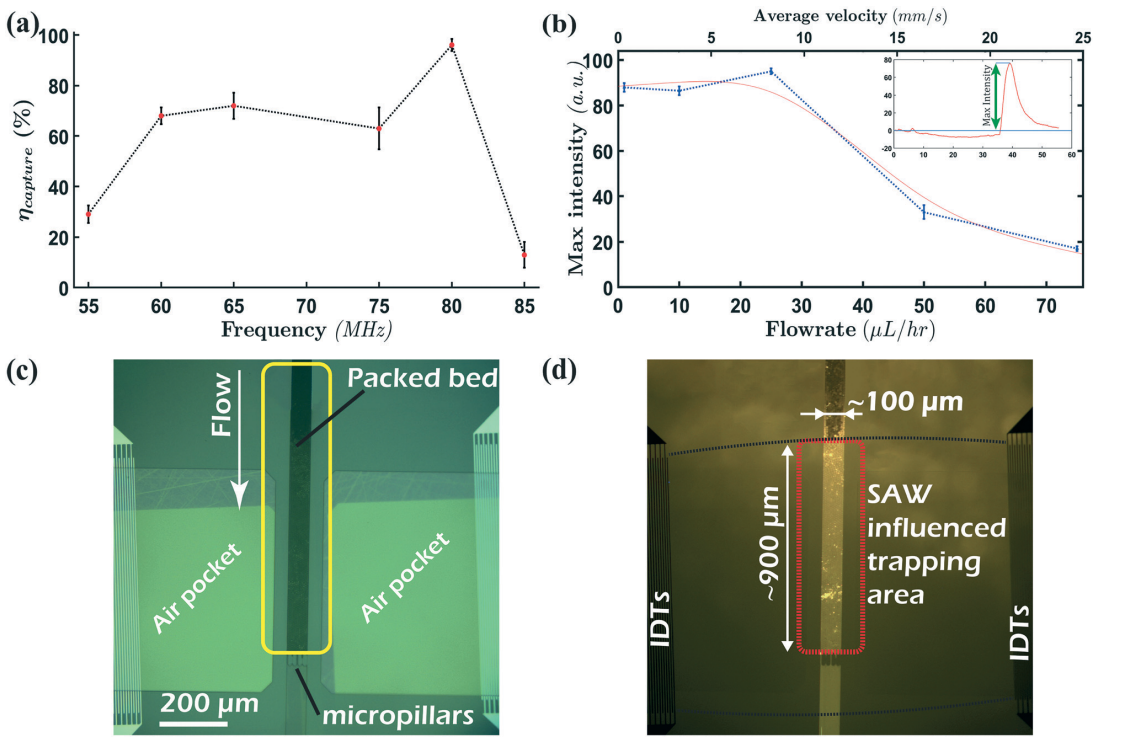

Fig. 7 (a) Capture efficiency at selected frequencies at a fixed power level of 12 dBm in a 94 μm × 20 μm channel. (b) Downstream maximum intensity in a 50 μm × 20 μm channel for different flow rates at 70 MHz, 14 dBm. (c) The packed bed fills the channel beyond the SAW beam. The fluorescent filter of the same caption shows the effective trapping area of the packed bed (d). Microparticles outside of this area (*i.e.* upstream of it) have a negligible part in the capture, confirming the need for microparticles and SAW excitation and defining the effective volume of the filter. The NP size in experiments of (a) and (b) is 500 nm and that of (c) and (d) is 190 nm. The error bars indicate standard error.

View Article Online
Lab on a Chip Paper

the volume of this part and for the case shown in Fig. 7c and d it is about $V_{chamber} = 900 \times 100 \times 20\ (\mu m)^3 = 1.8$ nL. Rearranging eqn (1) and (2), the concentration return can be expressed as follows:

$$\frac{R_i}{R_i} = \eta_{capture} \times \left(\frac{Q}{V_{chamber}} \right) \times t \quad (3)$$

For this small bed, this is valid within short periods of time as enrichment cannot increase endlessly and linearly. In a set of experiments run in a 50 μm wide and 20 μm high channel under 70 MHz and 14 dBm SAW signal conditions, after measuring the maximum intensity at the downstream (as an indication of the maximum number of captured nanoparticles with 500 nm size) against different flow rates, it can be seen that this maximum intensity is retained up to 25 μL h^{-1} flow rate which corresponds to an average velocity of 6900 μm s^{-1}, Fig. 7b. Assuming a conservative capture efficiency of 0.7 at the 14 dBm level, within a 10 s period of SAW operation the concentration return is about 54. Hence, SWANS has the capability of about 50-fold enrichment of the nanoparticles within a very short time. By scaling up, the chamber volume $V_{chamber}$ increases and to maintain the return ratio, the flow rate can increase thus enabling the SWANS system to handle larger sample volumes.

4.4.3 Effect of nanoparticle size. We further investigated the operability of the SWANS system for smaller nanoparticles. Our characterisation of the role of frequency and power has utilised 500 nm polystyrene beads, taking advantage of the brightness of fluorescence they offer for high quality data collection. That study clearly showed two ranges over which the collection of nanoparticles is optimal. In that study, the power had to be limited in order to observe the effect of frequency, as at high powers a mixture of total capture and bed saturation caused a maximum intensity change to be reached. In terms of the operation of the system, this clearly demonstrates that there is unused capacity in the operational range. Here, we utilise this, by turning up the power, to address the more challenging task of capturing smaller particles. We note here that the broadband width chirped IDTs are still used for this task, and that this too offers additional scope for enhancement as single frequency IDTs are considerably more efficient.

The frequency of 72 MHz is within the range of the first peak; to study how this set of conditions can be used to capture smaller objects, in a 94 μm × 20 μm channel, experiments were separately performed for 190 nm and 100 nm polystyrene nanoparticles with 0.3% w/v and 0.007% w/v concentrations, respectively, both at a 1 μL h^{-1} flow rate.

A 72 MHz SAW at 18 dBm is used to activate the bed. Fig. 8a-2 shows the intensity changes resulting from the capture of 190 nm particles in the bed. Upon turning off the ultrasonic actuation, the concentration of nanoparticles upstream drops quickly with the transition region between high and low intensity moving downstream with the flow (Fig. 8a-3). A few seconds after the end of SAW activation, the fluorescence intensity returns to its initial level (Fig. 8a-4).

Similarly, the solution of 100 nm particles went through the collection, enrichments and release cycle at 72 MHz frequency and 18 dBm power level; however, due to the smaller size of the 100 nm particles, although the collection takes place and the release of trapped particles can be observed from Fig. 8b-3, it is less distinct. The acoustic radiation forces on nanoparticles can be presumed to be proportional to the volume of the particle, and hence to the cube of its diameter, from Gor'kov[98] and Weiser.[99] To counter this, a further increase in the power by just 50% shows a more clearly evident collection of 100 nm particles under otherwise identical conditions (Fig. 8c). The comparison of stages 2 and 3 in Fig. 8b and c demonstrates that adjusting to a suitable power level effectively traps 100 nm particles in the packed bed (evident from the intensity drop at the downstream) and swiftly releases the enriched batch with its propagating front to the downstream (Movie S3j†).

The series of experiments have been designed to demonstrate the role of microparticle resonance in the capture of

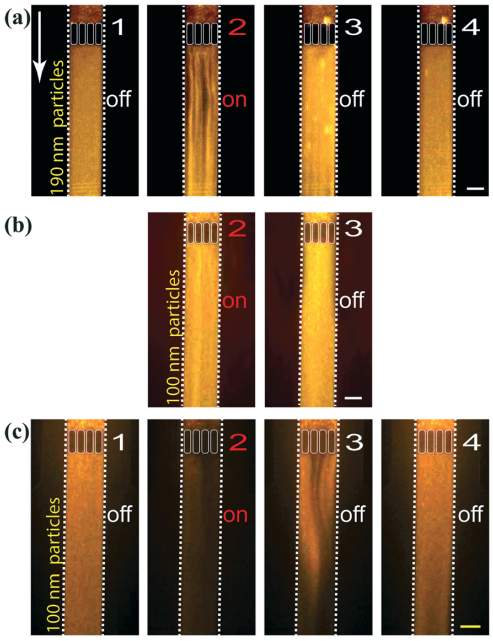

Fig. 8 (a) The downstream view of trapping 190 nm polystyrene particles. Each sequence follows: (1) before SAW activation, (2) during SAW activation, (3) instantly upon turning off the SAW and (4) seconds after activation ends. (b) The downstream view of SWANS with 100 nm polystyrene particles shown at stages (2) and (3). The capture occurs; however, it is not significant due to the smaller size of the NPs. At a higher power level, (c) capture of 100 nm polystyrene beads is shown by (2) the drop in downstream intensity while the SAW is activated and (3) the noticeable release of the enriched batch upon turning the SAW off. The arrow shows the flow that is downward for all captions and the scale bar is 50 μm.

nanoparticles. To this end, several requirements were imposed for the acquisition of high-quality data. It was necessary to use relatively large particles (500 nm) such that the image intensity was significant, and to perform the experiments in a small system to further assist visualisation. It was then observed that at high powers, the role of frequency is blurred by the fairly efficient capture at even sub-optimal frequencies. We have referred to the necessity to drop the power level to observe the resonant behaviour as demonstrating the excess operational capacity, and then later utilised that capacity to capture smaller particles. However, it is also worth noting that the intensity of the sound field can be further increased by more efficient transduction from electrical power into surface acoustic waves. To study frequency effects, it is necessary to use a broadband IDT set with variable pitch electrodes, in which the optimum pitch for SAW generation only occurs across a few electrodes. Operation of a single frequency, constant pitch IDT offers considerably higher efficiency, and hence additional capacity for improved performance.

5 Conclusions

The concept of a mechanically activated packed bed has been presented and shown to be capable of entrapment and enrichment of nanoparticles in a continuous flow. The activation is in the form of ultrasonic excitation which is shown, both numerically and experimentally, to be most efficient when the frequency is chosen such that it coincides with a resonant mode of the microparticles forming the packed bed. Under these conditions, firstly, the bed itself is stable as the microparticles are attracted to each other. Secondly, when a solution of nanoparticles passes through the bed, they too are attracted to the microparticles and become captured on their surface. Hence filtration is achieved without the need for chemical functionalisation of the bed in a manner which is reversible, such that an enriched sample can be collected. The filtration does not block the bed, and, in contrast to membrane filtration, the pore size is dictated by the size of the microparticles rather than the nanoparticles. At a power of 12 dBm, 97% of the 500 nm particles passed through a bed activated at a resonance frequency of 80 MHz were collected. In addition, the collection of both 190 and 100 nm particles was shown at higher powers. As the resonance is related to the components of the bed, rather than the bed size, there is excellent potential for upscaling, having, in this work, demonstrated the underlying physics.

Conflicts of interest

There are no conflicts to declare.

Acknowledgements

This work is funded by the Australian Research Council by way of grant no. DP160101263. This work was performed in part at the Melbourne Centre for Nanofabrication (MCN) in the Victorian Node of the Australian National Fabrication Facility (ANFF).

References

1 S.-H. Wu and D.-H. Chen, *J. Colloid Interface Sci.*, 2004, **273**, 165–169.
2 M. Gericke and A. Pinches, *Hydrometallurgy*, 2006, **83**, 132–140.
3 F. G. Mitri and D. N. Sinha, *2011 IEEE International Ultrasonics Symposium*, 2011.
4 Z. Lin, Z. Xia, J. Zheng, D. Zheng, L. Zhang, H. Yang and G. Chen, *J. Mater. Chem.*, 2012, **22**, 17914–17922.
5 P. M. Valencia, O. C. Farokhzad, R. Karnik and R. Langer, *Nat. Nanotechnol.*, 2012, **7**, 623.
6 J. L. Corchero and A. Villaverde, *Trends Biotechnol.*, 2009, **27**, 468–476.
7 B. Podbilewicz, *Annu. Rev. Cell Dev. Biol.*, 2014, **30**, 111–139.
8 M. J. Rohovie, M. Nagasawa and J. R. Swartz, *Bioeng. Transl. Med.*, 2017, **2**, 43–57.
9 S. Wang, X. Zhang, B. Yu, R. J. Lee and L. J. Lee, *Biosens. Bioelectron.*, 2010, **26**, 778–783.
10 B. Kim, H.-B. Pang, J. Kang, J.-H. Park, E. Ruoslahti and M. J. Sailor, *Nat. Commun.*, 2018, **9**, 1969.
11 J. Sun, Y. Xianyu and X. Jiang, *Chem. Soc. Rev.*, 2014, **43**, 6239–6253.
12 W. S. Bauer, C. P. Gulka, L. Silva-Baucage, N. M. Adams, F. R. Haselton and D. W. Wright, *Anal. Chem.*, 2017, **89**, 10216–10223.
13 Y. Ha, S. Ko, I. Kim, Y. Huang, K. Mohanty, C. Huh and J. A. Maynard, *ACS Appl. Nano Mater.*, 2018, **1**, 512–521.
14 J. Wen, L. A. Legendre, J. M. Bienvenue and J. P. Landers, *Anal. Chem.*, 2008, **80**, 6472–6479.
15 C. Chen, J. Skog, C.-H. Hsu, R. T. Lessard, L. Balaj, T. Wurdinger, B. S. Carter, X. O. Breakefield, M. Toner and D. Irimia, *Lab Chip*, 2010, **10**, 505–511.
16 G. D. Chen, C. J. Alberts, W. Rodriguez and M. Toner, *Anal. Chem.*, 2010, **82**, 723–728.
17 J. Yoon, Y.-J. Yoon, T. Y. Lee, M. K. Park, J. Chung and Y. Shin, *Sens. Actuators, B*, 2018, **255**, 1491–1499.
18 Z. Ma, J. Guo, Y. J. Liu and Y. Ai, *Nanoscale*, 2015, **7**, 14047–14054.
19 Y. Lee, S. E. L. Andaloussi and M. J. Wood, *Hum. Mol. Genet.*, 2012, **21**, R125–R134.
20 O. G. De Jong, B. W. M. Van Balkom, R. M. Schiffelers, C. V. C. Bouten and M. C. Verhaar, *Front. Immunol.*, 2014, **5**, 608.
21 A. Thind and C. Wilson, *J. Extracell. Vesicles*, 2016, **5**, 31292.
22 P. Li, M. Kaslan, S. H. Lee, J. Yao and Z. Gao, *Theranostics*, 2017, **7**, 789–804.
23 G. Raposo and W. Stoorvogel, *J. Cell Biol.*, 2013, **200**, 373–383.
24 E. Cocucci and J. Meldolesi, *Trends Cell Biol.*, 2015, **25**, 364–372.
25 W. Wang, J. Luo and S. Wang, *Adv. Healthcare Mater.*, 2018, **7**, 1800484.

26 F. Momen-Heravi, L. Balaj, S. Alian, P.-Y. Mantel, A. E. Halleck, A. J. Trachtenberg, C. E. Soria, S. Oquin, C. M. Bonebreak, E. Saracoglu, S. Johan and K. W. Patrick, *Biol. Chem.*, 2013, **394**, 1253.

27 L. Mincheva-Nilsson, V. Baranov, O. Nagaeva and E. Dehlin, *Curr. Protoc. Immunol.*, 2016, **115**, 14.42.1–14.42.21.

28 F. Liu, O. Vermesh, V. Mani, T. J. Ge, S. J. Madsen, A. Sabour, E.-C. Hsu, G. Gowrishankar, M. Kanada, J. V. Jokerst, R. G. Sierra, E. Chang, K. Lau, K. Sridhar, A. Bermudez, S. J. Pitteri, T. Stoyanova, R. Sinclair, V. S. Nair, S. S. Gambhir and U. Demirci, *ACS Nano*, 2017, **11**, 10712–10723.

29 K. Liang, F. Liu, J. Fan, D. Sun, C. Liu, C. J. Lyon, D. W. Bernard, Y. Li, K. Yokoi, M. H. Katz, E. J. Koay, Z. Zhao and Y. Hu, *Nat. Biomed. Eng.*, 2017, **1**, 0021.

30 A. Ghosh, M. Davey, I. C. Chute, S. G. Griffiths, S. Lewis, S. Chacko, D. Barnett, N. Crapoulet, S. Fournier, A. Joy, M. C. Caissie, A. D. Ferguson, M. Daigle, M. V. Meli, S. M. Lewis and R. J. Ouellette, *PLoS One*, 2014, **9**, 1–12.

31 I. Lozano-Ramos, I. Bancu, A. Oliveira-Tercero, M. P. Armengol, A. Menezes-Neto, H. A. D. Portillo, R. Lauzurica-Valdemoros and F. E. Borrás, *J. Extracell. Vesicles*, 2015, **4**, 27369.

32 C. Manri, T. Yokoi and H. Nishida, *Appl. Biochem. Biotechnol.*, 2017, **182**, 609–623.

33 J. Caradec, G. Kharmate, E. Hosseini-Beheshti, H. Adomat, M. Gleave and E. Guns, *Clin. Biochem.*, 2014, **47**, 1286–1292.

34 K. Yakimchuk, *Mater. Methods*, 2015, **5**, 1450–1453.

35 A. Safdar, A. Saleem and M. A. Tarnopolsky, *Nat. Rev. Endocrinol.*, 2016, **12**, 504.

36 J. J. Lai, J. M. Hoffman, M. Ebara, A. S. Hoffman, C. Estournés, A. Wattiaux and P. S. Stayton, *Langmuir*, 2007, **23**, 7385–7391.

37 A. Liga, A. D. B. Vliegenthart, W. Oosthuyzen, J. W. Dear and M. Kersaudy-Kerhoas, *Lab Chip*, 2015, **15**, 2388–2394.

38 T. Salafi, K. K. Zeming and Y. Zhang, *Lab Chip*, 2017, **17**, 11–33.

39 J. Nilsson, M. Evander, B. Hammarström and T. Laurell, *Anal. Chim. Acta*, 2009, **649**, 141–157.

40 Z. Wang, H.-j. Wu, D. Fine, J. Schmulen, Y. Hu, B. Godin, J. X. J. Zhang and X. Liu, *Lab Chip*, 2013, **13**, 2879–2882.

41 B. H. Wunsch, J. T. Smith, S. M. Gifford, C. Wang, M. Brink, R. L. Bruce, R. H. Austin, G. Stolovitzky and Y. Astier, *Nat. Nanotechnol.*, 2016, **11**, 936.

42 R. T. Davies, J. Kim, S. C. Jang, E.-J. Choi, Y. S. Gho and J. Park, *Lab Chip*, 2012, **12**, 5202–5210.

43 A. M. Leshansky, A. Bransky, N. Korin and U. Dinnar, *Phys. Rev. Lett.*, 2007, **98**, 234501.

44 E. J. Lim, T. J. Ober, J. F. Edd, S. P. Desai, D. Neal, K. W. Bong, P. S. Doyle, G. H. McKinley and M. Toner, *Nat. Commun.*, 2014, **5**, 4120.

45 C. Liu, J. Guo, F. Tian, N. Yang, F. Yan, Y. Ding, J. Wei, G. Hu, G. Nie and J. Sun, *ACS Nano*, 2017, **11**, 6968–6976.

46 P. Chiou, A. T. Ohta, A. Jamshidi, H. Hsu and M. C. Wu, *J. Microelectromech. Syst.*, 2008, **17**, 525–531.

47 R. T. Turgeon and M. T. Bowser, *Anal. Bioanal. Chem.*, 2009, **394**, 187–198.

48 M. Viefhues, R. Eichhorn, E. Fredrich, J. Regtmeier and D. Anselmetti, *Lab Chip*, 2012, **12**, 485–494.

49 H. Cong, J. Chen and H.-P. Ho, *Sens. Actuators, B*, 2018, **264**, 224–233.

50 S. H. S. Lee, T. A. Hatton and S. A. Khan, *Microfluid. Nanofluid.*, 2011, **11**, 429.

51 A. Tay, A. Kunze, D. Jun, E. Hoek and D. Di Carlo, *Small*, 2016, **12**, 3559–3567.

52 Z. Zhao, Y. Yang, Y. Zeng and M. He, *Lab Chip*, 2016, **16**, 489–496.

53 D. J. Collins, T. Alan and A. Neild, *Lab Chip*, 2014, **14**, 1595–1603.

54 D. J. Collins, Z. Ma and Y. Ai, *Anal. Chem.*, 2016, **88**, 5513–5522.

55 Z. Mao, P. Li, M. Wu, H. Bachman, N. Mesyngier, X. Guo, S. Liu, F. Costanzo and T. J. Huang, *ACS Nano*, 2017, **11**, 603–612.

56 M. Wu, Z. Mao, K. Chen, H. Bachman, Y. Chen, J. Rufo, L. Ren, P. Li, L. Wang and T. J. Huang, *Adv. Funct. Mater.*, 2017, **27**, 1606039.

57 A. H. J. Yang, S. D. Moore, B. S. Schmidt, M. Klug, M. Lipson and D. Erickson, *Nature*, 2009, **457**, 71.

58 S. J. Williams, A. Kumar, N. G. Green and S. T. Wereley, *Nanoscale*, 2009, **1**, 133–137.

59 G. P. Gautam, R. Gurung, F. A. Fencl and M. E. Piyasena, *Anal. Bioanal. Chem.*, 2018, **410**, 6561–6571.

60 D. J. Collins, B. Morahan, J. Garcia-Bustos, C. Doerig, M. Plebanski and A. Neild, *Nat. Commun.*, 2015, **6**, 8686.

61 P. Glynne-Jones, R. J. Boltryk, N. R. Harris, A. W. Cranny and M. Hill, *Ultrasonics*, 2010, **50**, 68–75.

62 J. Behrens, S. Langelier, A. R. Rezk, G. Lindner, L. Y. Yeo and J. R. Friend, *Lab Chip*, 2015, **15**, 43–46.

63 B. W. Drinkwater, *Lab Chip*, 2016, **16**, 2360–2375.

64 A. Franklin, A. Marzo, R. Malkin and B. W. Drinkwater, *Appl. Phys. Lett.*, 2017, **111**, 094101.

65 A. Haake, A. Neild, G. Radziwill and J. Dual, *Biotechnol. Bioeng.*, 2005, **92**, 8–14.

66 J. P. Lata, F. Guo, J. Guo, P.-H. Huang, J. Yang and T. J. Huang, *Adv. Mater.*, 2016, **28**, 8632–8638.

67 J. P. K. Armstrong, J. L. Puetzer, A. Serio, A. G. Guex, M. Kapnisi, A. Breant, Y. Zong, V. Assal, S. C. Skaalure, O. King, T. Murty, C. Meinert, A. C. Franklin, P. G. Bassindale, M. K. Nichols, C. M. Terracciano, D. W. Hutmacher, B. W. Drinkwater, T. J. Klein, A. W. Perriman and M. M. Stevens, *Adv. Mater.*, 2018, **30**, 1802649.

68 B. Raeymaekers, C. Pantea and D. N. Sinha, *J. Appl. Phys.*, 2011, **109**, 014317.

69 K. Lee, H. Shao, R. Weissleder and H. Lee, *ACS Nano*, 2015, **9**, 2321–2327.

70 P. Sehgal and B. J. Kirby, *Anal. Chem.*, 2017, **89**, 12192–12200.

71 P. B. Muller, R. Barnkob, M. J. H. Jensen and H. Bruus, *Lab Chip*, 2012, **12**, 4617–4627.

72 C. Devendran, I. Gralinski and A. Neild, *Microfluid. Nanofluid.*, 2014, **17**, 879–890.
73 C. Reyes, L. Fu, P. P. A. Suthanthiraraj, C. E. Owens, C. W. Shields IV, G. P. López, P. Charbonneau and B. J. Wiley, *Part. Part. Syst. Charact.*, 2018, **35**, 1700470.
74 M. Antfolk, P. B. Muller, P. Augustsson, H. Bruus and T. Laurell, *Lab Chip*, 2014, **14**, 2791–2799.
75 M. Evander, L. Johansson, T. Lilliehorn, J. Piskur, M. Lindvall, S. Johansson, M. Almqvist, T. Laurell and J. Nilsson, *Anal. Chem.*, 2007, **79**, 2984–2991.
76 H. V. Phan, M. Şeşen, T. Alan and A. Neild, *Appl. Phys. Lett.*, 2014, **105**, 193507.
77 D. J. Collins, B. L. Khoo, Z. Ma, A. Winkler, R. Weser, H. Schmidt, J. Han and Y. Ai, *Lab Chip*, 2017, **17**, 1769–1777.
78 J. T. Karlsen, W. Qiu, P. Augustsson and H. Bruus, *Phys. Rev. Lett.*, 2018, **120**, 054501.
79 A. Fakhfouri, C. Devendran, A. Ahmed, J. Soria and A. Neild, *Lab Chip*, 2018, **18**, 3926–3938.
80 B. Hammarström, T. Laurell and J. Nilsson, *Lab Chip*, 2012, **12**, 4296–4304.
81 M. Tenje, H. Xia, M. Evander, B. Hammarström, A. Tojo, S. Belák, T. Laurell and N. LeBlanc, *Anal. Chim. Acta*, 2015, **853**, 682–688.
82 M. Evander, O. Gidlöf, B. Olde, D. Erlinge and T. Laurell, *Lab Chip*, 2015, **15**, 2588–2596.
83 P. Ohlsson, M. Evander, K. Petersson, L. Mellhammar, A. Lehmusvuori, U. Karhunen, M. Soikkeli, T. Seppä, E. Tuunainen, A. Spangar, P. von Lode, K. Rantakokko-Jalava, G. Otto, S. Scheding, T. Soukka, S. Wittfooth and T. Laurell, *Anal. Chem.*, 2016, **88**, 9403–9411.
84 K.-M. Yao, M. T. Habibian and C. R. O'Melia, *Environ. Sci. Technol.*, 1971, **5**, 1105–1112.
85 L. M. McDowell-Boyer, J. R. Hunt and N. Sitar, *Water Resour. Res.*, 1986, **22**, 1901–1921.
86 F. V. Tinaut, A. Melgar, J. F. Pérez and A. Horrillo, *Fuel Process. Technol.*, 2008, **89**, 1076–1089.
87 R. D. Oleschuk, L. L. Shultz-Lockyear, Y. Ning and D. J. Harrison, *Anal. Chem.*, 2000, **72**, 585–590.
88 M. A. M. Gijs, F. Lacharme and U. Lehmann, *Chem. Rev.*, 2010, **110**, 1518–1563.
89 H. Shao, J. Chung, K. Lee, L. Balaj, C. Min, B. S. Carter, F. H. Hochberg, X. O. Breakefield, H. Lee and R. Weissleder, *Nat. Commun.*, 2015, **6**, 6999.
90 G. Destgeer, K. H. Lee, J. H. Jung, A. Alazzam and H. J. Sung, *Lab Chip*, 2013, **13**, 4210–4216.
91 H. Ahmed, G. Destgeer, J. Park, M. Afzal and H. J. Sung, *Anal. Chem.*, 2018, **90**, 8546–8552.
92 R. Habibi, C. Devendran and A. Neild, *Lab Chip*, 2017, **17**, 3279–3290.
93 G. T. Silva, J. H. Lopes, J. P. Leão Neto, M. K. Nichols and B. W. Drinkwater, *Phys. Rev. Appl.*, 2019, **11**, 054044.
94 M. Settnes and H. Bruus, *Phys. Rev. E: Stat., Nonlinear, Soft Matter Phys.*, 2012, **85**, 016327.
95 S. Sepehrirahnama, F. S. Chau and K.-M. Lim, *Phys. Rev. E*, 2016, **93**, 023307.
96 A. Winkler, S. Harazim, D. Collins, R. Brünig, H. Schmidt and S. Menzel, *Biomed. Microdevices*, 2017, **19**, 9.
97 D. J. Collins, C. Devendran, Z. Ma, J. W. Ng, A. Neild and Y. Ai, *Sci. Adv.*, 2016, **2**, e1600089.
98 L. Gor'Kov, *Sov. Phys. Dokl.*, 1962, 773.
99 M. Weiser, R. Apfel and E. Neppiras, *Acta Acust. Acust.*, 1984, **56**, 114–119.

Supporting Information (SI) for: Sound Wave Activated Nano-Sieve (S.W.A.N.S) for Enrichment of Nanoparticles†

Ruhollah Habibi
LMS, Monash University

Adrian Neild*
LMS, Monash University

I. Theory and numerical models

The methodology of the numerical simulations and theory behind them are established on the basis Habibi et al.'s work.[1] The application of the perturbation theory into time-dependent oscillating pressure, velocity and density fields is explained in that work. After plugging them into the continuity and Navier-Stokes equations and taking time average, the second-order pressure integrated over the surface of the particle provides the force, $\boldsymbol{F}$, applied on the particle:

$$\langle \boldsymbol{F} \rangle = \int_{S_0} \frac{\rho_0}{2} \langle v_1^2 \rangle \boldsymbol{n} d\boldsymbol{S} - \int_{S_0} \frac{1}{2\rho_0 c_a^2} \langle P_1^2 \rangle \boldsymbol{n} d\boldsymbol{S} - \int_{S_0} \rho_0 \langle (\boldsymbol{n} \cdot \boldsymbol{v_1}) \boldsymbol{v_1} \rangle d\boldsymbol{S}\,, \tag{1}$$

Where ρ_0 is the fluid density at rest, c_a the speed of sound in the fluid and v_1 and P_1 are the first-order velocity and pressure terms, respectively. Here, $\boldsymbol{n}$ represents the normal vector of the particle's surface, $\boldsymbol{S}$ and the integration is performed over the initial surface, S_0. $\langle\rangle$ denotes the time average operator.

Similar to the referenced work, the finite element method (FEM) model was constructed in COMSOL Multiphysics® 5.1 to investigate acoustic radiation forces on micro and nanoscale polystyrene particles.

Firstly, the frequency effect on the acoustic radiation force on a single 10 μm polystyrene particle was conducted in a 2D antisymmetric space that provided the primary force results with distinguishable regions. The basic parameters of the FEM model and materials properties are given in Table S1 under **2DAxi-1P**.

Similarly, the primary, total and consequently secondary (Bjerknes) acoustic radiation forces on a nanoparticle were investigated in a 2D antisymmetric space FEM model of two particles, a 10 μm as the microparticle and one 500 nm as the nanoparticle, positioned around an anti-node with

*Corresponding author: Laboratory for Micro Systems, Department of Mechanical and Aerospace Engineering, Monash University, Clayton, Victoria 3800, Australia.; E-mail: adrian.neild@monash.edu

Table S1: *Basic parameters of the FEM models that were simulated in this work. Material data are obtained from COMSOL material library otherwise stated. The values of parameters are given for each FEM model, single 10 μm polystyrene particle under 2DAxi-1P, the interaction of one microparticle and one nanoparticle under 2DAxi-2P and a cluster of microparticles as the packed bed under 2D-MMP.*

Parameter	Symbol	Unit	**2DAxi–1P**	**2DAxi– 2P**	**2D-MMP**
Fluid Domain					
Water					
Density	ρ_f	kg m^{-3}	1000	1000	1000
Speed of sound	c_f	m s^{-1}	1500	1500	1500
Domain height	L	μm	100	40	$\lambda\times3$
Domain width	W	μm	50	15	$\lambda\times2$
Frequency	f	MHz	15∼105	15∼105	15
Wavelength	λ	μm	c_f/f	c_f/f	100
Wavenumber	k	μm	$2\pi/\lambda$	$2\pi/\lambda$	$2\pi/\lambda$
Acoustic pressure amp.	P_0	kPa	100	100	100
Mesh size range	e_f	μm	0.03∼1	0.02∼0.6	0.01∼1
Curvature factor		-	0.3	0.1	0.15
Max. mesh growth rate		-	1.05	1.08	1.3
Solid Domain					
Polystyrene					
Density[3]	ρ_{ps}	kg m^{-3}	1050	1050	1050
Modulus of elasticity[a]	E_{ps}	GPa	3.60	3.60	3.60
Poisson ratio[4]	ν_{ps}	-	0.35	0.35	0.35
Domain dimensions:					
Microparticle diameter	d	μm	10	10	$0.31\times\lambda$
Microparticle radius	R	μm	5	5	d/2
Nanoparticle diameter	d_{NP}	μm	n/a	0.5	n/a
Nanoparticle radius	R_{NP}	μm	n/a	0.25	n/a
Gap between particles	Gap	μm	n/a	$\lambda/200$	0
Mesh size range	e_s	μm	0.03∼0.5	0.02∼2	0.01∼R/10
Curvature factor		-	0.2	0.15	0.3
Max. mesh growth rate		-	1.1	1.05	1.3
Fluid-Solid interface					
Mesh size range	e_1	μm	0.03∼0.2	0.004∼0.02	0.01∼0.1
Curvature factor		-	0.15	0.15	0.15
Max. mesh growth rate		-	1.05	1.05	1.05

[a] Calculated from Bulk Modulus (K_{ps}) as $E_{ps} = 3K_{ps}(1-2\nu_{ps})$ from ref. 4 and 5.

the normalised Gap of $\lambda/200$ with frequency range of 15 to 105 MHz (that corresponds to the microparticle's normalised size of d/λ from 0.1 to 0.7). The values of parameters and properties of this stage of the simulation are presented under **2DAxi-2P** in Table S1.

To investigate the presence of multiple microparticles and the shape of force field around them when at a frequency in region B and close to resonance, a 2D space dimension was used. To represent a packed bed, the *Gap* between microparticles was considered zero. The forces on 500 nm particles were computed based on Gor'kov[2] formulation and due to the varying scale of the force vectors, for the purpose of visualisation, all vectors were normalised that still provide information on the direction of force field. The parameters details of this section are given in Table S1 under **2D-MMP**.

II. Operation sequence

The sequences of the operation of SWANS system is shown in Fig. 1b of the main article where channels are washed with distilled water and then 2% PEG water solution as the first step *(i)*. This is to wet the channels and to ensure no large debris would be present in the test channel, suspensions are filtered at the inlet. The second stage is the loading of the microparticles suspended in 2% PEG water solution to create the packed bed *(ii)*. After the completion of packed bed loading, when the length of the packed bed covers IDT's aperture and beyond it providing packed bed's stability at resonance, the solution of nanoparticles at desired concentration and flowrate is loaded to the microchannel *(iii)*. The pores between microparticles are large enough to provide a smooth flow of the nanoparticles. When the collection of the nanoparticles is in demand, IDTs are activated at a certain frequency that generates the surface acoustic wave (SAW) and consequently entraps nanoparticles *(iv)*. The collected batch of nanoparticles in the upstream has a high concentration now and can be released to the downstream on demand by de-energising of the IDTs *(v)*.

III. Effect of hydrodynamic resistance on the collection

The packed bed creates a hydrodynamic effect on the flow and the passage of the nanoparticles, increasing the resistance against the flow, however, due to the size of the pores (approximately about 4 μm), 500 nm can pass freely. There might be some random entrapments of nanoparticles at the boundary of those pores in long run, however, its effect is very minor and can be neglected in comparison to the collection due to primary and secondary forces applied on the nanoparticles. The slopes of black dotted and dashed black lines in Fig. S2 as an indication of intensity growth over the SAW activation period (30 seconds here) are 87% for 62.5 MHz and 193% for 75 MHz, respectively.

IV. Capturing efficiency evaluation

To evaluate system performance at capturing of nanoparticles, the intensity of fluorescent nanoparticles at the downstream were integrated over the selected area. Upon activating the SAW and after the transient time, the intensity level is stabilised and steady for optimised frequencies. Ideally, if all nanoparticles are trapped at the upstream, the grayscale intensity of light at the downstream should be zero, equivalent to pure black(Fig. S5). The difference of the area between actual intensity level to the black reference line can represent the fraction of passed particles. However, as it can be seen from Fig. S5b, the grayscale intensity level even at the locations that there is no particle (outside the channel for example) is not zero. This background intensity, possibly due

to the reflection and refraction of fluorescent light into the PDMS, is set as the threshold. Thus, the efficiency is calculated as the ratio of the area highlighted as captured to the total area of the rectangle below the initial level and this background intensity threshold.

References

[1] R. Habibi, C. Devendran and A. Neild, *Lab Chip*, 2017, **17**, 3279–3290.

[2] L. Gor'Kov, Soviet Physics Doklady, 1962, p. 773.

[3] P. B. Muller, R. Barnkob, M. J. H. Jensen and H. Bruus, *Lab Chip*, 2012, **12**, 4617–4627.

[4] P. Mott, J. Dorgan and C. Roland, *Journal of Sound and Vibration*, 2008, **312**, 572 – 575.

[5] R. Kono, *Journal of the Physical Society of Japan*, 1960, **15**, 718–725.

4

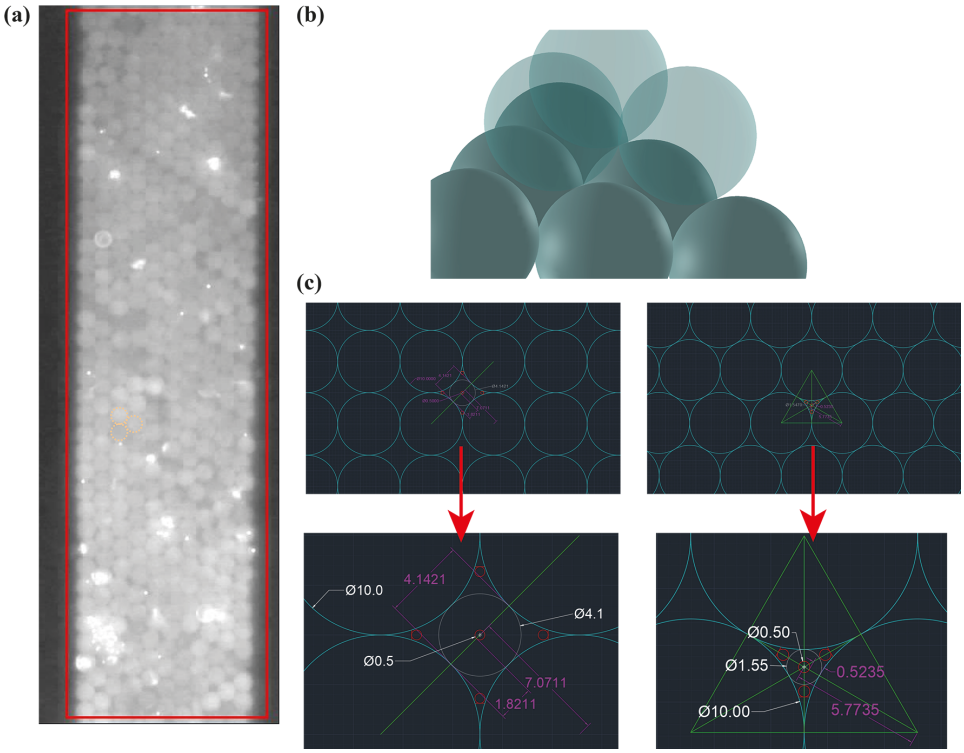

Fig. S1: *(a)Caption of the packed bed at a relatively higher magnification shows that beads are well packed in a honeycomb-like pattern (the ideal packing scenario) (b) Spheres in an ideal packed scenario and their cross section in different planes (c) where provide largest (left) and narrowest (right) passage for red nanoparticles. Dimensions are in micrometer. The 'pore' size is about 41% of the microparticle (MP) diameter and the passage between spheres are about 15.5% of the MP's size. That brings the gap between MP and NP down to 500 nm. In this work it is about 1/50 of the wavelength.*

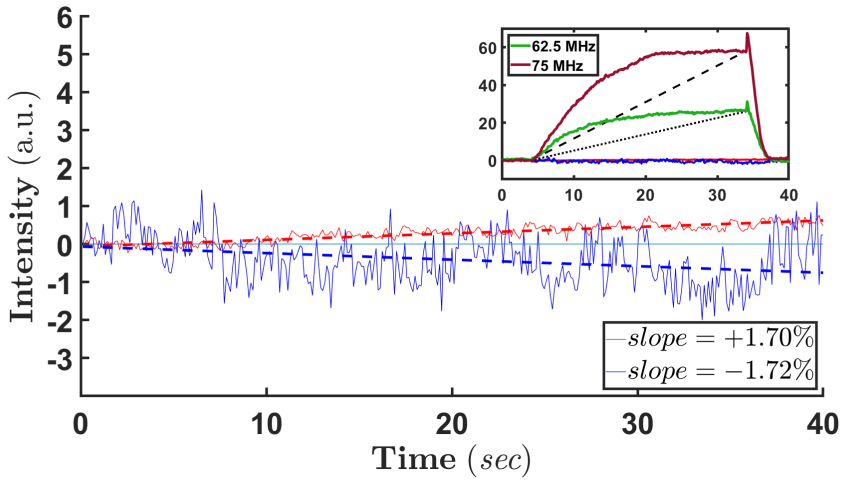

Fig. S2: *Instantaneous intensity level at the upstream of the channel (width 94 μm)* ***without*** *activating the SAW, at two extreme cases that have the highest average linear intensity growth (both ascending and descending). When compared with intensity level growths by energised SAW (here are shown for 2 different frequencies of 62.5 and 75 MHz activated for 30 seconds in the inset), the intensity change due to hydrodynamic effects is insignificant and thus negligible.*

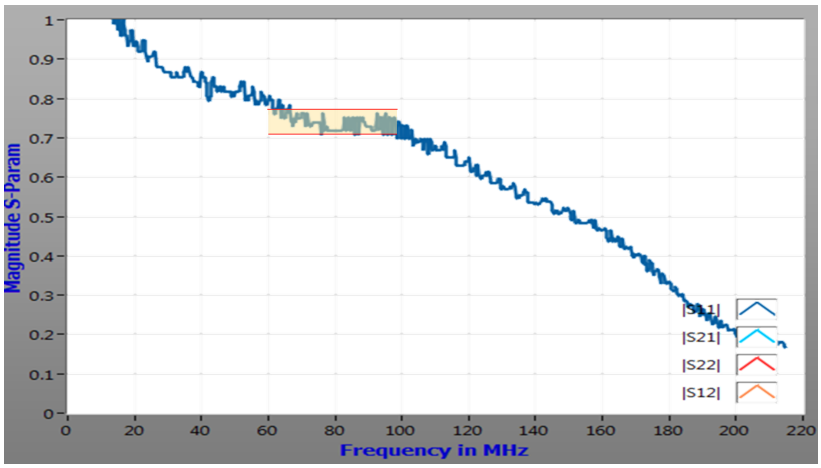

Fig. S3: *The |S11| parameter of the IDT, that was used in the frequency characterisation, is nearly constant with no significant change within the range of 60 - 90 MHz. This asserts that the optimum frequencies, where the nanoparticle collection is higher, depend on the physics of the interaction between nanoparticles and the microparticles of the packed bed rather than the chirped IDT's response. S11 parameter is obtained using PowerSAW F-20 (BelektroniG, Germany) signal generator.*

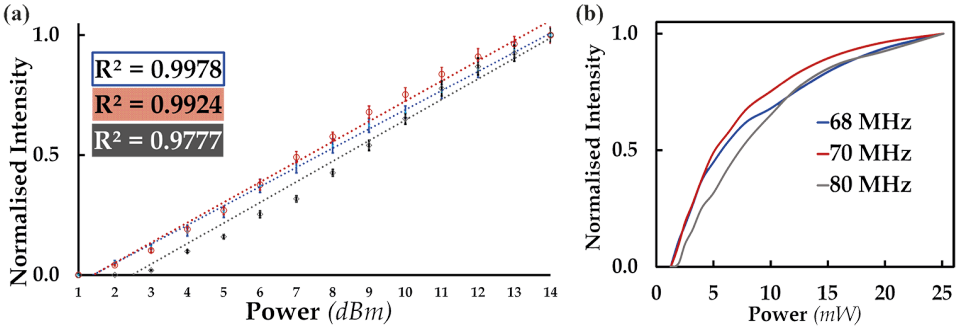

Fig. S4: ***(a)*** *The normalised intensity gains at different frequencies show linear compliance with power level in dBm (with R^2 shown and linear regression p-value is <0.001 for three data sets), thus a (b) logarithmic leaning against power levels in mW.*

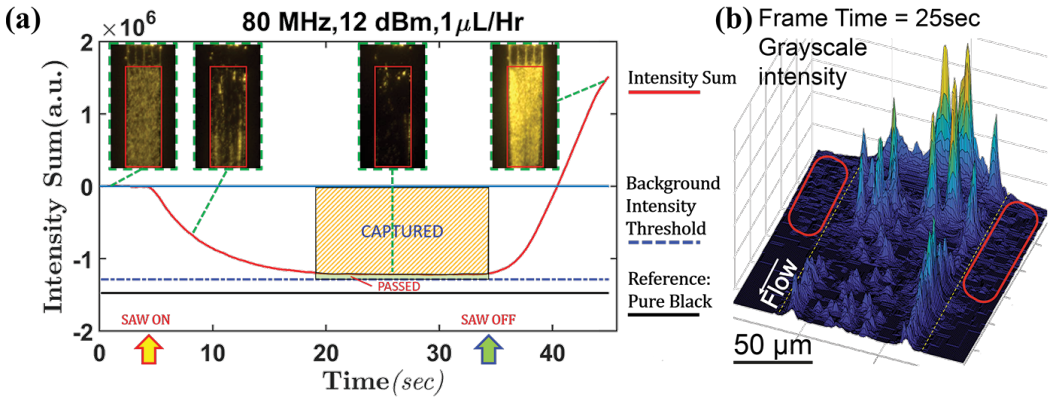

Fig. S5: *(a)Integrated intensity of the selected region at the downstream were considered to represent the population of passed nanoparticles. After the intensity stabilised, the differenced of intensity with the initial level shows the fraction that captured. (b)The background area is not zero (pure black) even at locations that no fluorescent nanoparticle is present such as outside of the channel. This intensity is defined as the threshold instead of the black background reference.*

Chapter 5

Submicron biological particle trapping and enrichment using a Sound Wave Activated Nano-sieve (SWANS)

5.1 Overview

The previous chapter established a platform for nanoparticle trapping and enrichment system that utilised a mechanically activated packed bed of microparticles; which its trapping mechanisms is independent of channel geometries hence has the potential to be further upscaled to a high-throughput technique. As previously discussed in Chapter 4, increasing the device flow rates will weaken the capturing efficiency due to increase in the drag force. Conversely, enlarging the channel size can help to reduce the drag force in the favour of the Bjerknes forces. However, increasing the size of the channel can lead to a longer packed bed and thus, to a higher hydrodynamic resistance. This challenge can be addressed by incorporating larger beads into the packed bed as the hydraulic pressure will reduce linearly with particle size.

This chapter investigates the effects that using larger beads has on the capturing efficiency. In an ideal dense packing of equal spheres, such as face-centred cubic (fcc) or hexagonal close-packed (hcp), the size of the smallest pore between beads scales linearly with the size of the beads. The effects of changing the bead material were also investigated; a material that has a higher sound wave scattering at resonance frequencies would increase the capturing efficiency. The theoretical model was expanded to include travelling waves to try and predict the appearance of new peaks and a wider frequency range was also incorporated. Polystyrene particles of three different sizes (7, 10 and 15 μm) along with polymethyl methacrylate (PMMA) and silica glass particles with a diameter of 10 um were used in this study. Computational numerical simulations and a systematic comparison method that includes all peak frequencies from standing and travelling wave scenarios, predict that bigger particles (15 μm) and softer polymeric materials (PMMA and PS) generate higher attraction forces. Further

experimental evaluations have verified and confirmed these findings.

The following chapter also demonstrates the capacity of the SWANS system to successfully capture exosomes (with mean size of 167 nm), although they are much softer compared to PS nanoparticles, making them harder to capture. Exosomes, like other submicron bioparticles such as bacteria, viruses and other EVs, have soft lipid-based membranes. Transmission electron microscopy (TEM) images of liposome samples (another EV particle) shows that their membranes retain their structure and spherical morphology even after going through the sound-activated packed bed of resonant particles. This ensures the biocompatibility of SWANS and a closer step toward large-scale purification system.

5.2 Publication

The following publication was reproduced from [3] with kind permission from the Royal Society of Chemistry.

Lab on a Chip

ROYAL SOCIETY OF CHEMISTRY

PAPER

View Article Online
View Journal

Cite this: DOI: 10.1039/d0lc00623h

Exosome trapping and enrichment using a sound wave activated nano-sieve (SWANS)†

Ruhollah Habibi, [a] Vincent He, [a] Sara Ghavamian, [b] Alex de Marco, [cd] Tzong-Hsien Lee,[d] Marie-Isabel Aguilar, [d] Dandan Zhu, [ef] Rebecca Lim [ef] and Adrian Neild *[a]

Received 17th June 2020,
Accepted 28th August 2020

DOI: 10.1039/d0lc00623h

rsc.li/loc

Exosomes, a form of extracellular vesicle, are an important precursor in regenerative medicine. Microfluidic methods exist to capture these sub-micrometer sized objects from small quantities of sample, ideal for multiple diagnostic applications. To address the challenge of extraction from large volumes, we use the visual access offered by microfluidic techniques to probe the physical mechanisms behind a method which is compatible with future upscaling. The sound wave actuated nano-sieve uses resonant modes in a packed bed of microparticles to exert trapping forces on nanoparticles. Here, we examine the role of the microparticle size, demonstrating better performance from 15 μm particles than 7 μm particles. When applied to biological samples, we demonstrate for the first time that a packed bed of these larger particles is capable of capturing exosomes and liposomes, the captured particles being on average 20 to 40 times smaller than the pores within the trapped bed.

1 Introduction

Surface acoustic waves offer three mechanisms with which to interact with fluid suspensions within an enclosed microfluidic system. Acoustic streaming acts on the fluid itself, causing a bulk, steady state flow.[1] Acoustic radiation forces arise due to gradients within the sound field and act on suspended particles.[2–4] Whilst, Bjerknes secondary force is an interparticle force which arises from the interaction of a wave scattered by one particle impinging on another.[5,6] Acoustic manipulation in microfluidics has been widely applied to micron-sized particles,[7,8] including cells,[9,10] for application such as separation,[11,12] sorting[13,14] or mixing.[15–17] However, as the size of particle decreases scaling laws dictate that drag forces induced by acoustic streaming become more significant than acoustic radiation forces.[18–20] As such the use of acoustic radiation forces to capture nano-scale particles is highly problematic, instead these particles tend to follow the swirling streaming flows.[21]

However, there are numerous biological applications which require the trapping and retention of nanoparticles for detection, diagnosis or as a precursor to other processes.[22–28] These include the detection of *E. coli* bacteria[29,30] and viruses[31] in drinking or sewage water,[32,33] and the capture of exosomes. Exosomes are extracellular vesicles (EVs) of between 30–200 nm diameter, they act as biomarkers for diagnosis of diseases[34] and play an important role in regenerative medicine.[35,36] For diagnosis, exosomes need to be detected from small volumes of bodily fluids[37] such as blood plasma, whilst for regenerative medicine, much larger volumes need to be processed to maximise the total yield of the harvest.[38–40]

Ultra-centrifugation or ultra-filtration offer a method to tackle nanoparticle collection from moderate fluid volumes, but are time-consuming, and, in some cases, damaging to the structural integrity of bioparticles.[41–43] Microfluidic approaches have been used to isolate exosomes from samples containing a mix of components. This is achieved by capture of larger components, whilst exosomes pass through the system largely unaffected.[44,45] The collection of exosomes for diagnostics has been achieved, but most methods used are incompatible with upscaling to the application of exosome harvesting.[46,47] For example, due to the operation being linked to channel dimensions.[37] However, the sound wave

[a] *Laboratory for Micro Systems, Department of Mechanical and Aerospace Engineering, Monash University, Clayton, Victoria – Australia. E-mail: adrian.neild@monash.edu*
[b] *Applied Micro and Nano Technology Lab, Department of Mechanical and Aerospace Engineering, Monash University, Clayton, Victoria – Australia*
[c] *ARC Centre of Excellence in Advanced Molecular Biology, Monash University, Clayton, Victoria – Australia*
[d] *Department of Biochemistry and Molecular Biology, Monash University, Clayton, Victoria – Australia*
[e] *Hudson Institute of Medical Research, Melbourne, Victoria – Australia*
[f] *Department of Obstetrics and Gynaecology, Monash University, Melbourne, Victoria – Australia*

† Electronic supplementary information (ESI) available. See DOI: 10.1039/d0lc00623h

View Article Online
Paper Lab on a Chip

activated nano-sieve (SWANS),[48] which uses acoustic actuation in a manner which is independent of channel geometry (the operation frequency is dictated by the size of the particles constituting the packed bed rather than a channel resonance), and so can potentially be upscaled. Here, a packed bed of microbeads are excited with ultrasound. These vibrating microbeads create an interparticle, Bjerknes, force which acts on nanoparticles as they travel through the packed bed. In addition, the highly confined fluid volumes found within the bed can be expected to change the role of acoustic streaming. This results in the capture of copolymer 100 nm nanoparticles within the bed.[48]

In order to translate the use of SWANS to the capture of exosomes from large fluid volumes, the channel size independence of operation must be exploited to obtain higher throughput and capture performance must be improved such that biological particles can be concentrated. In this work, we directly address the latter challenge in a manner which will assist future efforts to address the former point. We examine the performance of the packed bed as a function of the size and material of the beads used to construct it. The use of larger beads in the bed reduces the pressure head at higher flow rates,[49,50] and lowers the frequency of operation, both of which will aid future upscaling of the system, however, here our focus is to show that through an increase in the size of these beads, the capture efficiency can be improved, and that using this improved efficiency the system is capable of capture of exosomes.

2 Materials and methods

A schematic of the system is shown in Fig. 1A. It consists of a channel across which a row of pillars creates a physical barrier. This barrier impedes the flow of microparticles (MPs), such that a packed bed is created. Two sets of electrodes deposited on a piezoelectric substrate form a pair of interdigital transducers (IDTs), capable of creating counter-propagating surface acoustic waves. These surface waves couple into the fluid within the channel and vibrate the beads in the packed bed, operation is most efficient when the beads are excited at a resonance frequency. Fig. 1B shows the operating sequence, the use of fluorescent nanoparticles (NPs) allows the change of light intensity to be used to measure trapping and release.

2.1 Simulation

The packed bed is formed when a row of pillars across the microchannel impede the flow of microparticles. The stacking arrangement of the spherical beads packed under a pressure head is face-centred cubic (FCC) or hexagonal closed-packed (HCC) (Fig. 2A). In this dense packing scenario, nanoparticles can only pass through the pores between the spheres. With the pore size being dictated by the microbead diameter, it is the forces acting on nanoparticles within these pores which is modelled, (Fig. 2B and S1†). By calculating the forces acting on a nanoparticle in a pore between three microparticles, we capture both the effect of microparticle size on the size of the pore and the magnitude of the acoustic forces.

Upon actuation, surface acoustic waves (SAW) propagate along the surface of the substrate. When they reach the fluid filled channel, the wave couples into the liquid domain at the Rayleigh angle.[51] This coupling of energy causes the SAW to diminish in strength. The use of two counter propagating waves means that at the location equidistant from the two IDTs a pure standing surface wave exists. However, as each

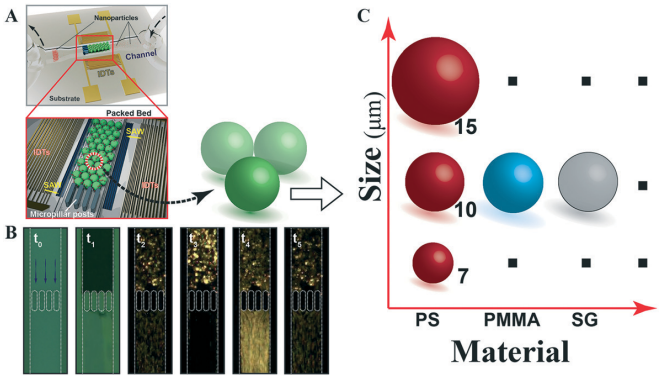

Fig. 1 (A) A schematic of the sound wave activated nano-sieve (SWANS) that uses a SAW excited packed bed of microparticles to trap nanoparticles. (B) A sequence of images which show the empty channel (t_0), the packed bed formed by the microparticles' inability to pass between the gaps between a row of micropillars (t_1). With the bed prepared, a solution of fluorescent nanoparticles is passed through the bed (t_2) with the SAW activated the fluorescent intensity drops downstream of the pillars as the nanoparticles are trapped within the bed (t_3), subsequently when the SAW is deactivated the enriched and highly concentrated batch of nanoparticles is released downstream (t_4). The fluorescent intensity reverts to its initial level when the concentrated batch leaves the pack bed and pillars downstream (t_5) (see Fig. S2A† for intensity measurement). (C) A range of size and material of microparticles are examined, to better understand the scaling of the mechanics behind the SWANS, with a view to using these findings to improve performance to enable biological particle capture and for future upscaling of the system.

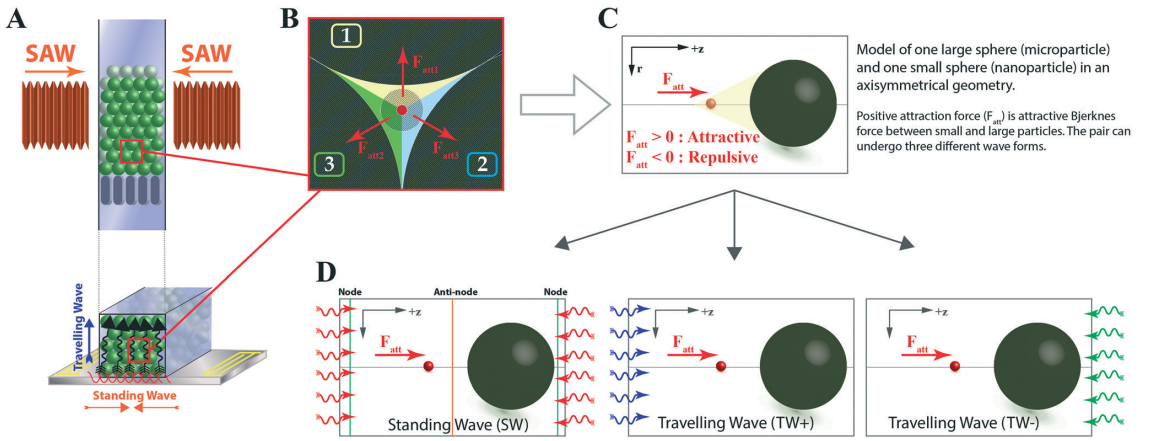

Fig. 2 (A) A schematic of the channel (note that in the experimental system the bed is two particles high) showing two superposed surface acoustic waves (SAW) generate a standing wave on the surface of the substrate while leaking to the fluid in Rayleigh angle. The result is a complex mix of standing wave and travelling wave components in the channel. Standing wave components are primarily in planes parallel to the substrate, as coupled waves counter propagate and interfere, whilst travelling components are primarily in the normal direction due to the Rayleigh angle of emergence of the coupled waves. (B) Before excitation, nanoparticles pass through the pores between densely packed adjacent particles, the central location of the pore is an unstable equilibrium. For an ideal dense packing, the nanoparticle pass through pores between three particles in the horizontal, vertical or diagonal planes. (C) As Bjerknes force scales with the gap between two particles, the attraction force of the nearest micro particle is most significant, so it is this interaction which is modelled. (D) Three excitation scenarios are used, to capture the complex wave field within the channel, these are a standing wave, and two travelling waves (in the $+z$ direction or and $-z$ direction).

SAW attenuates exponentially as it passes under the fluid, at locations closer to one IDT set than the other, the amplitude of the counter propagating waves differ, so the resultant interference pattern has both standing and travelling wave components.[52] In addition as the coupled wave propagates up through the fluid, it will encounter the PDMS roof of the channel, and undergo only weak reflection, hence there is also a mixed standing and travelling wave in the vertical direction.[53] The sound field is further complicated by the inclusion of the microparticle spheres, whose whole purpose is to scatter waves in order to generate interparticle forces with the passing nanoparticles. As a result, we model a highly simplified aspect of the system, identified to allow understanding of the underlying physical effects.

Fig. 2A depicts the mechanically actuated packed bed. The packing of the beads creates a small pore through which the nanoparticles flow (Fig. 2B). The waves scattered by the beads create a Bjerknes force acting on the nanoparticle. Each pore will have a different ultrasonic exposure and each nanoparticle will take a different route through the network of pores, so rather than attempt to model the whole system, we identify what is key to successful operation and simplify accordingly. Specifically, we aim to examine the link between frequency and capture force magnitude, how this varies with microparticle size and type, and what role standing and travelling wave components play in the frequency response of the system. The system is therefore restricted to the study of only these aspects.

Each microparticle will induce a Bjerknes force on a nanoparticle (Fig. 2B). Each nanoparticle will take its own convoluted course through the network of pores, and in doing so, it will spend some time in closer proximity to one microparticle than the other two forming the pore. As the Bjerknes force scales with the inverse of distance to the higher powers ($F_{att} \propto 1/d^n$, $n > 1$),[54] the Bjerknes force from the closest microparticle will be most significant. As such we model a single microparticle in proximity to a single nanoparticle (Fig. 2C). The microparticle is varied over a defined range to study the role of this parameter on the Bjerknes force exerted, however, this will also alter the pore size. To capture this, the separation between microparticle and nanoparticle is scaled accordingly (Fig. S1†). For 10 μm particles, the centre to centre spacing was set at 5750 nm (this sets the nanoparticle at the centre of the pore), whilst for 7 μm and 15 μm, this distance scales linearly to become 4050 nm and 8650 nm, respectively. To capture the variations in acoustic excitation due to spatial changes in the degree of standing and travelling wave exposure, the pair of particles is exposed to three different incoming waves, Fig. 2D, a standing wave and a travelling wave propagating in two directions. Again, this will not capture every conceivable excitation type, but it will give the trends as a function of frequency, as required for effective operation. An axisymmetric model of the two spheres was built in COMSOL Multiphysics 5.1 using the Acoustic module. More details of the simulation implementation can be found in the ESI† (Tables S1 and S2).

2.2 Device fabrication

To accommodate a uniform and dense packed bed in the channels for each MP size, we select a channel height scaled to be slightly over two microbead diameters, 14.8 μm for 7

micron polystyrene MPs (Magsphere, USA), between 20.5–21.5 μm for 10 micron polystyrene (Magsphere, USA), PMMA (Phosphorex, USA) and silica glass (EPRUI, China) MPs and 32.5 μm for the 15 micron polystyrene particles (Phosphorex, USA). The microchannels were fabricated from PDMS by soft lithography using a silicon mould. The mould was fabricated by UV lithography, followed by Cr deposition and DRIE (deep reactive ion etching). The cast PDMS was bonded to piezoelectric chips using plasma treatment (Harrick Plasma, PDC-32G). These piezoelectric chips were patterned with IDTs and diced from a lithium niobate ($LiNbO_3$, LN) wafer (128° *Y*-cut). The IDT patterning was achieved using UV lithography, and E-beam evaporation deposition (5 nm-thick Cr primer layer, 190 nm-thick Al conductive layer and 5 nm-thick Au corrosion protective layer) followed by lift-off. An extra 250 nm layer of SiO_2 was used to cover the IDTs to provide corrosion protection and stronger bonding. We used chirped IDTs so that a wide range of frequencies could be used to excite the packed bed. Three different SAW wavelength (λ_{SAW}) ranges were used: 14–60 μm, 20–70 μm and 40–120 μm, in each case the IDT fingers were aligned at 45° to the *x*-propagation direction were used. To evaluate the frequency response and capturing efficiency of ultrasonically activated packed beds, 500 nm red fluorescent polystyrene nanoparticles (Magsphere, USA) were used.

2.3 Exosome sample

Isolation of human amnion epithelial cell-derived extracellular vesicles (hAEC-EVs). Human amnion epithelial cells (hAECs) were cultured at a concentration of 0.4 million per mL in serum free media (UltraCULTURE, LONZA) for four days at 37 °C, 95% humidified air and 5% CO_2. Conditioned media were collected and put through a tangential flow filtration system (AKTAcrossflow, GE Healthcare). Condition media were passed through a 0.2 μm pore size column and then a 500 kDa pore size column to exclude the particles that larger than 0.2 μm and smaller than 500 kDa. Then the conditioned media was concentrated to 1/10th of its original volume and washed with PBS repeatedly prior to assessment and characterisation.

hAEC-EV characterisation with transmission electron microscopy analysis (TEM). Isolated EVs were resuspended 1 : 1 with 4% of PFA. Then 5 μL of the EV suspension was placed on a Formvar–carbon coated electron microscope (EM) grid and then fixed with 1% glutaraldehyde. After 5 washes in distilled water, the grid was soaked in 4% uranyl-oxalate solution (UOA) for 5 minutes and then in methylose cellulose for another 5 minutes before it was dried for imaging. The images were taken using a H75000 transmission electron microscope (Hitachi, Japan) at 70 kV. The EVs used for this project are of typical exosome shape, bearing a distinct cup-shaped morphology (see Fig. S3A in the ESI†).

hAEC-EV characterisation with nanoparticle tracking analysis (NTA). EV samples were assessed using a NanoSight NS300 system (NanoSight technology, Malvern, UK) coupled with a 405 nm laser. EV sample was diluted to 4 μg mL^{-1} in MilliQ water and was injected into a flow-cell top plate by a syringe pump. Three videos (60 s per video) were recorded, merged, and analysed using the proprietary software (Build 3.1.45). The particle concentration of the EV sample was 4.5×10^{10} per mL. The particle size distribution was D10 67 nm, D50 109 nm and D90 300.5 nm with mean size of 167.3 nm (see Fig. S3B in the ESI†).

Prior to the trapping experiment with SWANS, the exosome sample was diluted in phosphate-buffered saline (PBS) buffer and labelled using ExoGlow protein labelling kit (EXOGP100A-1, Systems Biosciences – USA).

2.4 Liposome sample

Preparation. POPE, POPG, cardiolipin (TOCL) were dissolved in chloroform to 2 mM as lipid stock solutions. Dried lipid films were prepared by adding 500 μL lipid solutions in a volume ratio of POPF : POPG : TOCL = 70 : 25 : 5 to the bottom of clean, dried glass test tubes. The organic solvent was evaporated with a gentle stream of dried N_2 at 40 °C. The lipid films were further dried under high vacuum for 16 h to completely remove the residual organic solvent. The dried lipid films were flushed with argon gas, sealed and kept at −78 °C till use. For the liposome preparation, 10 mM HEPES, 150 mM NaCl, pH 7.2 (HBS) was used to hydrate the lipid films at a final concentration of 1 mg mL^{-1} with constant vortex at high speed for 5 min. The liposome solutions were incubated at 37 °C for 1 hour with shaking at 120 rpm min^{-1}, followed by bath-sonication for 30 min till full transparency. To make the liposome homogeneous in size, the clear liposome-HBS solutions were pass through a polycarbonate membrane (ATA Scientific, Lucas Heights, NSW, Australia) with 100 nm pore diameter 31 times with AVESTIN Liposofast extruder (Avestin, ON, Canada).

Dynamic light scattering. The hydrodynamic diameter of the liposomes was measured at 25 °C in HEPES buffer using a Zetasizer NanoZS (Malvern Instruments, Worcestershire, UK) collecting the scattering light at an angle of 173° at a wavelength of 633 nm using a 5 mW He–Ne laser. The mean diameter of liposomes to the light intensity was calculated using the Stoke–Einstein relation for spherical particles. The refractive index (RI) of HEPES buffer was 1.3345 and the viscosity of the buffer was 1.003 mPa·s at 25 °C. The mean diameters of liposomes 75.75 nm (peak at 107 nm).

Liposome characterisation with transmission electron microscopy analysis (TEM). Liposomes-containing solution was vitrified by plunge freezing using a ThermoFisher Vitrobot. 3 μL of solution were deposited on Quantifoil 300-mesh R2/2 EM grids that were glow discharged for 45 seconds. TEM imaging was performed on a ThermoFisher Arctica operated at 200 keV and images were acquired on a ThermoFisher Falcon 2 Direct Electron Detector. Imaging was performed in nanoprobe mode with the illumination set to be parallel and at nominal magnification comprised between 6500× and 36 000×. Images were acquired at a negative 3 μm

View Article Online
Lab on a Chip Paper

focus in movie mode with a maximum total electron dose of 20 $e^-/Å^2$ applied to the sample.

2.5 Experiment setup and data analysis

Prior to each experiment solid particles were suspended in a water solution with 2% polyethylene glycol (to reduce attachment of particles to the channel walls), the suspension was shaken by a vortex mixer prior to being injected into the microchannel using a syringe pump (KD Scientific). SAW was excited by application of an oscillating electrical signal to the IDTs, this was emitted by SMC100A signal generator (Rhode & Schwarz, Germany) and amplified (Amplifier Research 25A250A) prior to application to the IDTs by use of SMA cables and spring loaded pins held in a custom 3D printed jig.

Images were taken using a Pixelink digital camera (PL-B782CU) top mounted on an upright microscope (BX43, Olympus). Fluorescent light filters (Edmund Optics, USA) were used to cover the fluorescent light wavelength of the target particles (PS nanoparticles and labelled exosomes): excitation at 532–554 nm and emission at 576–596 nm. A MATLAB® script was used to trigger ultrasonic excitation signal and the commencement of video capturing. The images were subsequently analysed based on the fluorescent light intensity at locations up and downstream from the micropillars (further details are provided in Fig. S2†).

3 Results and discussion

3.1 Frequency response of sizes and materials: evaluation of expanded model

In order to efficiently capture nanoparticles in the mechanically activated packed bed the optimum frequency must be selected, previously we studied this for a single microbead size and assumed pure standing wave excitation.[6,48] Here, we examine the effect of bead material and size, and include a more diverse set of excitation conditions to better represent the experimental system. In each case we are interested in the peak force amplitude, we note that due to the complexity and variation in the sound field the ratio of travelling to standing wave components in the excitation will vary spatially across the packed bed.

For standing wave excitation of the polystyrene (PS) particles, the peak attractive force occurs at two frequencies (within the range considered) (f_1^*) at $d/\lambda \approx 0.44$ and (f_2^*) at $d/\lambda \approx 0.57$.[6,48] It can be seen from Fig. 3A for 7 μm PS particle, these peaks are at approximately 94 and 123 MHz, respectively, whilst for 10 μm, they are at 66 MHz and 87 MHz (Fig. 3B). For the size of 15 μm, the first two peaks occur at 44 and 58 MHz. In addition the range is sufficient that a third standing wave induced peak can be seen (Fig. 3C) at 81 MHz ($d/\lambda \approx 0.81$). Such higher peaks can be expected for all particle sizes, however, in most cases we limited the simulation study up to $d/\lambda \approx 0.7$ to be in line with the experimental frequency range. A key trend for this excitation mode is that the force

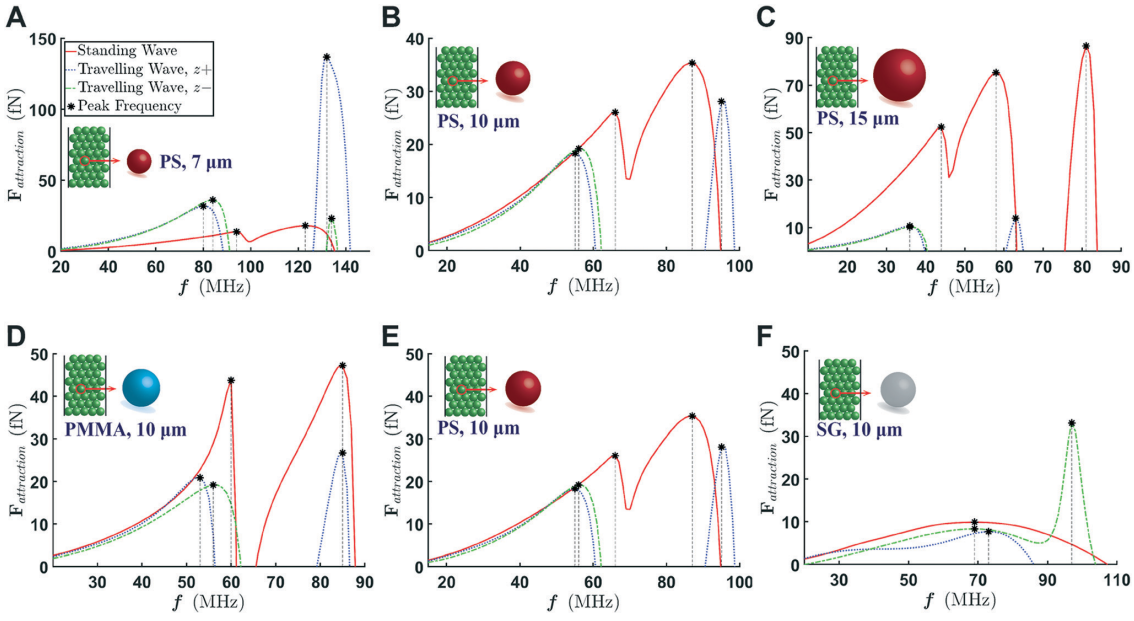

Fig. 3 Simulation results for the attraction force between a 500 nm polystyrene nanoparticle and a microparticle (MP), in (A)–(C) the MP is polystyrene of a diameter of 7 μm, 10 μm and 15 μm, respectively. For (D)–(F) the MP is 10 μm, with the material being poly(methyl methacrylate) (PMMA), polystyrene (PS) and silica glass (SG), respectively. In each case, the peak frequencies from travelling waves in positive or negative directions overlap whenever peaks from both wave types appear. The legend shown in (A) is the same for all the plots.

amplitude increases with microparticle size. It was expected that the Bjerknes force would increase with the size of the scatterer, but it is interesting to see this effect dominates over the effect of the interparticle spacing being scaled with scatter size (Fig. S1 in the ESI†).

The addition of travelling wave excitation to the study (Fig. 2D), yields additional frequencies at which peaks in the force occur. Whilst the natural/resonance frequencies of the microbeads are not excitation type dependant, it can be seen that the magnitude of the attraction force is. For example in the case of 7 μm PS microparticle under travelling wave in $+z$ direction (TW+), the first and second peaks of the attraction force are at 80 and 132 MHz, clearly distinct from their standing wave counterparts. It can also be seen that the direction of the travelling wave can make modest changes to the peak frequencies. Again, for 7 μm PS microbead under travelling wave in $-z$ direction (TW−) these frequencies are respectively, 84 and 134 MHz. However, the shift from TW+ is not significant. Two other trends can be seen from the travelling wave excitation. Firstly, the higher frequency peaks which occur for the positive travelling wave often disappear for the negative travelling waves. Presumably because the shorter wavelength causes diffraction around the bead to be less pronounced and hence the beads casts a greater ultrasonic shadow onto the nanoparticle at these higher frequencies. Secondly, as the particle size increases this excitation mode becomes less significant, here the scaled spacing has a more significant effect than the increased size of the scatterer. In terms of material, the simulation shows a modest amplitude difference between PS and PMMA, and a substantial drop, especially in the standing wave component for the much stiffer SG (Fig. 3D–F), this despite the increased scattering that can be expected due to the higher acoustic impedance contrast with the fluid medium. This could be as polymer-based beads undergo extreme resonance effects and volume deflection, thus create more wave scattering, which in consequence, generate larger Bjerknes forces. Fig. 4A shows a direct comparison of the scale of the forces arising from each excitation type for each scatterer considered (this data is tabulated in Table S1 in the ESI†).

With the simulations showing that for standing wave excitation the Bjerknes force on a nanoparticle at a scaled spacing is increased with scatter size, and the converse trend is seen for travelling waves, we turn to the experimental data, which focusses on the capture of the nanoparticles across the ensemble of conditions which apply in the full bed. The sound wave activated nano-sieve (SWANS) were tested for these different microbead sizes. So, in a channel of 94 μm × 14.8 μm a packed bed of 7 μm particles was formed. The channel height of 14.8 allows to have 2 layers of randomly packed microbeads, though upon the excitation of the sound wave, the bed reforms itself to an arrangement of FCC or HCC packing. Similarly, the selected channel height allow a 2-layer packed bed to be formed for the other particle sizes.

In the case of 10 μm PS microbeads, our previous numerical work, which only considered SW wave scenario,

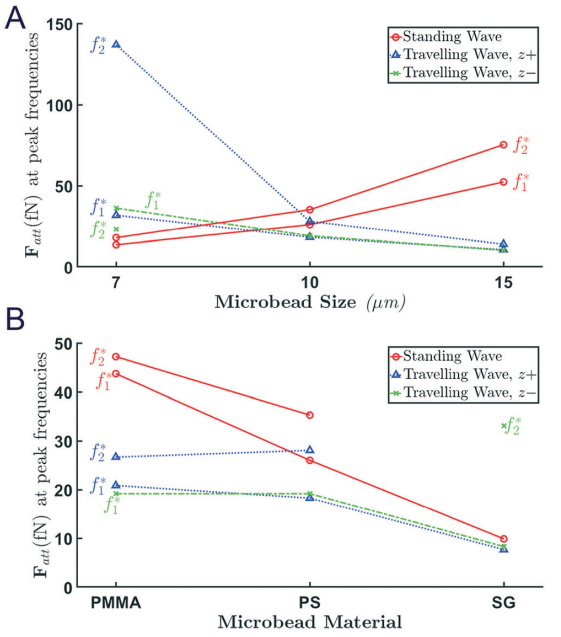

Fig. 4 A comparison of the attraction force between MP–NP at each peak frequency between different sizes and materials is shown, this indicates the highest attraction forces which are predicted. (A) F_{att} at peak frequencies for three difference size of microbeads in the packed bed. Comparing the peak forces from standing wave frequencies shows larger sizes can perform better in NP trapping, whilst if travelling wave components were to be present smaller MPs are predicted to generate larger attraction forces. (B) For the three materials investigated, for standing wave components PMMA outperforms both PS and SG, whilst for travelling wave components, the attraction force of PMMA and PS at their corresponding peak frequencies are not significantly different. SG does not show a second peak in SW and TW+ scenarios, however, a second peak of TW− does occur.

two peaks were predicted within the range of 60 to 90 MHz. With the inclusion of travelling wave excitation, another two peaks, are predicted (55 and 95 MHz). Experimental testing over a range of 51 to 100 MHz confirms peaks from both types of excitation (Fig. 5). There is a clear increase in the fluorescent light intensity level within the packed bed area, indicating the entrapment of 500 nm red fluorescent polystyrene particles, at 56–58 MHz, 68–72 MHz, 76–80 MHz and 84–86 MHz.

Clearly, the travelling wave excitation modes exist and result in peaks in the intensity plots representing particle capture. In Fig. 4, these modes are predicted to be very important in the case of smaller beads, and much less so for larger ones. However, the complexity of the spread of different types of acoustic fields across the full channel is not captured in the model, so nor is the relative degree of importance of these modes. To understand that, it is necessary to examine the case of the 7 um particles, to see if the very strong travelling wave peaks result in high nanoparticle capture rates. We further discuss the

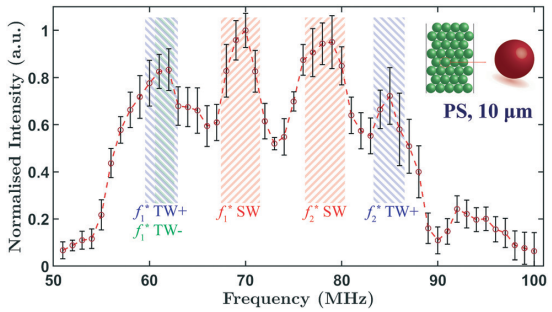

Fig. 5 Experimental results of the fluorescent intensity changes, detected downstream of the micropillars, shows the capture of 500 nm PS nanoparticles at different frequencies within a range of 50–100 MHz, for a bed of 10 μm PS particles. Four distinct peak frequencies can be observed. The central two relate to frequencies predicted for standing wave excitation, the lowest frequency peak (62 MHz) can be attributed to a travelling wave component excitation (either both positive or negative propagation direction) and the fourth peak (85 MHz) relates to the second TW+ peak. The error bars indicate standard error.

experimental results of other materials frequency response in the ESI,† where we can see similar trends with simulation prediction can be observed.

The key feature of the 7 μm and 15 μm packed bed simulation data is that for the smaller beads the travelling components dominate, and in contrast standing wave excitation is dominant for the larger beads. The experimental results for the 7 μm particle (Fig. 6A) shows six peaks, those at 70 and 80 MHz align with the lower travelling wave prediction, the peaks at 85 and 122 MHz aligns with a standing wave frequencies prediction, and those at 129 to 135 MHz are aligned with the higher travelling waves prediction. It is clear from the experimental data that travelling wave excitation must be considered in order to explain all the peaks. However it is noteworthy, that the model, which simply uses an equal amplitude excitation for the travelling and standing waves, overestimates the importance of the former. This bias in the experimental data is also seen in the case of 15 μm PS (Fig. 6B). Here, three peaks in the experimental align with frequencies predicted by the standing wave model (41 ± 2 MHz, 49 ± 2 MHz and 72–76 MHz), whilst the peaks expected due to TW excitation are significantly weaker.

In conclusion, the experimental data shows that the predicted peaks for travelling wave exposure do occur, but they are not as strong as the modelling data suggests. The most important example of this is the second peak frequency of TW+ for 7 μm, for which a high attraction force is predicted, but results in a much weaker peak in the experimental intensity data. This suggests that the overall acoustic field in the packed bed is dominated by standing wave components in its excitation. It is worth noting, that the numerical (Fig. 3D–F) and experimental data for the other microparticle materials (Fig. S4†) also showed a dominance of the standing wave frequencies for PMMA and importance

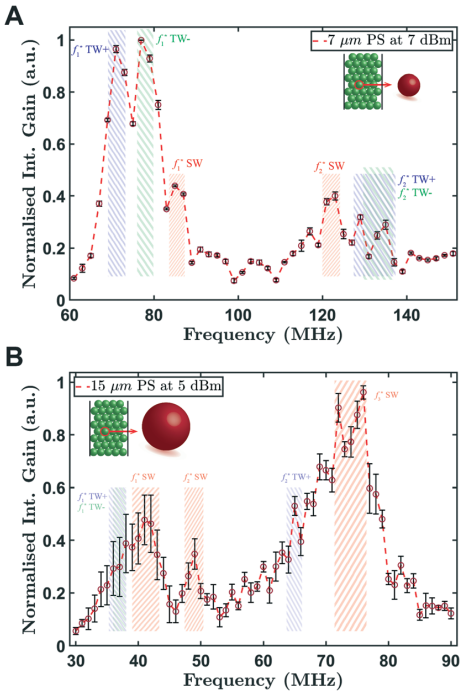

Fig. 6 Experimental results of the fluorescent intensity change shows the capture of 500 nm PS, detected downstream of the packed bed made of (A) 7 μm and (B) 15 μm polystyrene microparticles. For the packed bed of 7 μm particles, two pronounced peaks within the range of 70–80 MHz (first TW peaks), and other smaller peaks at 85–87 MHz (first SW peak) and within the range of 120–140 MHz (second SW and TW peaks) can be observed. The capturing of second TW+ peak is not as high as expected. For the case of 15 μm particles, three distinct peaks are observed at around 40, 50 and 70–80 MHz. For larger beads, SW peaks manifest themselves well while in comparison TW peaks are apparently weak. The error bars indicate standard error.

of travelling wave for SG, however not as significant as expected (see Fig. 4B).

The combination of the simulation data, understood in the context of the frequency sweep experimental data, allows the selection of preferred operating frequencies, and the understanding of which bed material and size is likely to yield the best collection efficiency. To finalise this study, we now study this efficiency directly.

3.2 Efficiency comparison

To directly compare the effect of the packed bed's microbead size, we evaluate the capturing efficiency of the system at each of the identified peak activation frequencies. To assess this the intensity level was measured downstream of the packed bed, during actuation, and the degree of reduction in nanoparticles emerging from the bed used to assess capture within it. Unsurprisingly the capturing efficiencies are power dependent, so as power level increases the capturing

efficiency also increases (Fig. 7A); this has the side effect that at higher powers the beds saturate and the difference in performance is masked. Examining the 7 dBm data set, it is clear that the most efficient trapping occurs using the 15 μm microparticle bed.

Turning to the effect of bead material, from the theoretical values, we expect to see marginally superior performance from PMMA particles over PS, and that SG offers the worst collection capability. Fig. 7B confirms the simulation trend as PMMA performs better than PS and SG, again, most clearly seen at lower power levels while at higher powers although PMMA's mean efficiency is higher its variation is not statistically significant due to saturation. PMMA capturing efficiencies are 80% ±12 at 10 dBm and 92% ±7.8 at 14 dBm, in both cases when actuation is at a frequency within the first SW peak. In contrast silica glass performs best at its second experimental peak, related to the second predicted TW– peak.

3.3 Capturing and enrichment of exosomes

Exosomes are in the range of 30–200 nm making them much harder to trap than 500 nm polystyrene particles we used so far in the interest of better visualisation and measurement of the system performance and efficiency. Moreover, exosomes like other biological particles have a softer construction than a polymer material, yielding less acoustic contrast and so lower trapping forces. In this work, we discussed a packed bed made of larger particles produces higher capturing even though it has larger pores. To demonstrate separation and enrichment of biological samples, a sample of exosomes with BCA concentration of 7918 μg mL^{-1} and mean particle size 167 nm was passed through the ultrasonically activated packed bed of 15 micron particles in a channel with 94 μm width and 32 μm height. The exosome sample diluted in phosphate-buffered saline (PBS) buffer and labelled using ExoGlow protein labelling kit (EXOGP100A-1, Systems Biosciences – USA). The flowrate was set at 0.1 μL min^{-1} and fluorescent filter with emission wavelength of 576–596 nm used for visualisation. The interdigital transducers (IDTs) were excited at a frequency of 70 MHz and a power of 14 dBm for 32 s. Fig. 8 shows the trapping, enrichment and release sequence starting with first left caption of the packed bed before excitation of ultrasound wave. During the 32 seconds of SAW activation, the intensity of the downstream flow dropped very significantly, showing that the packed bed captured the vast majority of exosomes. Upon deactivation of the SAW, the exosomes were washed out of the bed, and so created a high concentration (high intensity) sample emerging from the bed (see caption t_0 and ESI† Movie). Consecutive images show this release downstream of the micropillars, the front of the batch is indicated in the Fig. 8 (captions t_1 to t_4). The enriched batch swept the distance of about 225 μm in those four images which spand a duration of 450 milliseconds. Hence, they travel with the average speed of slightly less than

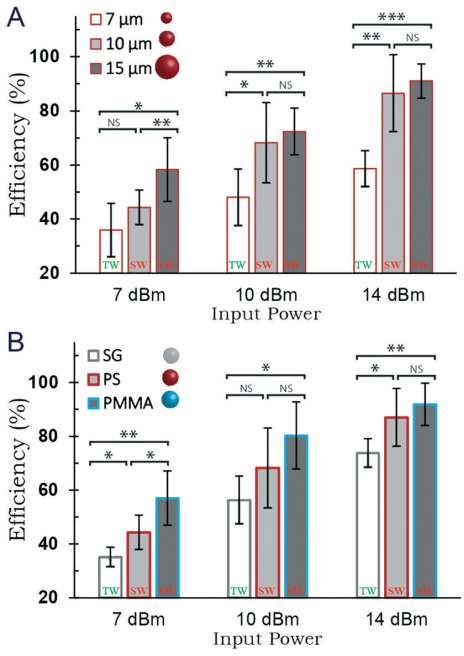

Fig. 7 Experimental data comparing the capturing efficiencies of different packed bed particles. In (A) the size is varied and in (B) the material. In each case a peak frequency is used, namely 79 MHz (TW) for 7 μm, 72 MHz (SW) for 10 μm and 40 MHz (SW) for 15 μm PS beads; and 67 MHz (SW) for PMMA and 78 MHz (TW) for silica glass. The error bars show standard deviation. Statistically different experiments are denoted by $*p < 0.05$, $**p < 0.01$ and $***p < 0.001$. NS stands for non-significant.

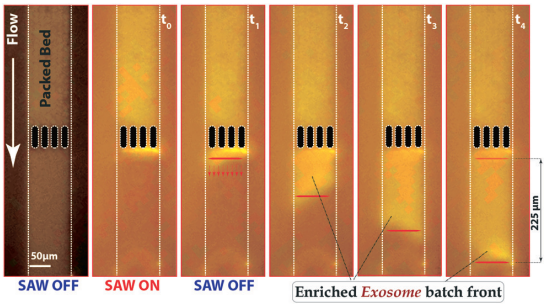

Fig. 8 A series of experimental images demonstrate the collection and enrichment of exosomes. The SAW actuation is activated in only one of the images, this image, labelled t_0, is taken after 32 s of actuation, the raised intensity of the packed bed indicates the entrapment of the fluorescently labelled exosomes. However, the capture is most clearly observed when the SAW is deactivated, and the exosomes leave the packed bed, images of which are presented over closely spaced time steps: t_1 = 300 ms, t_2 = 450 ms, t_3 = 600 ms and t_4 = 750 ms. The front of the highly concentrated batch of released exosomes is tracked as it passes downstream at a speed of 0.5 mm s^{-1}, which corresponds with the rate of a plug flow emerging from the packed bed (a typical laminar flow profile will only develop further down the channel).

0.5 mm s^{-1}, which is the same speed as the flow, further showing that the intensity front passing along the channel is due to released exosomes re-entering the flow. Also, another demonstration of exosome capture at Fig. S5A† clearly demonstrates the capturing of fluorescent labelled exosomes. Here, images are shown for a longer period after excitation ceased so that it can be seen that the intensity of the bed drops to background levels, showing the successful release of the concentrated exosomes. Fig. S5B† represents the same by showing the spatial and temporal intensity profile of the exosome collection and release.

3.4 Integrity of bioparticles

High frequency ultrasonic actuation is not damaging to the viability of cells,[55] we now check that the integrity of the much smaller exosomes is also uncompromised. To do this, a sample of liposomes with mean particles size of 100 nm with concentration of 1 mg mL^{-1} diluted in buffer (10 mM HEPES, 150 mM NaCl, pH 7.2) was passed through a single outlet microfluidic channel (94 μm × 21 μm) filled with a packed bed of 10 micron polystyrene particles (Magsphere, USA) where the collection and release cycles were run

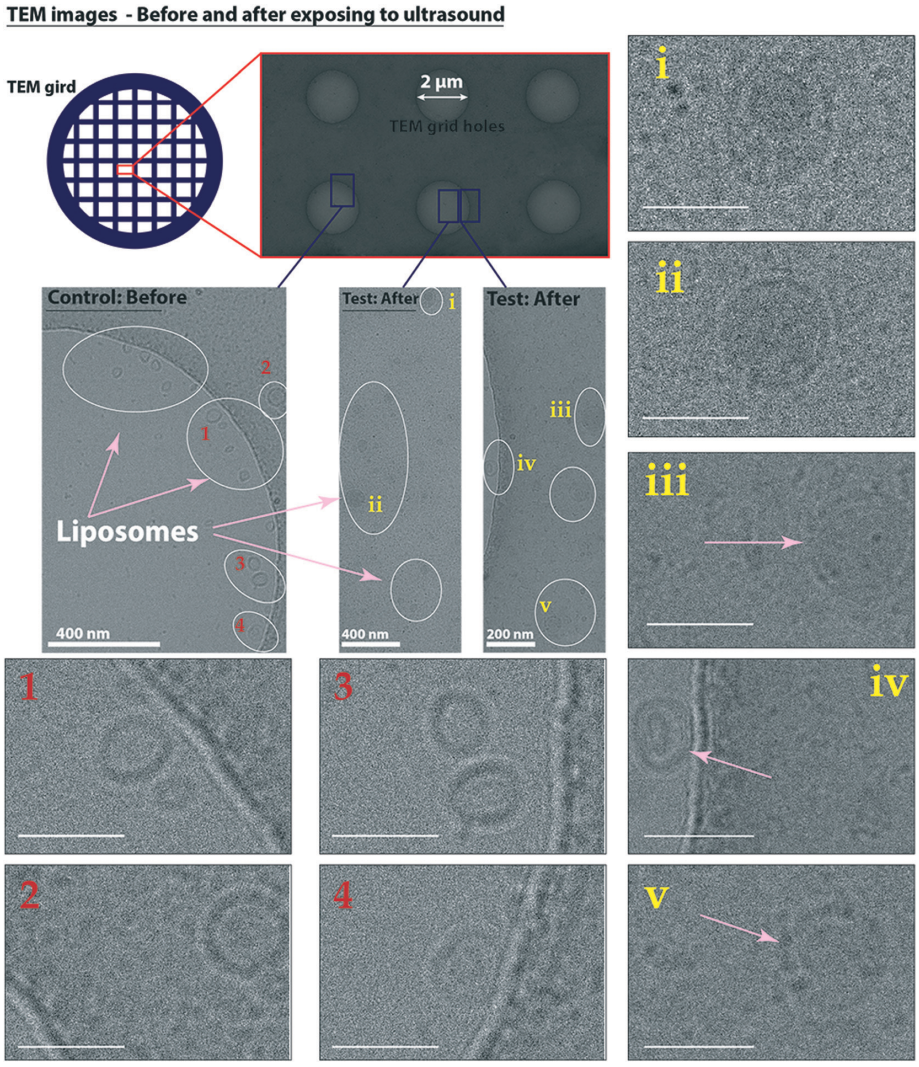

Fig. 9 Transmission electron microscopy (TEM) images of liposomes (with mean size of 100 nm) are presented. Different sets of images are taken before (insets 1–4) and after (insets i–v) exposure to ultrasound trapping in the activated packed bed. The exposed sample was extracted over 1 hour of cycling through trapping and enrichment stages, using a bed in a 94 μm wide channel activated at 70 MHz and 13 dBm. The images show that the lipid bilayer membrane remains intact after exposure to ultrasound. All scale bars are 100 nm unless specified (see Fig. S6 in the ESI† for more post exposure images).

continuously for 1 hour to ensure that all particles are exposed to the excitation frequency (70 MHz with 13 dBm power level at source signal generator). Transmission electron microscopy (TEM) images of the control (liposomes before exposure to the ultrasound) and test sample (collected after the continuous exposure to ultrasound and passed through the acoustically activated packed bed) show the membranes remain intact and lipid bilayer is observable from both images.

The imaged liposomes retained their spherical shape and morphology, suggesting that the lipid bilayer membrane of liposomes held in the packed bed can withstand the mechanical energy imparted by the ultrasonic exposure (Fig. 9).[44] As the lipid bilayer is a universal component of all cellular membranes and also makes up the envelope of most viruses, based on this study, it is expected that the morphology and integrity of other particles such as viruses, bacteria and exosomes will also be preserved after exposure to the ultrasound activated packed bed.

4 Conclusion

The physics of the ultrasonically activated packed bed is highly complex due to the nature of the scattering, SAW propagation and coupling, and the partial reflections from the roof of the PDMS channel. Nonetheless, through reduction of the system to its most basic components, in a manner in which both the effect of particle size on Bjerknes forces and pore size are captured, operating frequencies could be predicted. Modes of operation were numerically predicted and experimentally found for both travelling and standing wave dominated excitations. Indeed the experimental frequency analysis results could not have been understood in the absence of consideration of both these forms of excitation. Experimental examination of the capturing efficiency showed that the 15 μm microparticles outperformed both the 7 and 10 μm beads. Indicating that the effect of a larger scattering body was more significant than the greater separation caused by a larger pore size. The data also showed that PS and PMMA particles far outperformed the much stiffer SG particles. Applying this insight, the capability of the sound wave activated nano-sieve was extended to include the capture of exosomes.

Conflicts of interest

There are no conflicts to declare.

Acknowledgements

This work is funded by the Australian Research Council by way of grant no. DP160101263. This work was performed in part at the Melbourne Centre for Nanofabrication (MCN) in the Victorian Node of the Australian National Fabrication Facility (ANFF). We thank Dr. Bahman Delalat for his assistance in the labelling of the exosomes.

References

1 Z. Mao, P. Li, M. Wu, H. Bachman, N. Mesyngier, X. Guo, S. Liu, F. Costanzo and T. J. Huang, *ACS Nano*, 2017, **11**, 603–612.
2 B. W. Drinkwater, *Lab Chip*, 2016, **16**, 2360–2375.
3 A. Franklin, A. Marzo, R. Malkin and B. W. Drinkwater, *Appl. Phys. Lett.*, 2017, **111**, 094101.
4 G. T. Silva, J. H. Lopes, J. P. Leão-Neto, M. K. Nichols and B. W. Drinkwater, *Phys. Rev. Appl.*, 2019, **11**, 054044.
5 S. Sepehrirahnama, K.-M. Lim and F. S. Chau, *J. Acoust. Soc. Am.*, 2015, **137**, 2614–2622.
6 R. Habibi, C. Devendran and A. Neild, *Lab Chip*, 2017, **17**, 3279–3290.
7 P. Glynne-Jones, R. J. Boltryk, N. R. Harris, A. W. Cranny and M. Hill, *Ultrasonics*, 2010, **50**, 68–75.
8 J. Behrens, S. Langelier, A. R. Rezk, G. Lindner, L. Y. Yeo and J. R. Friend, *Lab Chip*, 2015, **15**, 43–46.
9 J. P. Lata, F. Guo, J. Guo, P.-H. Huang, J. Yang and T. J. Huang, *Adv. Mater.*, 2016, **28**, 8632–8638.
10 J. P. K. Armstrong, J. L. Puetzer, A. Serio, A. G. Guex, M. Kapnisi, A. Breant, Y. Zong, V. Assal, S. C. Skaalure, O. King, T. Murty, C. Meinert, A. C. Franklin, P. G. Bassindale, M. K. Nichols, C. M. Terracciano, D. W. Hutmacher, B. W. Drinkwater, T. J. Klein, A. W. Perriman and M. M. Stevens, *Adv. Mater.*, 2018, **30**, 1802649.
11 G. Destgeer, K. H. Lee, J. H. Jung, A. Alazzam and H. J. Sung, *Lab Chip*, 2013, **13**, 4210–4216.
12 M. Wu, A. Ozcelik, J. Rufo, Z. Wang, R. Fang and T. Jun Huang, *Microsyst. Nanoeng.*, 2019, **5**, 32.
13 D. J. Collins, T. Alan and A. Neild, *Lab Chip*, 2014, **14**, 1595–1603.
14 H. Cong, J. Chen and H.-P. Ho, *Sens. Actuators, B*, 2018, **264**, 224–233.
15 J. Nam and C. S. Lim, *Sens. Actuators, B*, 2018, **255**, 3434–3440.
16 H. Ahmed, J. Park, G. Destgeer, M. Afzal and H. J. Sung, *Appl. Phys. Lett.*, 2019, **114**, 043702.
17 M. Sesen, A. Fakhfouri and A. Neild, *Anal. Chem.*, 2019, **91**, 7538–7545.
18 C. Devendran, I. Gralinski and A. Neild, *Microfluid. Nanofluid.*, 2014, **17**, 879–890.
19 C. Reyes, L. Fu, P. P. A. Suthanthiraraj, C. E. Owens, C. W. Shields IV, G. P. López, P. Charbonneau and B. J. Wiley, *Part. Part. Syst. Charact.*, 2018, **35**, 1700470.
20 J. Zhou, R. Habibi, F. Akbaridoust, A. Neild and R. Nosrati, *Anal. Chem.*, 2020, **92**, 8569–8578.
21 A. Fakhfouri, C. Devendran, A. Ahmed, J. Soria and A. Neild, *Lab Chip*, 2018, **18**, 3926–3938.
22 J. Sun, Y. Xianyu and X. Jiang, *Chem. Soc. Rev.*, 2014, **43**, 6239–6253.
23 W. S. Bauer, C. P. Gulka, L. Silva-Baucage, N. M. Adams, F. R. Haselton and D. W. Wright, *Anal. Chem.*, 2017, **89**, 10216–10223.
24 Y. Ha, S. Ko, I. Kim, Y. Huang, K. Mohanty, C. Huh and J. A. Maynard, *ACS Appl. Nano Mater.*, 2018, **1**, 512–521.
25 J. Wen, L. A. Legendre, J. M. Bienvenue and J. P. Landers, *Anal. Chem.*, 2008, **80**, 6472–6479.

26 C. Chen, J. Skog, C.-H. Hsu, R. T. Lessard, L. Balaj, T. Wurdinger, B. S. Carter, X. O. Breakefield, M. Toner and D. Irimia, *Lab Chip*, 2010, **10**, 505–511.

27 G. D. Chen, C. J. Alberts, W. Rodriguez and M. Toner, *Anal. Chem.*, 2010, **82**, 723–728.

28 J. Yoon, Y.-J. Yoon, T. Y. Lee, M. K. Park, J. Chung and Y. Shin, *Sens. Actuators, B*, 2018, **255**, 1491–1499.

29 G. A. Toranzos, G. A. McFeters, J. José Borrego and M. Savill, in *Manual of Environmental Microbiology*, American Society of Microbiology, 3rd edn, 2007, pp. 249–264.

30 J. H. M. van Lieverloo, G. A. M. Mesman, G. L. Bakker, P. K. Baggelaar, A. Hamed and G. Medema, *Water Res.*, 2007, **41**, 4299–4308.

31 X. Zhou, D. Liu, R. Zhong, Z. Dai, D. Wu, H. Wang, Y. Du, Z. Xia, L. Zhang, X. Mei and B. Lin, *Electrophoresis*, 2004, **25**, 3032–3039.

32 W. Lodder and A. M. de Roda Husman, *Lancet Gastroenterol. Hepatol.*, 2020, **5**, 533–534.

33 P. M. Gundy, C. P. Gerba and I. L. Pepper, *Food Environ. Virol.*, 2008, **1**, 10.

34 W. Wang, J. Luo and S. Wang, *Adv. Healthcare Mater.*, 2018, **7**, 1800484.

35 O. G. De Jong, B. W. M. Van Balkom, R. M. Schiffelers, C. V. C. Bouten and M. C. Verhaar, *Front. Immunol.*, 2014, **5**, 608.

36 G. D. Kusuma, J. Carthew, R. Lim and J. E. Frith, *Stem Cells Dev.*, 2017, **26**, 617–631.

37 M. Evander, O. Gidlöf, B. Olde, D. Erlinge and T. Laurell, *Lab Chip*, 2015, **15**, 2588–2596.

38 J. J. Lai, J. M. Hoffman, M. Ebara, A. S. Hoffman, C. Estournès, A. Wattiaux and P. S. Stayton, *Langmuir*, 2007, **23**, 7385–7391.

39 P. Li, M. Kaslan, S. H. Lee, J. Yao and Z. Gao, *Theranostics*, 2017, **7**, 789–804.

40 A. Liga, A. D. B. Vliegenthart, W. Oosthuyzen, J. W. Dear and M. Kersaudy-Kerhoas, *Lab Chip*, 2015, **15**, 2388–2394.

41 J. Caradec, G. Kharmate, E. Hosseini-Beheshti, H. Adomat, M. Gleave and E. Guns, *Clin. Biochem.*, 2014, **47**, 1286–1292.

42 K. Yakimchuk, *Mater. Methods*, 2015, **5**, 1450–1453.

43 A. Safdar, A. Saleem and M. A. Tarnopolsky, *Nat. Rev. Endocrinol.*, 2016, **12**, 504.

44 M. Wu, Y. Ouyang, Z. Wang, R. Zhang, P.-H. Huang, C. Chen, H. Li, P. Li, D. Quinn, M. Dao, S. Suresh, Y. Sadovsky and T. J. Huang, *Proc. Natl. Acad. Sci. U. S. A.*, 2017, **114**, 10584.

45 K. Lee, H. Shao, R. Weissleder and H. Lee, *ACS Nano*, 2015, **9**, 2321–2327.

46 T. Salafi, K. K. Zeming and Y. Zhang, *Lab Chip*, 2017, **17**, 11–33.

47 S. Lin, Z. Yu, D. Chen, Z. Wang, J. Miao, Q. Li, D. Zhang, J. Song and D. Cui, *Small*, 2020, **16**, 1903916.

48 R. Habibi and A. Neild, *Lab Chip*, 2019, **19**, 3032–3044.

49 S. Ergun, *Chem. Eng. Prog.*, 1952, **48**, 89–94.

50 D. Nemec and J. Levec, *Chem. Eng. Sci.*, 2005, **60**, 6947–6957.

51 M. Sesen, C. Devendran, S. Malikides, T. Alan and A. Neild, *Lab Chip*, 2017, **17**, 438–447.

52 J. W. Ng, D. J. Collins, C. Devendran, Y. Ai and A. Neild, *Microfluid. Nanofluid.*, 2016, **20**, 151.

53 C. Devendran, T. Albrecht, J. Brenker, T. Alan and A. Neild, *Lab Chip*, 2016, **16**, 3756–3766.

54 M. Gröschl, *Acta Acust. Acust.*, 1998, **84**, 432–447.

55 C. Devendran, J. Carthew, J. E. Frith and A. Neild, *Adv. Sci.*, 2019, **6**, 1902326.

Electronic Supplementary Material (ESI) for Lab on a Chip.

Supporting Information (SI) for: Exosome trapping and enrichment using a Sound Wave Activated Nano-Sieve (SWANS)†

Ruhollah Habibi Vincent He Sara Ghavamian Alex de Marco
Tzong-Hsien Lee Marie-Isabel Aguilar Dandan Zhu Rebecca Lim
Adrian Neild*

*Corresponding author: Laboratory for Micro Systems, Department of Mechanical and Aerospace Engineering, Monash University, Clayton, Victoria 3800, Australia.; E-mail: adrian.neild@monash.edu

Table S1: *Basic parameters of all FEM models that were simulated in this work based on Ref. 1 methodology. Material data were obtained from COMSOL material library otherwise stated.*

Parameter	Symbol	Unit	Value
Fluid Domain			
Water			
Density	ρ_f	kg m^{-3}	1000
Speed of sound	c_f	m s^{-1}	1500
Domain height	L	µm	100
Domain width	W	µm	50
Frequency	f	MHz	see Table 2
Wavelength	λ	µm	c_f/f
Wavenumber	k	µm	$2\pi/\lambda$
Acoustic pressure amp.	P_0	kPa	100
Max. mesh size	e_f	nm	400-600
Curvature factor		-	0.15
Max. mesh growth rate		-	1.05
Solid Domain (NP)			
Material			Polystyrene
Density[2]	ρ_{ps}	kg m^{-3}	1050
Modulus of elasticity[a]	E_{ps}	GPa	3.60
Poisson ratio[3]	ν_{ps}	-	0.35
Domain dimensions:			
Nanoparticle diameter	d_{NP}	µm	0.5
Max. mesh size range	e_s	nm	60∼100
Curvature factor		-	0.15
Max. mesh growth rate		-	1.05
Fluid-Solid interface			
Mesh size range	e_1	nm	7∼20
Curvature factor		-	0.15
Max. mesh growth rate		-	1.05

[a] Calculated from Bulk Modulus (K_{ps}) as $E_{ps} = 3K_{ps}(1 - 2\nu_{ps})$ from ref. 3 and 4.

Table S2: *Specific parameters of each FEM model that were simulated in this work to study the effect of size or material of microparticles (MPs) in the packed bed. Material data are obtained from COMSOL material library otherwise stated.*

Parameter	Symbol	Unit	**7-PS**	**10-PS**	**15-PS**	**10-PMMA**	**10-SG**
Fluid Domain							
Water							
Frequency	f	MHz	20 - 215	15 - 150	10 - 100	15 - 150	15 - 150
Solid Domain (MP)							
Material			PS	PS	PS	PMMA	Silia Glass
Microparticle diameter	D_{MP}	µm	7	10	15	10	10
Density	ρ_{ps}	kg m^{-3}	1050[2]	1050[2]	1050[2]	1190	2203
Modulus of elasticity	E_{ps}	GPa	3.60[a]	3.60[a]	3.60[a]	3.0	73.1
Poisson ratio	ν_{ps}	-	0.35[3]	0.35[3]	0.35[3]	0.4	0.17
Fluid-Solid interface							
Gap between MP and NP	Gap	nm	300	500	900	500	500

[a] Calculated from Bulk Modulus (K_{ps}) as $E_{ps} = 3K_{ps}(1 - 2\nu_{ps})$ from ref. 3 and 4.

References

[1] R. Habibi, C. Devendran and A. Neild, *Lab Chip*, 2017, **17**, 3279–3290.

[2] P. B. Muller, R. Barnkob, M. J. H. Jensen and H. Bruus, *Lab Chip*, 2012, **12**, 4617–4627.

[3] P. Mott, J. Dorgan and C. Roland, *Journal of Sound and Vibration*, 2008, **312**, 572 – 575.

[4] R. Kono, *Journal of the Physical Society of Japan*, 1960, **15**, 718–725.

[5] R. Habibi and A. Neild, *Lab Chip*, 2019, **19**, 3032–3044.

Table S3: *Summary of peak frequencies and their corresponding attraction Force on the 500 nm nanoparticle for each simulated pair of nanoparticle and microparticle.*

PS 7 μm	f_1^*	$\mathbf{F}_{att}$ (fN)	f_2^*	$\mathbf{F}_{att}$ (fN)	f_3^*	$\mathbf{F}_{att}$ (fN)
SW	94	13.71	123	18.01	174	19.31
TW +	80	31.87	132	136.78	-	-
TW –	84	36.24	134	23.11	-	-

PS 10 μm	f_1^*	$\mathbf{F}_{att}$ (fN)	f_2^*	$\mathbf{F}_{att}$ (fN)	f_3^*	$\mathbf{F}_{att}$ (fN)
SW	66	26.03	87	35.29	122	39.09
TW +	55	18.27	95	28.07	-	-
TW –	56	19.18	-	-	-	-

PS 15 μm	f_1^*	$\mathbf{F}_{att}$ (fN)	f_2^*	$\mathbf{F}_{att}$ (fN)	f_3^*	$\mathbf{F}_{att}$ (fN)
SW	44	52.38	58	75.27	81	86.43
TW +	36	10.66	63	14.05	-	-
TW –	36	10.29	-	-	-	-

PMMA 10 μm	f_1^*	$\mathbf{F}_{att}$ (fN)	f_2^*	$\mathbf{F}_{att}$ (fN)	f_3^*	$\mathbf{F}_{att}$ (fN)
SW	60	43.74	85	47.23	115	39.92
TW +	53	20.86	85	26.68	113	40.53
TW –	56	19.18	-	-	-	-

SG 10 μm	f_1^*	$\mathbf{F}_{att}$ (fN)	f_2^*	$\mathbf{F}_{att}$ (fN)	f_3^*	$\mathbf{F}_{att}$ (fN)
SW	69	9.87	-	-	-	-
TW +	73	7.66	-	-	-	-
TW –	69	8.28	97	33.11	-	-

4

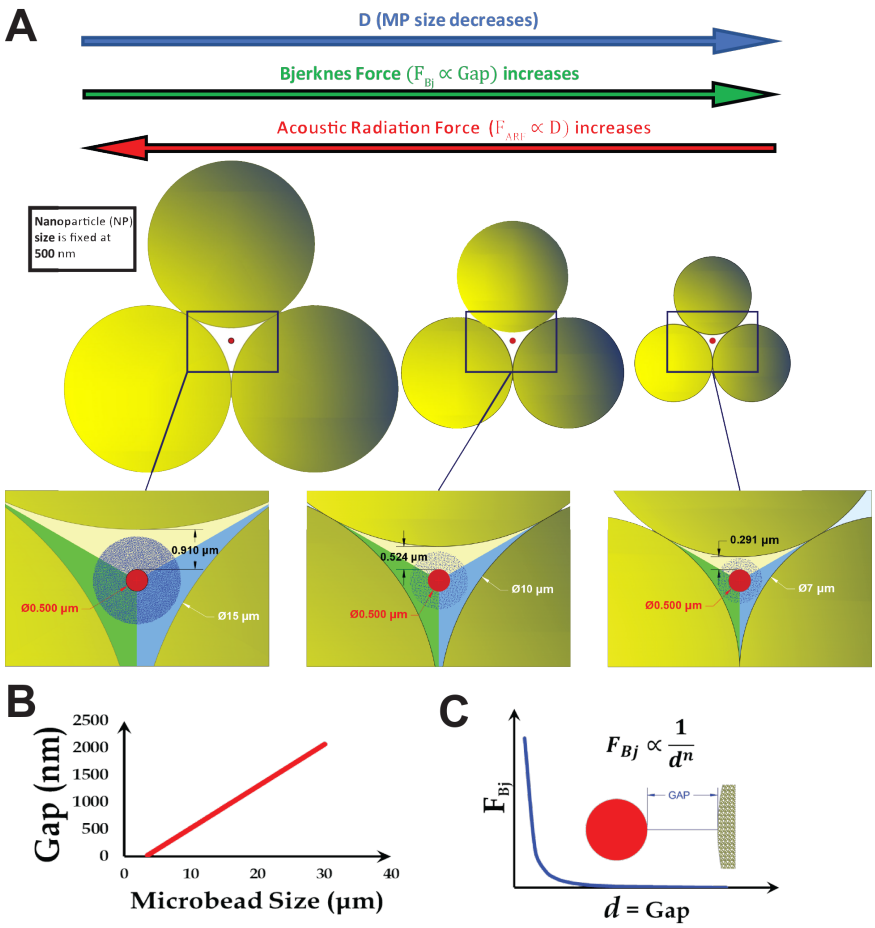

Fig. S1: *(A) Interplay between the size of the microbeads in the packed bed and the attraction force (secondary Bjerknes force) induced on nanoparticles: By increasing the MP size, the gap between the beads and the nanoparticle decreases (linearly as shown in (B) so enhances the Bjerknes force between the MP and NP as the Bjerknes force scales to the inverse of gap squared or even higher powers(C). On the other hand, although increasing the size of the beads increases the gap, but with the same acoustically normalised size (d/λ), larger particle generates higher amplitude scattering so higher radiation forces (both primary and secondary). At a fixed gap distance, larger particle normally generates higher attraction forces.*

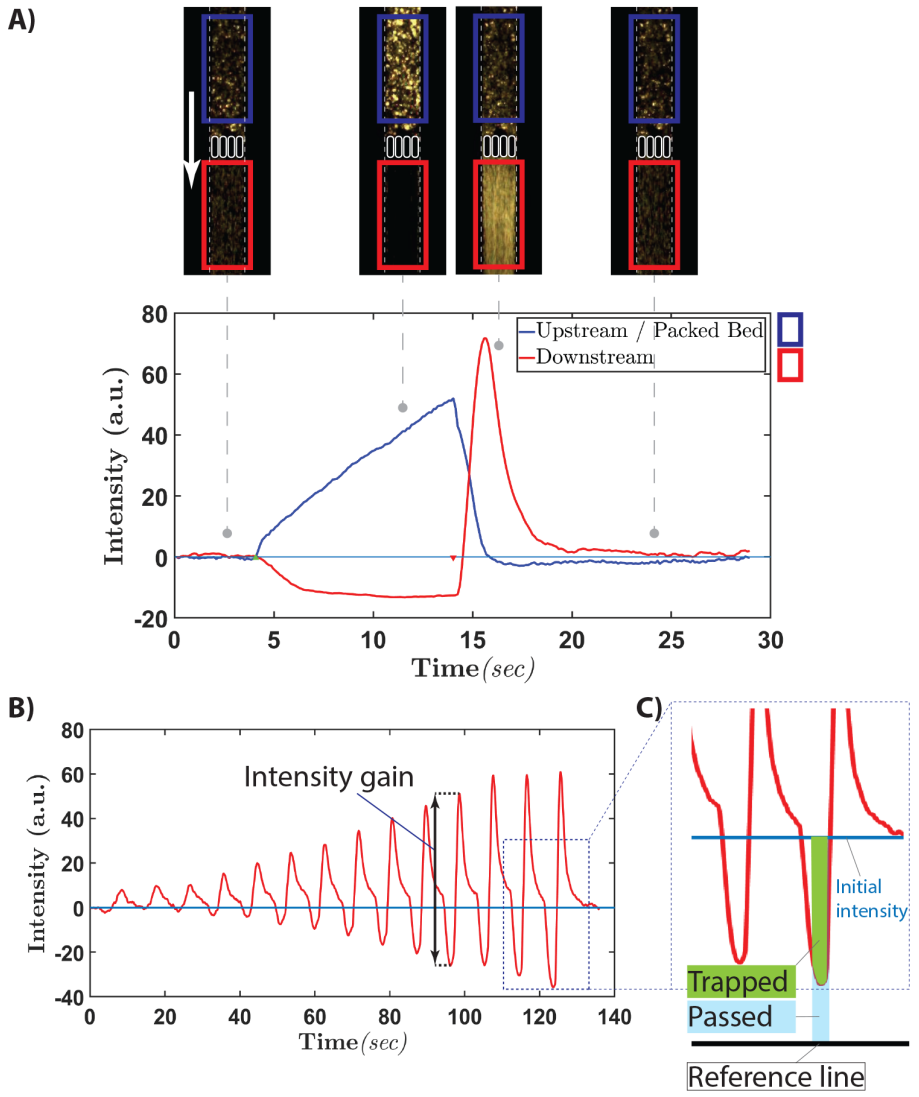

Fig. S2: *(A) Measuring the fluorescent intensity level indicates successful trapping of particles in the packed bed and also capturing efficiency when measured at the downstream of the pillars. Here, intensity change is demonstrated when the packed bed is excited at one fixed frequency. Captions are reproduced from Fig. 1B. The intensity level is set to zero at initial level (before SAW activation). (B) A typical frequency response of fluorescent intensity level change as an indication of nanoparticle collection/release, measured here at the packed bed downstream; Measurement of the intensity is calculated at different locations (upstream or downstream) to find the mean value of intensity gain at each frequency. The intensity gain at each frequency is then normalised versus highest and lowest values. Similarly, intensity measurement and normalisation is discussed in more detail in Ref. 5. (C) The efficiency of nanoparticle capturing is measured by investigating the change of the intensity at the downstream while ultrasound is activated (SAW is on). If all particles are trapped at the upstream the intensity level drops to the lowest level (indicated as reference line). So the efficiency is calculated as the ratio of the trapped particles to the total (sum of trapped and passed particles).*

6

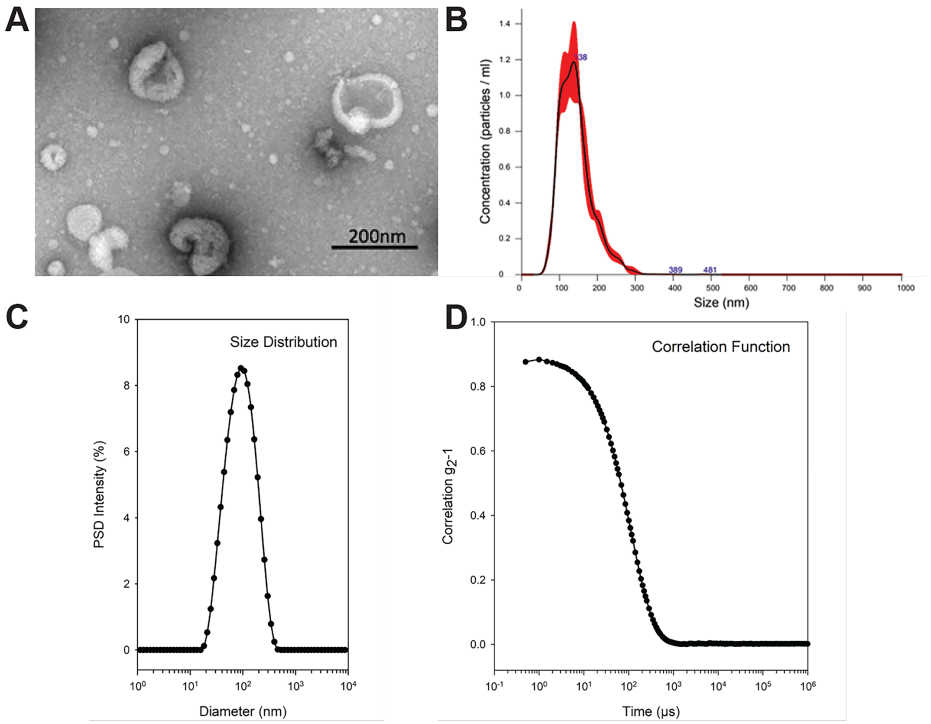

Fig. S3: *A) TEM image of the original exosome sample: the EVs used for this project are of typical exosome shape, bearing a distinct cup-shaped morphology. B) The particle concentration of the EV sample was* 4.5×10^{10} *per mL. The particle size distribution was D10 67 nm, D50 109 nm and D90 300.5 nm with mean size of 167.3 nm. C) and D) Dynamic light scattering (DLS) results of liposome size distribution. The mean diameter of liposomes measured at 75.75 nm (peak at 107 nm) with PDI of 0.25 and mean count rate of 325.2.*

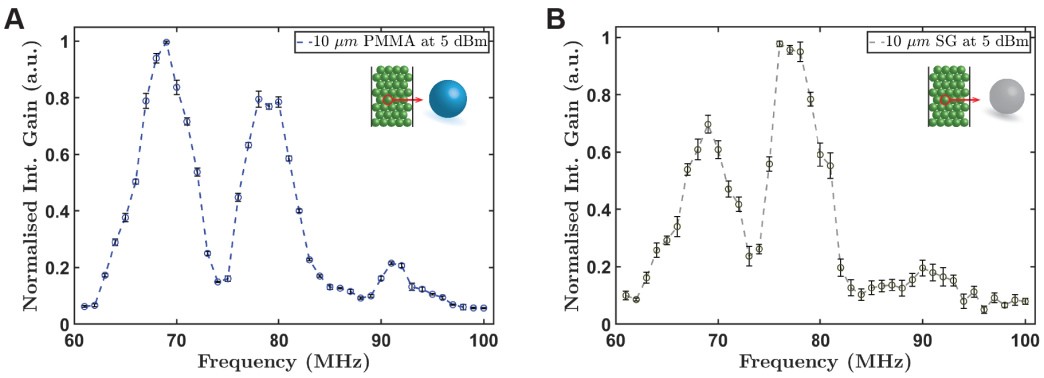

Fig. S4: *Experimental results for intensity change (as an indication of fluorescent 500 nm NPs collection) for packed bed made of (A) 10 µm PMMA that shows two major peaks at frequencies around 70 MHz and 80 MHz and (B) 10 µm SG with two major peaks around 70 and 79 MHz.*

8

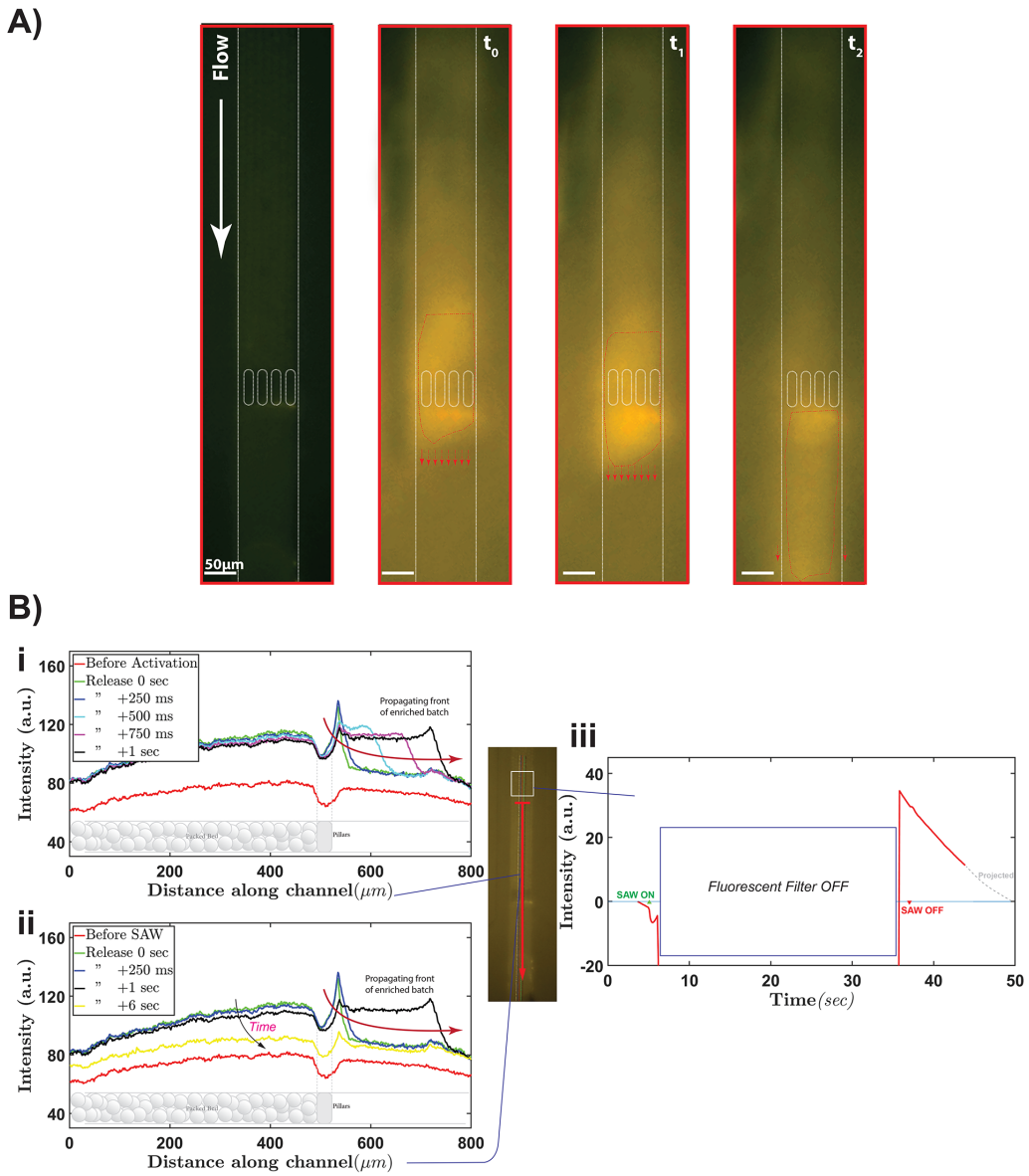

Fig. S5: *(A) Another experimental demonstration of capturing, enriching and releasing of high concentrated exosome batch to the downstream, where the left caption shows the channel before SAW excitation. Further captions show the release and propogation of high concentrated batch toward the downstream at t_0 = After SAW OFF, $t_1 = t_0 + 100$ ms and then $t_2 = t_0 + 3$ sec when the front of the batch left the image borders. (B) The spatial profile of intensity along the channel length at different times shows the release of high concentrated batch of exosomes when SAW is turned off. The front propagates and leaves the frame area(i); intensity level eventually will revert to initial level (ii). Temporal variation of intensity before and after SAW activation (iii).*

9

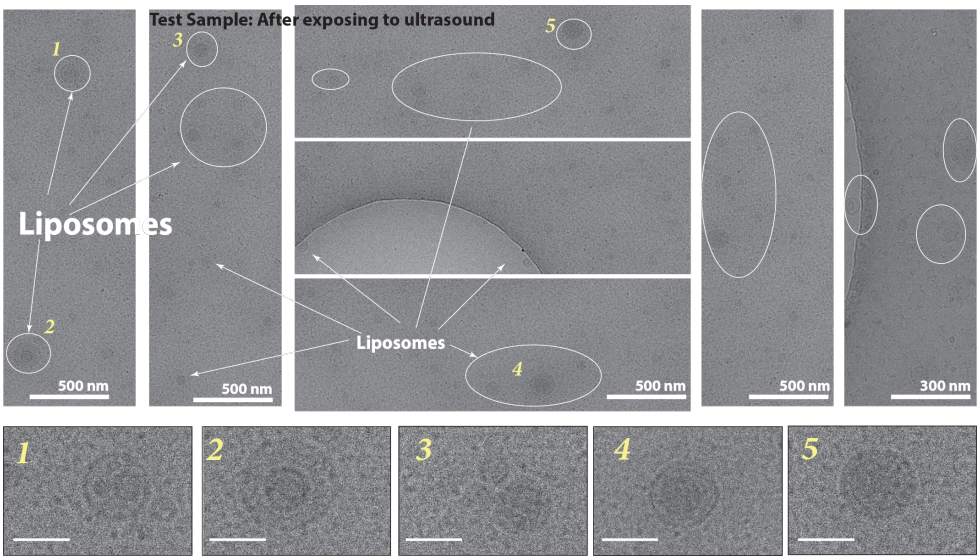

Fig. S6: *Multiple Transmission electron microscopy (TEM) images of liposome particles (with 100 nm mean size) show that the particles retain their morphology and bilayer lipid membrane after being exposed to ultrasound wave (SAW 70 MHz at 13 dBm source power level), collected and released by the activated packed bed. The sample collected after 1 hour continuous collection and release cycles. Insets 1 to 5 shows examples of liposome particles after ultrasound exposure for more clarity. All scale bars are 100 nm unless specified.*

10

Chapter 6

Conclusions and Future Work

This chapter summarises the key findings and contributions of the research work discussed throughout this thesis. Following these recommendations, future work will be presented.

6.1 Contributions

While some practical solutions for trapping and patterning cells and particles have advanced in recent years, there is an apparent gap of knowledge in the underlying physics responsible. Hence, this thesis focused on expanding the understanding of the interplaying mechanisms of suspended particles in acoustic fields, showing the potentials and exploiting such knowledge for next-generation trapping systems. In particular, a body of knowledge on secondary inter-particle forces, also known as Bjerknes forces, between resonant particles was built piece by piece, so that a clear map of the effect of different parameters such as gap, angle, position, frequency, size and mechanical properties on these forces can be drawn. A new system for the trapping of nanoparticles in a continuous flow was theorised and then developed on the foundation of those theoretical findings. Applicability of secondary forces to manipulate suspended matter within microfluidic or macro-scale systems opens up the possibility of realising such systems.

The following will discuss the specific contributions that stem from each of the chapters included in this thesis.

Chapter 3

In this chapter, a computational model using COMSOL Multiphysics with a finite element analysis package, was developed to calculate the acoustic radiation force (ARF) on a spherical solid elastic particle by surface integration of convective and momentum flux. In contrast to other analytical methods, the solution is not limited to small size particles or time consuming with numerous iterations. The ARF on one and two spheres in a one-dimensional standing wave field were computed for three different materials, PS, PMMA and SG for sizes less than

half the wavelength ($\lambda/2$) since the node to node distance is only a half-wavelength. From the ARF, the frequency response within the range of d/λ <1/2, three distinct regions were observed. For instance, for PMMA in the region A ($0 < d/\lambda < 0.33$) the ARF is positive and therefore pushes the particles to the pressure nodes, whereas in region B ($0.33 < d/\lambda < 0.42$) the ARF is negative and the particles are attracted to the antinodes and in then next region, C ($0.42 < d/\lambda < 0.5$) the ARF is again positive. Regions B and C also contain the first and second resonance frequencies. This trend of alternating ARF signs and collection points repeats. PS particles demonstrate similar trends to PMMA particles seeing as their mechanical properties are comparable. SG particles also demonstrate a similar trend of alternating ARF however, no resonance is observed in the first half wavelength as it is stiffer in comparison to the other two materials.

Chapter 3 discusses for the first time, how large particles interact at each region and how resonance frequencies affect secondary Bjerknes forces. Although in Region B the secondary forces are attractive at small gaps between two particles, Region B showed a striking rise of attractive Bjerknes forces. Evaluating these interactions with different gaps between the two particles and at different positions of the pair of particles with respect to wave axis, a map depicted all possible scenarios was obtained. The map shows that there is a narrow range of frequencies in region C where the Bjernkes forces are repulsive at all positions and for all gaps. Therefore, particles will be lead to single pressure nodes without forming aggregates. This is in agreement with previously demonstrated single particle and cell patterning in an experimental method.

However, numerical simulations of cells in Chapter 3 shows that the patterning of single cells per well is achievable at sizes close to half-wave length ($0.4 \lesssim d/\lambda < 0.5$) in a 1D ultrasound wave (or close to one wavelength in 2D field) due to the dominance of primary forces over the very weak attractive Bjerknes forces. Nonetheless, finding all of the attractive secondary forces in region B i.e. in all gaps and at all positions, causes clustering and leads to the idea of harnessing the clustering effect for particle trapping and collection that was later developed in the following chapter.

Chapter 4

In this chapter, computational numerical analysis using COMSOL Multiphysics was again used to demonstrate the peak of the secondary forces between a 10 μm and a 500 nm polystyrene particle in Region B, as was predicted in the previous chapter. When the frequency range is extended for a 10 micron polystyrene sphere, another peak in Region C (where the second resonance exists) appears. This confirms that the secondary forces are directly affected by the resonance frequencies. While in these frequencies a single large particle may not be stable enough to be used for entrapment of nanoparticles, having a packed bed of identical large particles (in this case 10 μm polystyrene particles) while excited at the frequencies where

the Bjerknes force is high, and also attractive, is proposed to construct a functional trapping system. This trapping system has been termed sound wave activated nano-sieve (SWANS). Simulations of multiple particles in a 2D geometry also shows that in that case, the force field in the pores between the large particles also leads the nanoparticles towards the large particles.

To evaluate this, Chapter 4 demonstrates a micro fluidic system composed of a PDMS microchannel and interdigital transducers (IDT) fabricated on the surface of a lithium niobate (LN) substrate. Micropillars in the channel helped to form the packed bed of 10 micron beads and the IDTs were used to excite a standing SAW field in the channel. Measuring the intensity level of the fluorescent light on the packed bed area and downstream, shows that there are two peak frequencies between 60 MHz to 90 MHz where the highest nanoparticle collection occurs. This trend is similar to the simulation predictions. Nanoparticles as small as 100 nm get trapped and held in the packed bed as long as the SAW is activated. This provides an on demand trap and release system with capturing efficiencies as high as 97%. Since the nanoparticle trapping is accomplished with a continuous flow system, the concentration of the sample increases in the packed bed; and upon the release, the sample has been estimated to being enriched up to 50 folds of its initial concentration within 10 sec.

An outstanding outcome of this chapter is the development of a trapping and enrichment system that is only dependent on the size and mechanical properties of the beads in the packed bed but not on the geometry of the channel like in other microfluidic based systems; possessing a huge potential for upscaling. A potential application of such an upscaled system is for exosome capturing and purification. Exosomes are believed to be the precursor for next generation regenerative medicine but only available in low concentrations in large volumes of bodily fluids such as plasma or milk, with sizes ranging between 50 - 200 nm.

This invention was filed for patent in Australia in March 2019 and internationally (through the PCT process) in March 2020.

Chapter 5

The effect of size and material properties of the microbeads on the performance of the SWANS is ad- dressed here. Although using two opposing IDTs generates standing surface acoustic wave (SSAW) on the substrate, travelling wave components are also present in the channel even when it is disturbed by the presences of the densely packed beads. Chapter 5 expands the theoretical model to include travelling waves so explains new collection peaks observed in the experiment results when the wider range of frequencies were tested. The new findings demonstrate that while the resonance frequencies of a single particle are independent of the wave form, peak frequencies of the secondary Bjerknes forces are different between standing waves and travelling waves. In this chapter, 3 different sizes of PS particle (7, 10 and 15 μm) and 3 different materials for a 10 micron particle (PS, PMMA and SG) were modelled

and tested in the packed bed of the SWANS system. Numerically and experimentally, it is demonstrated that when larger beads are used in the packed bed, the capturing efficiency increases and polymeric materials create more attraction due to higher scattering.

Finally, experimentally, larger 15 μm PS particles have been used to successfully trap exosomes with mean sizes of 160 nm. Also, to confirm the biocompatibility of the resonant packed bed of microbeads for trapping of biological samples, liposomes with mean sizes of 100 nm were tested and TEM images of samples collected downstream shows that their membranes were still intact and that the lipid bilayer was not ruptured due to the mechanical forces applied.

6.2 Future Work

As outlined in this thesis, investigations into trapping and patterning systems utilising ultrasound has resulted in several contributions. However, the need for further development of the system's capability of handling large volumes to trap nanoparticles is evidently necessary. This section will briefly discuss some ongoing and potential avenues for future research.

In Chapter 3, solid elastic spheres and liquid particles with white blood cells' acoustic properties were used to numerically simulate large cell responses to a wider range of frequencies for the purpose of trapping and patterning them in single nodes. However, expanding the model to a more realistic visco-elastic model may provide more information on cell reaction to ultrasonic waves. This information could be used for ultrasonic cell lysis studies as well. Furthermore, as acoustically large particles were investigated the stream effects were negligible and thus not included. However, an expanded model that takes the effect of viscous terms into account would extend our knowledge and understanding of the system in particular, as nanoparticles may undergo microstreaming effects.

Chapters 4 and 5 presented a novel method to trap and enrich nanoparticle samples in a continuous flow SAW-based microfluidic systems. The system only depends on the size and mechanical properties of the microparticles in the packed bed and is not limited to the channel geometry, and therefore has the full potential to be upscaled and applied in larger channels to process volumes required at the industrial level. Furthermore, it also has the advantage of being damage-free, label-free and less-laborious compared to conventional ultra-centrifugation or ultrafiltration.

As SWANS method only uses mechanical inter-particle forces to trap extracellular vesicles, such as exosomes it does not cause any chemical contamination. With an upscaled channel system (with a typical cross-section area of 5 mm $\times$ 5 mm), the projected operating time of SWANS system (with the flow speed and performance reported in Chapters 4 and 5)

would be significantly less than conventional systems. A thorough comparison of this newly established method (i.e. SWANS) with these standard methods in terms of throughput, yield and post-treatment protein structure will define the position of this technique among current methods and applications. Also, this system can be integrated into a viral or bacterial detection system by trapping target viruses or bacteria from a larger volume sample, or as a precursor for PCR system by concentrating the cell lysate.

"*The process of scientific discovery is, in effect, a continual flight from wonder*"

Albert Einstein

Bibliography

[1] Ruhollah Habibi, Citsabehsan Devendran, and Adrian Neild. Trapping and patterning of large particles and cells in a 1d ultrasonic standing wave. *Lab Chip*, 17:3279–3290, 2017.

[2] Ruhollah Habibi and Adrian Neild. Sound wave activated nano-sieve (swans) for enrichment of nanoparticles. *Lab Chip*, 19:3032–3044, 2019.

[3] Ruhollah Habibi, Vincent He, Sara Ghavamian, Alex de Marco, Tzong-Hsien Lee, Marie-Isabel Aguilar, Dandan Zhu, Rebecca Lim, and Adrian Neild. Exosome trapping and enrichment using a sound wave activated nano-sieve (swans). *Lab Chip*, 2020.

[4] R. Habibi and A. Neild. Nanoparticle capture using ultrasonic actuation. In *2019 20th International Conference on Solid-State Sensors, Actuators and Microsystems & Eurosensors XXXIII (TRANSDUCERS & EUROSENSORS XXXIII)*, pages 797–800, 2019.

[5] Neil Convery and Nikolaj Gadegaard. 30 years of microfluidics. *Micro and Nano Engineering*, 2:76–91, 2019.

[6] Adam Bohr, Stefano Colombo, Henrik Jensen, Hélder A. Santos, Dongfei Liu, and Hongbo Zhang. Chapter 15 - future of microfluidics in research and in the market. In *Microfluidics for Pharmaceutical Applications*, pages 425–465. William Andrew Publishing, 2019.

[7] Evan W. Newell and Mark M. Davis. Beyond model antigens: high-dimensional methods for the analysis of antigen-specific t cells. *Nature Biotechnology*, 32(2):149–157, 2014.

[8] Bertrand Guillotin and Fabien Guillemot. Cell patterning technologies for organotypic tissue fabrication. *Trends in Biotechnology*, 29(4):183–190, 2011.

[9] Tohid Fatanat Didar, Amir M. Foudeh, and Maryam Tabrizian. Patterning multiplex protein microarrays in a single microfluidic channel. *Anal. Chem.*, 84(2):1012–1018, January 2012.

[10] Akira Ito, Masamichi Kamihira, and Antonio Villaverde. Chapter 9 - tissue engineering using magnetite nanoparticles. In *Progress in Molecular Biology and Translational Science*, volume 104, pages 355–395. Academic Press, 2011.

[11] Dino Di Carlo, Liz Y. Wu, and Luke P. Lee. Dynamic single cell culture array. *Lab Chip*, 6(11):1445–1449, 2006.

[12] David J Collins, Belinda Morahan, Jose Garcia-Bustos, Christian Doerig, Magdalena Plebanski, and Adrian Neild. Two-dimensional single-cell patterning with one cell per well driven by surface acoustic waves. *Nature Communications*, 6:8686, 2015.

[13] Sangiliyandi Gurunathan, Min-Hee Kang, Muniyandi Jeyaraj, Muhammad Qasim, and Jin-Hoi Kim. Review of the isolation, characterization, biological function, and multifarious therapeutic approaches of exosomes. *Cells*, 8(4), 2019.

[14] Zongxing Wang, Hung-jen Wu, Daniel Fine, Jeffrey Schmulen, Ye Hu, Biana Godin, John X. J. Zhang, and Xuewu Liu. Ciliated micropillars for the microfluidic-based isolation of nanoscale lipid vesicles. *Lab Chip*, 13:2879–2882, 2013.

[15] Chao Liu, Jiayi Guo, Fei Tian, Na Yang, Fusheng Yan, Yanping Ding, JingYan Wei, Guoqing Hu, Guangjun Nie, and Jiashu Sun. Field-free isolation of exosomes from extracellular vesicles by microfluidic viscoelastic flows. *ACS Nano*, 11(7):6968–6976, 2017. PMID: 28679045.

[16] Benjamin H Wunsch, Joshua T Smith, Stacey M Gifford, Chao Wang, Markus Brink, Robert L Bruce, Robert H Austin, Gustavo Stolovitzky, and Yann Astier. Nanoscale lateral displacement arrays for the separation of exosomes and colloids down to 20 nm. *Nature nanotechnology*, 11(11):936, 2016.

[17] Hui Min Tay, Sharad Kharel, Rinkoo Dalan, Zhijie Joshua Chen, Kah Kee Tan, Bernhard O. Boehm, Say Chye Joachim Loo, and Han Wei Hou. Rapid purification of sub-micrometer particles for enhanced drug release and microvesicles isolation. *NPG Asia Materials*, 9(9):e434–e434, 2017.

[18] Elisabetta Primiceri, Maria Serena Chiriacò, Ross Rinaldi, and Giuseppe Maruccio. Cell chips as new tools for cell biology - results, perspectives and opportunities. *Lab Chip*, 13(19):3789–3802, 2013.

[19] Zhiyong Gong, Yong-Le Pan, and Chuji Wang. Optical configurations for photophoretic trap of single particles in air. *Review of Scientific Instruments*, 87(10):103104, October 2016.

[20] Su Hui Sophia Lee, T. Alan Hatton, and Saif A. Khan. Microfluidic continuous magnetophoretic protein separation using nanoparticle aggregates. *Microfluidics and Nanofluidics*, 11(4):429, May 2011.

[21] Stuart D. Ibsen, Jennifer Wright, Jean M. Lewis, Sejung Kim, Seo-Yeon Ko, Jiye Ong, Sareh Manouchehri, Ankit Vyas, Johnny Akers, Clark C. Chen, Bob S. Carter, Sadik C. Esener, and Michael J. Heller. Rapid isolation and detection of exosomes and associated biomarkers from plasma. *ACS Nano*, 11(7):6641–6651, July 2017.

[22] Kyungheon Lee, Huilin Shao, Ralph Weissleder, and Hakho Lee. Acoustic purification of extracellular microvesicles. *ACS Nano*, 9(3):2321–2327, March 2015.

[23] Mengxi Wu, Yingshi Ouyang, Zeyu Wang, Rui Zhang, Po-Hsun Huang, Chuyi Chen, Hui Li, Peng Li, David Quinn, Ming Dao, Subra Suresh, Yoel Sadovsky, and Tony Jun Huang. Isolation of exosomes from whole blood by integrating acoustics and microfluidics. *Proc Natl Acad Sci USA*, 114(40):10584, October 2017.

[24] SS Sadhal. Acoustofluidics 13: Analysis of acoustic streaming by perturbation methods. *Lab on a Chip*, 12(13):2292–2300, 2012.

[25] David J. Collins, Bee Luan Khoo, Zhichao Ma, Andreas Winkler, Robert Weser, Hagen Schmidt, Jongyoon Han, and Ye Ai. Selective particle and cell capture in a continuous flow using micro-vortex acoustic streaming. *Lab Chip*, 17(10):1769–1777, 2017.

[26] Armaghan Fakhfouri, Citsabehsan Devendran, Asif Ahmed, Julio Soria, and Adrian Neild. The size dependant behaviour of particles driven by a travelling surface acoustic wave (tsaw). *Lab Chip*, 18(24):3926–3938, 2018.

[27] Ivo Leibacher, Peter Reichert, and Jürg Dual. Microfluidic droplet handling by bulk acoustic wave (baw) acoustophoresis. *Lab Chip*, 15(13):2896–2905, 2015.

[28] Mihai Caleap and Bruce W. Drinkwater. Three-dimensional ultrasonic colloidal crystals. *Comptes Rendus Physique*, 17(5):501–511, 2016.

[29] Mikael Evander and Johan Nilsson. Acoustofluidics 20: Applications in acoustic trapping. *Lab Chip*, 12(22):4667–4676, 2012.

[30] Citsabehsan Devendran, Thomas Albrecht, Jason Brenker, Tuncay Alan, and Adrian Neild. The importance of travelling wave components in standing surface acoustic wave (ssaw) systems. *Lab Chip*, 16(19):3756–3766, 2016.

[31] David J Collins, Citsabehsan Devendran, Zhichao Ma, Jia Wei Ng, Adrian Neild, and Ye Ai. Acoustic tweezers via sub–time-of-flight regime surface acoustic waves. *Science Advances*, 2(7):e1600089, 2016.

[32] William Connacher, Naiqing Zhang, An Huang, Jiyang Mei, Shuai Zhang, Tilvawala Gopesh, and James Friend. Micro/nano acoustofluidics: materials, phenomena, design, devices, and applications. *Lab Chip*, 2018.

[33] Patrick Tabeling. *Introduction to microfluidics*. Oxford University Press, 2010.

[34] Henrik Bruus. Acoustofluidics 1: Governing equations in microfluidics. *Lab Chip*, 11:3742–3751, 2011.

[35] Nam-Trung Nguyen, Steven T Wereley, and Seyed Ali Mousavi Shaegh. *Fundamentals and applications of microfluidics*. Artech house, 2019.

[36] George M. Whitesides. The origins and the future of microfluidics. *Nature*, 442(7101):368–373, July 2006.

[37] P Gravesen, J Branebjerg, and O S Jensen. Microfluidics-a review. *Journal of Micromechanics and Microengineering*, 3(4):168–182, dec 1993.

[38] Ulrike Haessler, Yevgeniy Kalinin, Melody A. Swartz, and Mingming Wu. An agarose-based microfluidic platform with a gradient buffer for 3d chemotaxis studies. *Biomedical Microdevices*, 11(4):827–835, August 2009.

[39] Joost van Mameren, Gijs JL Wuite, and Iddo Heller. Introduction to optical tweezers: background, system designs, and commercial solutions. In *Single Molecule Analysis*, pages 1–20. Springer, 2011.

[40] Jeffrey R Moffitt, Yann R Chemla, Steven B Smith, and Carlos Bustamante. Recent advances in optical tweezers. *Annu. Rev. Biochem.*, 77:205–228, 2008.

[41] Iwijn De Vlaminck and Cees Dekker. Recent advances in magnetic tweezers. *Annual review of biophysics*, 41:453–472, 2012.

[42] Fernando Martinez-Pedrero and Pietro Tierno. Magnetic propulsion of self-assembled colloidal carpets: efficient cargo transport via a conveyor-belt effect. *Physical Review Applied*, 3(5):051003, 2015.

[43] Peter RC Gascoyne and Jody Vykoukal. Particle separation by dielectrophoresis. *Electrophoresis*, 23(13):1973–1983, 2002.

[44] WJ Liu, J Zhang, LJ Wan, KW Jiang, BR Tao, HL Li, WL Gong, and XD Tang. Dielectrophoretic manipulation of nano-materials and its application to micro/nano-sensors. *Sensors and Actuators B: Chemical*, 133(2):664–670, 2008.

[45] Albrecht Haake, Adrian Neild, Gerald Radziwill, and Jurg Dual. Positioning, displacement, and localization of cells using ultrasonic forces. *Biotechnology and bioengineering*, 92(1):8–14, 2005.

[46] Xiaoyun Ding, Peng Li, Sz-Chin Steven Lin, Zackary S. Stratton, Nitesh Nama, Feng Guo, Daniel Slotcavage, Xiaole Mao, Jinjie Shi, Francesco Costanzo, and Tony Jun Huang. Surface acoustic wave microfluidics. *Lab Chip*, 13:3626–3649, 2013.

[47] Margaret V Merritt, Milan Mrksich, and George M Whitesides. Using selfassembled monolayers to study the interactions of man-made materials with proteins. *Principles of tissue engineering. Austin: RG Landes Co*, page 211, 1997.

[48] Milan Mrksich and George M. Whitesides. Patterning self-assembled monolayers using microcontact printing: A new technology for biosensors? *Trends in Biotechnology*, 13(6):228 – 235, 1995.

[49] Rahul Singhvi, Amit Kumar, Gabriel P Lopez, Gregory N Stephanopoulos, Daniel IC Wang, George M Whitesides, Donald E Ingber, et al. Engineering cell shape and function. *SCIENCE-NEW YORK THEN WASHINGTON-*, pages 696–696, 1994.

[50] Ravi S Kane, Shuichi Takayama, Emanuele Ostuni, Donald E Ingber, and George M Whitesides. Patterning proteins and cells using soft lithography. *Biomaterials*, 20(23–24):2363 – 2376, 1999.

[51] Chunlong Tu, Bobo Huang, Jian Zhou, Yitao Liang, Jian Tian, Lin Ji, Xiao Liang, and Xuesong Ye. A microfluidic chip for cell patterning utilizing paired microwells and protein patterns. *Micromachines*, 8(1), 2017.

[52] Jacqueline R. Rettig and Albert Folch. Large-scale single-cell trapping and imaging using microwell arrays. *Analytical Chemistry*, 77(17):5628–5634, 2005. PMID: 16131075.

[53] Shohei Yamamura, Hiroyuki Kishi, Yoshiharu Tokimitsu, Sachiko Kondo, Ritsu Honda, Sathuluri Ramachandra Rao, Masahiro Omori, Eiichi Tamiya, and Atsushi Muraguchi. Single-cell microarray for analyzing cellular response. *Analytical Chemistry*, 77(24):8050–8056, 2005. PMID: 16351155.

[54] Jenny Fink, Manuel Thery, Ammar Azioune, Raphael Dupont, Francois Chatelain, Michel Bornens, and Matthieu Piel. Comparative study and improvement of current cell micro-patterning techniques. *Lab Chip*, 7:672–680, 2007.

[55] Hoyoung Yun, Kisoo Kim, and Won Gu Lee. Cell manipulation in microfluidics. *Biofabrication*, 5(2):022001, 2013.

[56] Xuan Mu, Wenfu Zheng, Jiashu Sun, Wei Zhang, and Xingyu Jiang. Microfluidics for manipulating cells. *Small*, 9(1):9–21, 2013.

[57] Alexander Revzin, Ronald G. Tompkins, and Mehmet Toner. Surface engineering with poly(ethylene glycol) photolithography to create high-density cell arrays on glass. *Langmuir*, 19(23):9855–9862, 2003.

[58] Dino Di Carlo, Nima Aghdam, and Luke P. Lee. Single-cell enzyme concentrations, kinetics, and inhibition analysis using high-density hydrodynamic cell isolation arrays. *Analytical Chemistry*, 78(14):4925–4930, 2006. PMID: 16841912.

[59] Siyang Zheng, Henry Lin, Jing-Quan Liu, Marija Balic, Ram Datar, Richard J. Cote, and Yu-Chong Tai. Membrane microfilter device for selective capture, electrolysis and genomic analysis of human circulating tumor cells. *Journal of Chromatography A*, 1162(2):154 – 161, 2007. 21st International Symposium on Microscale Bioseparations21st International Symposium on Microscale Bioseparations.

[60] Wei-Heong Tan and Shoji Takeuchi. A trap-and-release integrated microfluidic system for dynamic microarray applications. *Proceedings of the National Academy of Sciences*, 104(4):1146–1151, 2007.

[61] Alison M Skelley, Oktay Kirak, Heikyung Suh, Rudolf Jaenisch, and Joel Voldman. Microfluidic control of cell pairing and fusion. *Nature methods*, 6(2):147–152, 2009.

[62] Pei Yu Chiou, Aaron T Ohta, and Ming C Wu. Massively parallel manipulation of single cells and microparticles using optical images. *Nature*, 436(7049):370–372, 2005.

[63] Peter Tseng, Jack W Judy, and Dino Di Carlo. Magnetic nanoparticle-mediated massively parallel mechanical modulation of single-cell behavior. *Nature methods*, 9(11):1113–1119, 2012.

[64] Nikhil Mittal, Adam Rosenthal, and Joel Voldman. ndep microwells for single-cell patterning in physiological media. *Lab Chip*, 7:1146–1153, 2007.

[65] Xiaoyun Ding, Jinjie Shi, Sz-Chin Steven Lin, Shahrzad Yazdi, Brian Kiraly, and Tony Jun Huang. Tunable patterning of microparticles and cells using standing surface acoustic waves. *Lab Chip*, 12:2491–2497, 2012.

[66] Xiaoyun Ding, Sz-Chin Steven Lin, Brian Kiraly, Hongjun Yue, Sixing Li, I-Kao Chiang, Jinjie Shi, Stephen J. Benkovic, and Tony Jun Huang. On-chip manipulation of single microparticles, cells, and organisms using surface acoustic waves. *Proceedings of the National Academy of Sciences*, 109(28):11105–11109, 2012.

[67] Feng Guo, Zhangming Mao, Yuchao Chen, Zhiwei Xie, James P. Lata, Peng Li, Liqiang Ren, Jiayang Liu, Jian Yang, Ming Dao, Subra Suresh, and Tony Jun Huang. Three-dimensional manipulation of single cells using surface acoustic waves. *Proceedings of the National Academy of Sciences*, 113(6):1522–1527, 2016.

[68] Marie-Christine Daniel and Didier Astruc. Gold nanoparticles: Assembly, supramolecular chemistry, quantum-size-related properties, and applications toward biology, catalysis, and nanotechnology. *Chem. Rev.*, 104(1):293–346, January 2004.

[69] Bartlomiej Kowalczyk, István Lagzi, and Bartosz A. Grzybowski. Nanoseparations: Strategies for size and/or shape-selective purification of nanoparticles. *Current Opinion in Colloid and Interface Science*, 16(2):135 – 148, 2011.

[70] Y. Liu, M. Tourbin, S. Lachaize, and P. Guiraud. Silica nanoparticles separation from water: Aggregation by cetyltrimethylammonium bromide (ctab). *Chemosphere*, 92(6):681–687, 2013.

[71] Grazyna Bystrzejewska-Piotrowska, Jerzy Golimowski, and Pawel L. Urban. Nanoparticles: Their potential toxicity, waste and environmental management. *Waste Management*, 29(9):2587–2595, 2009.

[72] Seokheun Choi, Michael Goryll, Lai Yi Mandy Sin, Pak Kin Wong, and Junseok Chae. Microfluidic-based biosensors toward point-of-care detection of nucleic acids and proteins. *Microfluidics and Nanofluidics*, 10(2):231–247, 2011.

[73] David M. Whiley, Seweryn Bialasiewicz, Cheryl Bletchly, Cassandra E. Faux, Bruce Harrower, Allan R. Gould, Stephen B. Lambert, Graeme R. Nimmo, Michael D. Nissen, and Theo P. Sloots. Detection of novel influenza a(h1n1) virus by real-time rt-pcr. *Journal of Clinical Virology*, 45(3):203–204, 2009.

[74] Asfar S. Azmi, Bin Bao, and Fazlul H. Sarkar. Exosomes in cancer development, metastasis, and drug resistance: a comprehensive review. *Cancer and Metastasis Reviews*, 32(3):623–642, 2013.

[75] Patricia A. Gonzales, Trairak Pisitkun, Jason D. Hoffert, Dmitry Tchapyjnikov, Robert A. Star, Robert Kleta, Nam Sun Wang, and Mark A. Knepper. Large-scale proteomics and phosphoproteomics of urinary exosomes. *J. Am. Soc. Nephrol.*, 20(2):363, February 2009.

[76] Y Mori. Size-selective separation techniques for nanoparticles in liquid, kona powder part. *J*, 32:102–114, 2015.

[77] Adeel Safdar, Ayesha Saleem, and Mark A. Tarnopolsky. The potential of endurance exercise-derived exosomes to treat metabolic diseases. *Nature Reviews Endocrinology*, 12:504, May 2016.

[78] Pin Li, Melisa Kaslan, Sze Han Lee, Justin Yao, and Zhiqiang Gao. Progress in exosome isolation techniques. *Theranostics*, 7(3):789–804, January 2017.

[79] C. Wyatt Shields IV, Catherine D. Reyes, and Gabriel P. López. Microfluidic cell sorting: a review of the advances in the separation of cells from debulking to rare cell isolation. *Lab Chip*, 15:1230–1249, 2015.

[80] Thoriq Salafi, Kerwin Kwek Zeming, and Yong Zhang. Advancements in microfluidics for nanoparticle separation. *Lab Chip*, 17:11–33, 2017.

[81] Anna De Momi and Jamie. R. Lead. Behaviour of environmental aquatic nanocolloids when separated by split-flow thin-cell fractionation (splitt). *Science of The Total Environment*, 405(1):317–323, 2008.

[82] Mitsuhiro Ebara, John M. Hoffman, Allan S. Hoffman, Patrick S. Stayton, and James J. Lai. A photoinduced nanoparticle separation in microchannels via ph-sensitive surface traps. *Langmuir*, 29(18):5388–5393, May 2013.

[83] Y. Yang, Y. Z. Shi, L. K. Chin, J. B. Zhang, D. P. Tsai, and A. Q. Liu. Optofluidic nanoparticles sorting by hydrodynamic optical force. In *2013 Transducers & Eurosensors XXVII: The 17th International Conference on Solid-State Sensors, Actuators and Microsystems (TRANSDUCERS & EUROSENSORS XXVII)*, pages 2122–2125, 2013.

[84] Jianlong Wang, Ahsan Munir, Zanzan Zhu, and H. Susan Zhou. Magnetic nanoparticle enhanced surface plasmon resonance sensing and its application for the ultrasensitive

detection of magnetic nanoparticle-enriched small molecules. *Anal. Chem.*, 82(16):6782–6789, August 2010.

[85] Ahsan Munir, Zanzan Zhu, Jianlong Wang, and Hong Susan Zhou. Experimental investigation of magnetically actuated separation using tangential microfluidic channels and magnetic nanoparticles. *IET Nanobiotechnology*, 8:102–110(8), June 2014.

[86] Hyungkook Jeon, Youngkyu Kim, and Geunbae Lim. Continuous particle separation using pressure-driven flow-induced miniaturizing free-flow electrophoresis (pdf-induced μ-ffe). *Scientific Reports*, 6(1):19911, 2016.

[87] Swagatika Dash, Swati Mohanty, Sasmita Pradhan, and B. K. Mishra. Cfd design of a microfluidic device for continuous dielectrophoretic separation of charged gold nanoparticles. *Journal of the Taiwan Institute of Chemical Engineers*, 58:39–48, 2016.

[88] Sathyakumar S. Kuntaegowdanahalli, Ali Asgar S. Bhagat, Girish Kumar, and Ian Papautsky. Inertial microfluidics for continuous particle separation in spiral microchannels. *Lab Chip*, 9:2973–2980, 2009.

[89] Ryan T. Davies, Junho Kim, Su Chul Jang, Eun-Jeong Choi, Yong Song Gho, and Jaesung Park. Microfluidic filtration system to isolate extracellular vesicles from blood. *Lab Chip*, 12:5202–5210, 2012.

[90] J Knight. News feature: Honey, i shrunk the lab. *Nature*, 418:474–475, 2002.

[91] Peter Woias. Micropumps-past, progress and future prospects. *Sensors and Actuators B: Chemical*, 105(1):28–38, 2005.

[92] JC Rife, MI Bell, JS Horwitz, MN Kabler, RCY Auyeung, and WJ Kim. Miniature valveless ultrasonic pumps and mixers. *Sensors and Actuators A: Physical*, 86(1):135–140, 2000.

[93] Laura Bindila, Martin Froesch, Niels Lion, Željka Vukelić, Joël S. Rossier, Hubert H. Girault, Jasna Peter-Katalinić, and Alina D. Zamfir. A thin chip microsprayer system coupled to fourier transform ion cyclotron resonance mass spectrometry for glycopeptide screening. *Rapid Communications in Mass Spectrometry*, 18(23):2913–2920, 2004.

[94] Stefano Oberti, Adrian Neild, and Tuck Wah Ng. Microfluidic mixing under low frequency vibration. *Lab on a Chip*, 9(10):1435–1438, 2009.

[95] Jue Nee Tan and Adrian Neild. Microfluidic mixing in a y-junction open channel. *AIP Advances*, 2(3):032160, 2012.

[96] Priscilla Rogers and Adrian Neild. Selective particle trapping using an oscillating microbubble. *Lab on a chip*, 11(21):3710–3715, 2011.

[97] Andréas Manz, N Graber, and H áM Widmer. Miniaturized total chemical analysis systems: a novel concept for chemical sensing. *Sensors and actuators B: Chemical*, 1(1):244–248, 1990.

[98] Rosamund Daw and Joshua Finkelstein. Insight: Lab on a chip. *Nature*, 442(7101):367–418, 2006.

[99] Steve CC Shih, Hao Yang, Mais J Jebrail, Ryan Fobel, Nathan McIntosh, Osama Y Al-Dirbashi, Pranesh Chakraborty, and Aaron R Wheeler. Dried blood spot analysis by digital microfluidics coupled to nanoelectrospray ionization mass spectrometry. *Analytical chemistry*, 84(8):3731–3738, 2012.

[100] Mehdi Ghodbane, Elizabeth C Stucky, Tim J Maguire, Rene S Schloss, David I Shreiber, Jeffrey D Zahn, and Martin L Yarmush. Development and validation of a microfluidic immunoassay capable of multiplexing parallel samples in microliter volumes. *Lab on a Chip*, 15(15):3211–3221, 2015.

[101] Adam T Woolley and Richard A Mathies. Ultra-high-speed dna fragment separations using microfabricated capillary array electrophoresis chips. *Proceedings of the National Academy of Sciences*, 91(24):11348–11352, 1994.

[102] Dieter Schmalzing, Aram Adourian, Lance Koutny, Liuda Ziaugra, Paul Matsudaira, and Daniel Ehrlich. Dna sequencing on microfabricated electrophoretic devices. *Analytical chemistry*, 70(11):2303–2310, 1998.

[103] Amir M Ghaemmaghami, Matthew J Hancock, Helen Harrington, Hirokazu Kaji, and Ali Khademhosseini. Biomimetic tissues on a chip for drug discovery. *Drug discovery today*, 17(3):173–181, 2012.

[104] J Wiest, T Stadthagen, M Schmidhuber, M Brischwein, J Ressler, U Raeder, H Grothe, A Melzer, and B Wolf. Intelligent mobile lab for metabolics in environmental monitoring. *Analytical letters*, 39(8):1759–1771, 2006.

[105] Leanne Marle and Gillian M Greenway. Microfluidic devices for environmental monitoring. *TrAC Trends in Analytical Chemistry*, 24(9):795–802, 2005.

[106] Daniel Mark, Stefan Haeberle, Günter Roth, Felix Von Stetten, and Roland Zengerle. Microfluidic lab-on-a-chip platforms: requirements, characteristics and applications. In *Microfluidics based microsystems*, pages 305–376. Springer, 2010.

[107] Eric K Sackmann, Anna L Fulton, and David J Beebe. The present and future role of microfluidics in biomedical research. *Nature*, 507(7491):181–189, 2014.

[108] AS Utada, L-Y Chu, A Fernandez-Nieves, DR Link, C Holtze, and DA Weitz. Dripping, jetting, drops, and wetting: The magic of microfluidics. *Mrs Bulletin*, 32(9):702–708, 2007.

[109] Wei Wang, Rui Xie, Xiao-Jie Ju, Tao Luo, Li Liu, David A Weitz, and Liang-Yin Chu. Controllable microfluidic production of multicomponent multiple emulsions. *Lab on a chip*, 11(9):1587–1592, 2011.

[110] Javier Atencia and David J Beebe. Controlled microfluidic interfaces. *Nature*, 437(7059):648, 2004.

[111] Masumi Yamada, Megumi Nakashima, and Minoru Seki. Pinched flow fractionation: continuous size separation of particles utilizing a laminar flow profile in a pinched microchannel. *Analytical chemistry*, 76(18):5465–5471, 2004.

[112] Abhishek Jain and Jonathan D Posner. Particle dispersion and separation resolution of pinched flow fractionation. *Analytical chemistry*, 80(5):1641–1648, 2008.

[113] Tomoki Morijiri, Satoshi Sunahiro, Masashi Senaha, Masumi Yamada, and Minoru Seki. Sedimentation pinched-flow fractionation for size-and density-based particle sorting in microchannels. *Microfluidics and nanofluidics*, 11(1):105–110, 2011.

[114] Dongeun Huh, Joong Hwan Bahng, Yibo Ling, Hsien-Hung Wei, Oliver D Kripfgans, J Brian Fowlkes, James B Grotberg, and Shuichi Takayama. Gravity-driven microfluidic particle sorting device with hydrodynamic separation amplification. *Analytical chemistry*, 79(4):1369–1376, 2007.

[115] Masumi Yamada, Kyoko Kano, Yukiko Tsuda, Jun Kobayashi, Masayuki Yamato, Minoru Seki, and Teruo Okano. Microfluidic devices for size-dependent separation of liver cells. *Biomedical microdevices*, 9(5):637–645, 2007.

[116] John Oakey, Robert W Applegate Jr, Erik Arellano, Dino Di Carlo, Steven W Graves, and Mehmet Toner. Particle focusing in staged inertial microfluidic devices for flow cytometry. *Analytical Chemistry*, 82(9):3862–3867, 2010.

[117] Han Wei Hou, Ali Asgar S Bhagat, Alvin Guo Lin Chong, Pan Mao, Kevin Shyong Wei Tan, Jongyoon Han, and Chwee Teck Lim. Deformability based cell margination–a simple microfluidic design for malaria-infected erythrocyte separation. *Lab Chip*, 10(19):2605–2613, 2010.

[118] D Gobby, P Angeli, and Asterios Gavriilidis. Mixing characteristics of t-type microfluidic mixers. *Journal of Micromechanics and Microengineering*, 11(2):126, 2001.

[119] Yu-Cheng Lin, Yung-Chiang Chung, and Chung-Yi Wu. Mixing enhancement of the passive microfluidic mixer with j-shaped baffles in the tee channel. *Biomedical Microdevices*, 9(2):215–221, 2007.

[120] Yung-Chiang Chung, Yuh-Lih Hsu, Chun-Ping Jen, Ming-Chang Lu, and Yu-Cheng Lin. Design of passive mixers utilizing microfluidic self-circulation in the mixing chamber. *Lab Chip*, 4(1):70–77, 2004.

[121] Lotien Richard Huang, Edward C Cox, Robert H Austin, and James C Sturm. Continuous particle separation through deterministic lateral displacement. *Science*, 304(5673):987–990, 2004.

[122] Sungyoung Choi, Jeffrey M Karp, and Rohit Karnik. Cell sorting by deterministic cell rolling. *Lab on a Chip*, 12(8):1427–1430, 2012.

[123] Timm Krüger, David Holmes, and Peter V Coveney. Deformability-based red blood cell separation in deterministic lateral displacement devices–a simulation study. *Biomicrofluidics*, 8(5):054114, 2014.

[124] S Cerbelli. Separation of polydisperse particle mixtures by deterministic lateral displacement. the impact of particle diffusivity on separation efficiency. *Asia-Pacific Journal of Chemical Engineering*, 7:S356–S371, 2012.

[125] Jungwoo Lee, Kanglyeol Ha, and K Kirk Shung. A theoretical study of the feasibility of acoustical tweezers: Ray acoustics approach. *The Journal of the Acoustical Society of America*, 117(5):3273–3280, 2005.

[126] A. Ashkin. Acceleration and trapping of particles by radiation pressure. *Phys. Rev. Lett.*, 24:156–159, Jan 1970.

[127] Arthur Ashkin and JM Dziedzic. Optical levitation by radiation pressure. *Applied Physics Letters*, 19(8):283–285, 1971.

[128] Lukas Novotny, Randy X Bian, and X Sunney Xie. Theory of nanometric optical tweezers. *Physical Review Letters*, 79(4):645, 1997.

[129] Takayuki Nishizaka, Hidetake Miyata, Hiroshi Yoshikawa, Shin'ichi Ishiwata, and Kazuhiko Kinosita Jr. Unbinding force of a single motor molecule of muscle measured using optical tweezers. *Nature*, 377(6546):251, 1995.

[130] Youhua Tan, Dong Sun, Jinzhi Wang, and Wenhao Huang. Mechanical characterization of human red blood cells under different osmotic conditions by robotic manipulation with optical tweezers. *Biomedical Engineering, IEEE Transactions on*, 57(7):1816–1825, 2010.

[131] S Winoto-Morbach, V Tchikov, and W Mueller-Ruchholtz. Magnetophoresis: I. detection of magnetically labeled cells. *Journal of clinical laboratory analysis*, 8(6):400–406, 1994.

[132] Maciej Zborowski and Jeffrey J Chalmers. Magnetophoresis: fundamentals and applications. *Wiley Encyclopedia of Electrical and Electronics Engineering*, pages 1–23, 1999.

[133] Ahmed Munaz, Muhammad J. A. Shiddiky, and Nam-Trung Nguyen. Recent advances and current challenges in magnetophoresis based micro magnetofluidics. *Biomicrofluidics*, 12(3):031501, 2018.

[134] Ki-Ho Han, Arum Han, and A Bruno Frazier. Microsystems for isolation and electrophysiological analysis of breast cancer cells from blood. *Biosensors and bioelectronics*, 21(10):1907–1914, 2006.

[135] P Dunnill and MD Lilly. Purification of enzymes using magnetic bio-affinity materials. *Biotechnology and Bioengineering*, 16(7):987–990, 1974.

[136] K Mosbach and L Andersson. Magnetic ferrofluids for preparation of magnetic polymers and their application in affinity chromatography. *Nature*, 270(5634):259, 1977.

[137] Akihiko Kondo, Hiroko Kamura, and Ko Higashitani. Development and application of thermo-sensitive magnetic immunomicrospheres for antibody purification. *Applied Microbiology and Biotechnology*, 41(1):99–105, 1994.

[138] Xujing Wang, Xiao-Bo Wang, and Peter RC Gascoyne. General expressions for dielectrophoretic force and electrorotational torque derived using the maxwell stress tensor method. *Journal of electrostatics*, 39(4):277–295, 1997.

[139] Orlin D. Velev, Sumit Gangwal, and Dimiter N. Petsev. Particle-localized ac and dc manipulation and electrokinetics. *Annu. Rep. Prog. Chem., Sect. C: Phys. Chem.*, 105:213–246, 2009.

[140] Ronald Pethig. Dielectrophoresis: Status of the theory, technology, and applications. *Biomicrofluidics*, 4(2):022811, 2010.

[141] DS Clague and EK Wheeler. Dielectrophoretic manipulation of macromolecules: The electric field. *Physical Review E*, 64(2):026605, 2001.

[142] Günter Fuhr, Torsten Müller, Vera Baukloh, and Kurt Lucas. High-frequency electric field trapping of individual human spermatozoa. *Human Reproduction (Oxford, England)*, 13(1):136–141, 1998.

[143] Tjitske Heida, Wim LC Rutten, and Enrico Marani. Dielectrophoretic trapping of dissociated fetal cortical rat neurons. *IEEE Transactions on Biomedical Engineering*, 48(8):921–930, 2001.

[144] DW Pimbley, PD Patel, and CJ Robertson. Dielectrophoresis. In *Environmental Monitoring of Bacteria*, pages 35–53. Springer, 1999.

[145] M Mischel, F Rouge, I Lamprecht, C Aubert, and G Prota. Dielectrophoresis of malignant human melanocytes. *Archives of Dermatological Research*, 275(3):141–143, 1983.

[146] Swagatika Dash and Swati Mohanty. Dielectrophoretic separation of micron and submicron particles: A review. *ELECTROPHORESIS*, 35(18):2656–2672, 2014.

[147] Velimir M Ristic. *Principles of acoustic devices*. Krieger Publishing Company, 1983.

[148] Lord Rayleigh. On the circulation of air observed in kundt's tubes, and on some allied acoustical problems. *Philosophical Transactions of the Royal Society of London*, pages 1–21, 1884.

[149] Michael Faraday. Xvii. on a peculiar class of acoustical figures; and on certain forms assumed by groups of particles upon vibrating elastic surfaces. *Philosophical Transactions of the Royal Society of London*, 121:299–340, 1831.

[150] John Miles. On rayleigh's investigation of crispations of fluid resting on a vibrating support. *Journal of Fluid Mechanics*, 244:645–648, 1992.

[151] James Friend and Leslie Y Yeo. Microscale acoustofluidics: Microfluidics driven via acoustics and ultrasonics. *Reviews of Modern Physics*, 83(2):647, 2011.

[152] Caroline Holmes, Bruce W Drinkwater, and Paul D Wilcox. Post-processing of the full matrix of ultrasonic transmit–receive array data for non-destructive evaluation. *NDT & e International*, 38(8):701–711, 2005.

[153] A Bauer, G Becker, A Krone, T Fröhlich, and U Bogdahn. Transcranial duplex sonography using ultrasound contrast enhancers. *Clinical Radiology*, 51:19–23, 1996.

[154] Constantin Chilowsky and Paul Langevin. Procédés et appareils pour la production de signaux sous-marins dirigés et pour la localisation à distance d'obstacles sous-marins. *French Patent*, 502913, 1916.

[155] Peter R Hoskins, Kevin Martin, and Abigail Thrush. *Diagnostic ultrasound: physics and equipment*. Cambridge University Press, 2010.

[156] RM White and FW Voltmer. Direct piezoelectric coupling to surface elastic waves. *Applied Physics Letters*, 7(12):314–316, 1965.

[157] Lord Rayleigh. On waves propagated along the plane surface of an elastic solid. *Proceedings of the London Mathematical Society*, 1(1):4–11, 1885.

[158] WL Nyborg. Acoustic streaming. *Physical acoustics*, 2(Pt B):265, 1965.

[159] LP Gor'Kov. On the forces acting on a small particle in an acoustical field in an ideal fluid. In *Soviet Physics Doklady*, volume 6, page 773, 1962.

[160] Louis Vessot King. On the acoustic radiation pressure on spheres. *Proceedings of the Royal Society of London. Series A - Mathematical and Physical Sciences*, 147(861):212–240, November 1934.

[161] Alexander A Doinikov. Bjerknes forces and translational bubble dynamics. *Bubble and particle dynamics in acoustic fields: modern trends and applications*, pages 95–143, 2005.

[162] K Yosioka and Y Kawasima. Acoustic radiation pressure on a compressible sphere. *Acta Acustica united with Acustica*, 5(3):167–173, 1955.

[163] Takahi Hasegawa. Acoustic radiation force on a sphere in a quasistationary wave field—theory. *The Journal of the Acoustical Society of America*, 65(1):32–40, 1979.

[164] Mikkel Settnes and Henrik Bruus. Forces acting on a small particle in an acoustical field in a viscous fluid. *Phys. Rev. E*, 85:016327, Jan 2012.

[165] Alexander A Doinikov. Acoustic radiation pressure on a compressible sphere in a viscous fluid. *Journal of Fluid Mechanics*, 267:1–22, 1994.

[166] F.G. Mitri. Acoustic radiation force acting on elastic and viscoelastic spherical shells placed in a plane standing wave field. *Ultrasonics*, 43(8):681 – 691, 2005.

[167] Peter Barkholt Muller, Rune Barnkob, Mads Jakob Herring Jensen, and Henrik Bruus. A numerical study of microparticle acoustophoresis driven by acoustic radiation forces and streaming-induced drag forces. *Lab Chip*, 12:4617–4627, 2012.

[168] Henrik Bruus. *Theoretical microfluidics*, volume 18. Oxford university press Oxford, 2008.

[169] P. Glynne-Jones, P. P. Mishra, R. J. Boltryk, and M. Hill. Efficient finite element modeling of radiation forces on elastic particles of arbitrary size and geometry. *J Acoust Soc Am*, 133(4):1885–93, 2013.

[170] Takahi Hasegawa and Katuya Yosioka. Acoustic-radiation force on a solid elastic sphere. *The Journal of the Acoustical Society of America*, 46(5B):1139–1143, 1969.

[171] V. F. K. Bjerknes. *Fields of Force*. Columbia University Press, New York, 1906.

[172] A. A. Doinikov and S. T. Zavtrak. On the mutual interaction of two gas bubbles in a sound field. *Physics of Fluids*, 7(8):1923–1930, 1995.

[173] A.A Doinikov and S.T Zavtrak. Interaction force between a bubble and a solid particle in a sound field. *Ultrasonics*, 34(8):807 – 815, 1996.

[174] Glauber T. Silva and Henrik Bruus. Acoustic interaction forces between small particles in an ideal fluid. *Phys. Rev. E*, 90:063007, Dec 2014.

[175] Shahrokh Sepehrirahnama, Kian-Meng Lim, and Fook Siong Chau. Numerical study of interparticle radiation force acting on rigid spheres in a standing wave. *The Journal of the Acoustical Society of America*, 137(5):2614–2622, 2015.

[176] Lawrence A Crum. Bjerknes forces on bubbles in a stationary sound field. *The Journal of the Acoustical Society of America*, 57(6):1363–1370, 1975.

[177] MAH Weiser, RE Apfel, and EA Neppiras. Interparticle forces on red cells in a standing wave field. *Acta Acustica united with Acustica*, 56(2):114–119, 1984.

[178] Martin Gröschl. Ultrasonic separation of suspended particles-part i: Fundamentals. *Acta Acustica united with Acustica*, 84(3):432–447, 1998.

[179] Davood Saeidi, Mohsen Saghafian, Shaghayegh Haghjooy Javanmard, and Martin Wiklund. A quantitative study of the secondary acoustic radiation force on biological cells during acoustophoresis. *Micromachines*, 11(2), 2020.

[180] Thomas Laurell and Andreas Lenshof. *Microscale Acoustofluidics*. Royal Society of Chemistry, 2014.

[181] Jeffrey S Marshall and Junru Wu. Acoustic streaming, fluid mixing, and particle transport by a gaussian ultrasound beam in a cylindrical container. *Physics of Fluids*, 27(10):103601, 2015.

[182] Richard Shilton, Ming K Tan, Leslie Y Yeo, and James R Friend. Particle concentration and mixing in microdrops driven by focused surface acoustic waves. *Journal of Applied Physics*, 104(1):014910, 2008.

[183] Michael B Dentry, James R Friend, and Leslie Y Yeo. Continuous flow actuation between external reservoirs in small-scale devices driven by surface acoustic waves. *Lab Chip*, 14(4):750–758, 2014.

[184] Po-Hsun Huang, Nitesh Nama, Zhangming Mao, Peng Li, Joseph Rufo, Yuchao Chen, Yuliang Xie, Cheng-Hsin Wei, Lin Wang, and Tony Jun Huang. A reliable and programmable acoustofluidic pump powered by oscillating sharp-edge structures. *Lab Chip*, 14(22):4319–4323, 2014.

[185] Ghulam Destgeer, Hyunjun Cho, Byung Hang Ha, Jin Ho Jung, Jinsoo Park, and Hyung Jin Sung. Acoustofluidic particle manipulation inside a sessile droplet: four distinct regimes of particle concentration. *Lab Chip*, 16(4):660–667, 2016.

[186] Julien Reboud, Yannyk Bourquin, Rab Wilson, Gurman S Pall, Meesbah Jiwaji, Andrew R Pitt, Anne Graham, Andrew P Waters, and Jonathan M Cooper. Shaping acoustic fields as a toolset for microfluidic manipulations in diagnostic technologies. *Proceedings of the National Academy of Sciences*, 109(38):15162–15167, 2012.

[187] Chengxun Liu, Liesbet Lagae, and Gustaaf Borghs. Manipulation of magnetic particles on chip by magnetophoretic actuation and dielectrophoretic levitation. *Applied Physics Letters*, 90(18):184109, 2007.

[188] M. Antfolk, P. B. Muller, P. Augustsson, H. Bruus, and T. Laurell. Focusing of submicrometer particles and bacteria enabled by two-dimensional acoustophoresis. *Lab Chip*, 14(15):2791–2799, 2014.

[189] Jonas T. Karlsen, Wei Qiu, Per Augustsson, and Henrik Bruus. Acoustic streaming and its suppression in inhomogeneous fluids. *Phys. Rev. Lett.*, 120:054501, Jan 2018.

[190] Glauber T. Silva and Bruce W. Drinkwater. Acoustic radiation force exerted on a small spheroidal rigid particle by a beam of arbitrary wavefront: Examples of traveling and

standing plane waves. *The Journal of the Acoustical Society of America*, 144(5):EL453–EL459, November 2018.

[191] Adrian Neild, Stefano Oberti, and Jürg Dual. Design, modeling and characterization of microfluidic devices for ultrasonic manipulation. *Sensors and Actuators B: Chemical*, 121(2):452–461, 2007.

[192] Adrian Neild, Stefano Oberti, Gerald Radziwill, and Jürg Dual. Simultaneous positioning of cells into two-dimensional arrays using ultrasound. *Biotechnology and Bioengineering*, 97(5):1335–1339, 2007.

[193] Stefano Oberti, Adrian Neild, and Jürg Dual. Manipulation of micrometer sized particles within a micromachined fluidic device to form two-dimensional patterns using ultrasound. *The Journal of the Acoustical Society of America*, 121(2):778–785, 2007.

[194] Stefano Oberti, Adrian Neild, Raymond Quach, and Jürg Dual. The use of acoustic radiation forces to position particles within fluid droplets. *Ultrasonics*, 49(1):47–52, 2009.

[195] Thomas Laurell, Filip Petersson, and Andreas Nilsson. Chip integrated strategies for acoustic separation and manipulation of cells and particles. *Chemical Society Reviews*, 36(3):492–506, 2007.

[196] Filip Petersson, Lena Åberg, Ann-Margret Swärd-Nilsson, and Thomas Laurell. Free flow acoustophoresis: microfluidic-based mode of particle and cell separation. *Analytical chemistry*, 79(14):5117–5123, 2007.

[197] Jonathan D Adams and H Tom Soh. Tunable acoustophoretic band-pass particle sorter. *Applied physics letters*, 97(6):064103, 2010.

[198] Martin Wiklund and Hans M Hertz. Ultrasonic enhancement of bead-based bioaffinity assays. *Lab Chip*, 6(10):1279–1292, 2006.

[199] Andreas Nilsson, Filip Petersson, Henrik Jönsson, and Thomas Laurell. Acoustic control of suspended particles in micro fluidic chips. *Lab Chip*, 4(2):131–135, 2004.

[200] Bart Raeymaekers, Cristian Pantea, and Dipen N. Sinha. Manipulation of diamond nanoparticles using bulk acoustic waves. *Journal of Applied Physics*, 109(1):014317, 2011.

[201] Björn Hammarström, Thomas Laurell, and Johan Nilsson. Seed particle-enabled acoustic trapping of bacteria and nanoparticles in continuous flow systems. *Lab Chip*, 12(21):4296–4304, 2012.

[202] CS Hartmann. Systems impact of modern rayleigh wave technology. In *Rayleigh-Wave Theory and Application*, pages 238–253. Springer, 1985.

[203] Cheng-kai Luo, Prasad S Gudem, and James F Buckwalter. A 0.4–6-ghz 17-dbm b1db 36-dbm iip3 channel-selecting low-noise amplifier for saw-less 3g/4g fdd diversity receivers. *IEEE Transactions on Microwave Theory and Techniques*, 64(4):1110–1121, 2016.

[204] Colin Campbell. *Surface acoustic wave devices for mobile and wireless communications*. Academic press, 1998.

[205] Henry Wohltjen and Raymond Dessy. Surface acoustic wave probe for chemical analysis. i. introduction and instrument description. *Analytical Chemistry*, 51(9):1458–1464, 1979.

[206] Amnon Yariv and Pochi Yeh. Optical waves in crystal propagation and control of laser radiation. *John Wiley and Sons, Inc., New York, NY*, 1983.

[207] Donald B Armstrong, Jeffrey W Asher, Susan P Benitez, Richard A Jones, Joel C Kent, Michael L Lewis, and Robert C Phares. Surface acoustic wave touchscreen with housing seal, July 21 1998. US Patent 5,784,054.

[208] Leslie Y Yeo and James R Friend. Ultrafast microfluidics using surface acoustic waves. *Biomicrofluidics*, 3(1):012002, 2009.

[209] Jason C Brenker, David J Collins, Hoang Van Phan, Tuncay Alan, and Adrian Neild. On-chip droplet production regimes using surface acoustic waves. *Lab Chip*, 16(9):1675–1683, 2016.

[210] Muhsincan Sesen, Tuncay Alan, and Adrian Neild. Microfluidic on-demand droplet merging using surface acoustic waves. *Lab Chip*, 2014.

[211] Lothar Schmid and Thomas Franke. Acoustic modulation of droplet size in a t-junction. *Applied Physics Letters*, 104(13):133501, 2014.

[212] Muhsincan Sesen, Tuncay Alan, and Adrian Neild. Microfluidic plug steering using surface acoustic waves. *Lab on a Chip*, 15(14):3030–3038, 2015.

[213] Scott R Heron, Rab Wilson, Scott A Shaffer, David R Goodlett, and Jonathan M Cooper. Surface acoustic wave nebulization of peptides as a microfluidic interface for mass spectrometry. *Analytical Chemistry*, 82(10):3985–3989, 2010.

[214] Aisha Qi, Leslie Y Yeo, and James R Friend. Interfacial destabilization and atomization driven by surface acoustic waves. *Physics of Fluids*, 20(7):074103, 2008.

[215] David J Collins, Tuncay Alan, and Adrian Neild. Particle separation using virtual deterministic lateral displacement (vdld). *Lab on a Chip*, 14(9):1595–1603, 2014.

[216] Jason Zhou, Ruhollah Habibi, Farzan Akbaridoust, Adrian Neild, and Reza Nosrati. Paper-based acoustofluidics for separating particles and cells. *Anal. Chem.*, May 2020.

[217] Kentaro Nakamura. *Ultrasonic transducers: Materials and design for sensors, actuators and medical applications*. Elsevier, 2012.

[218] Thomas L Szabo and AJ Slobodnik. The effect of diffraction on the design of acoustic surface wave devices. *IEEE Transactions on Sonics and Ultrasonics*, 20(3):240–251, 1973.

[219] RT Smith and FS Welsh. Temperature dependence of the elastic, piezoelectric, and dielectric constants of lithium tantalate and lithium niobate. *Journal of applied physics*, 42(6):2219–2230, 1971.

[220] James F Tressler, Sedat Alkoy, and Robert E Newnham. Piezoelectric sensors and sensor materials. *Journal of Electroceramics*, 2(4):257–272, 1998.

[221] Don A Berlincourt, Daniel R Curran, and Hans Jaffe. Piezoelectric and piezomagnetic materials and their function in transducers. *Physical Acoustics: Principles and Methods*, 1(Part A):247, 1964.

[222] RM Arzt, E Salzmann, and K Dransfeld. Elastic surface waves in quartz at 316 mhz. *Applied Physics Letters*, 10(5):165–167, 1967.

[223] Michael B Dentry, Leslie Y Yeo, and James R Friend. Frequency effects on the scale and behavior of acoustic streaming. *Physical Review E*, 89(1):013203, 2014.

[224] Andreas Winkler, Paul Bergelt, Lars Hillemann, and Siegfried Menzel. Influence of viscosity in fluid atomization with surface acoustic waves. *Open Journal of Acoustics*, 6(03):23, 2016.

[225] Jinjie Shi, Xiaole Mao, Daniel Ahmed, Ashley Colletti, and Tony Jun Huang. Focusing microparticles in a microfluidic channel with standing surface acoustic waves (ssaw). *Lab on a Chip*, 8(2):221–223, 2008.

[226] Tsung-Tsong Wu, He-Tai Tang, Yung-Yu Chen, and Pei-Ling Liu. Analysis and design of focused interdigital transducers. *Ultrasonics, Ferroelectrics, and Frequency Control, IEEE Transactions on*, 52(8):1384–1392, 2005.

[227] Hiromi Yatsuda. Design techniques for saw filters using slanted finger interdigital transducers. *Ultrasonics, Ferroelectrics, and Frequency Control, IEEE Transactions on*, 44(2):453–459, 1997.